NUMERICAL STUDY OF FLOW AND HEAT TRANSFER IN ROTATING MICROCHANNELS

A Dissertation

by

PRATANU ROY

Submitted to the Office of Graduate and Professional Studies of
Texas A&M University
in partial fulfillment of the requirements for the degree of

DOCTOR OF PHILOSOPHY

Chair of Committee,	N. K. Anand
Co-Chair of Committee,	Debjyoti Banerjee
Committee Members,	Je-Chin Han
	Hamn-Ching Chen
Head of Department,	Andreas A. Polycarpou

December 2014

Major Subject: Mechanical Engineering

ABSTRACT

Investigation of fluid flow and heat transfer in rotating microchannels is important for centrifugal microfluidics, which has emerged as an advanced technique in biomedical applications and chemical separations. The centrifugal force and the Coriolis force, arising as a consequence of the microchannel rotation, change the flow pattern significantly from the symmetric profile of a non-rotating channel. A successful design of a centrifugal microfluidic device depends on effectively regulating these forces in rotating microchannels. Although a large number of experimental studies have been performed in order to demonstrate the applications of centrifugal microfluidics in various fields, a systematic study on the effect of rotation, channel aspect ratio, and wall boundary conditions on the fluid flow and heat transfer phenomena in rotating microchannels has not yet been conducted.

During the present study, pressure-based finite volume solvers in both staggered and collocated grids were developed to solve steady and unsteady, incompressible Navier-Stokes equations. The serial solver in collocated grid was parallelized using a Message Passing Interface (MPI) library. In order to accelerate the convergence of the collocated finite volume solver, a non-linear multi-grid method was developed. The parallel performances of the single and multi-grid solvers were tested on a two-dimensional lid driven cavity flow. High fidelity benchmark solution to a lid driven cavity flow problem in a 1024×1024 grid was presented for a range of Reynolds numbers. Parallel multigrid speedup as high as three orders of magnitude was achieved for low Reynolds number flows. In addition, the optimal multigrid efficiency was validated.

The fluid flow in a rotating microchannel was modeled as a steady, laminar incompressible flow with no slip and slip boundary conditions. For no slip boundary condition, critical values of parameters that determine the extent of the centrifugal force and the Coriolis force were identified. The critical aspect ratio (=width/height) that causes the optimal mixing of two liquids was found to be 1.0. For liquid slip boundary condition, the effect of rotation on liquid slip flow in rotating microchannels with hydrophobic and superhydrophobic surfaces was studied. New correlations for friction relation (fRe) as a function of slip length (λ) and rotational Reynolds number (Re_ω) were proposed. It was also found that, the liquid slip can increase or decrease the heat transfer depending on the secondary flow effect and the aspect ratio of the microchannel.

The microscale effects, such as surface tension and contact angle boundary condition, were included in the modeled problem. A level set method was applied to incorporate these microscale effects, which will enable us to investigate the unsteady nature of the liquid meniscus during two-phase flow simulations.

DEDICATION

To My Late Father Dr. Prodosh Kumar Roy

and

My Mother Ms. Anjana Roy

ACKNOWLEDGEMENTS

I am greatly indebted to my advisor Dr. N. K. Anand, who supervised my doctoral work with utmost care and great patience. As a mentor, he gave me complete freedom of thinking, inspired me to reason critically, respected my opinions, and continuously motivated me to conduct original research - all of which are crucial for nurturing creativity and fostering independent learning. The research reported in this dissertation was partly supported by James and Ada Forsyth Professorship Endowment Funds, for which I am again thankful to Dr. Anand.

I am grateful to my co-advisor Dr. Debjyoti Banerjee for introducing me to the world of multiphase flow and heat transfer, and particularly to the subject of centrifugal microfluidics. He funded me during the initial stage of my PhD and gave me the opportunity to conduct experimental work, which certainly enhanced my experience in experimental methods in fluid flow and heat transfer.

I am thankful to Dr. J. C. Han and Dr. H. C. Chen for taking the time to serve as the committee members. Their courses have been very useful to improve my understanding on the underlying physics of convective heat transfer and computational techniques of fluid mechanics.

I am also thankful to Dr. Diego Donzis for his guidance in using high performance computing (HPC) resources in the finite volume solver. He not only taught me the different techniques of parallelization, but also motivated me to study the state of the art of HPC and apply them to a non-linear multigrid technique. The collaboration with him that started with a simple course project resulted in a journal publication and formed an important part of the dissertation. I would also like to thank Dr. Sharath Girimaji for his insightful lectures on turbulent flow phenomena and turbulence modeling. The joint effort with his group also produced a conference paper on hybrid RANS-LES modeling. Although the work was not included in my dissertation, it added diversity to my research experience.

My friends and colleagues have played a vital role in this endeavor. My heartfelt thanks to Md. Yakut Ali, Bhanesh Akula, Shriram Jagannathan, Aditya Konduri and Pooyan Razi for their continuous support. The countless hours I have spent with them having critical discussions on various scientific topics were invaluable. I would also like to thank my colleagues Robert Park, Kyle Mcvay, Han Li and Ted Blowe. Teaching different topics of finite volume method to them has enhanced my knowledge on the subject matter.

The staff of the Texas A&M University Supercomputing facility are also gratefully acknowledged. They have patiently responded to my queries numerous times, and assisted me in different stages of the code development, including optimization and parallelization. In particular, Mr. Spiros Vellas, Mr. Marinus Pennings and Ms. Ping Luo were very helpful and I am really thankful to them.

I am ever thankful to my mother, who always encouraged me to pursue graduate studies and who sacrificed everything for the betterment of my future. I am also grateful to my sister Antara Roy and my in-laws for supporting me throughout my graduate studies.

I would like to express my deepest gratitude to my wife, Koly Sengupta, whose love, support and inspiration have been the key ingredients in the successful completion of my doctoral work. She has been a true companion in every aspect of my graduate student life and the compromises she made to share the stressful hours of this long journey are unprecedented.

Finally, a special thanks to Ms. Teresa Wright for her painstaking effort to proofread my dissertation manuscript. She made sure that all is well for me in the end.

NOMENCLATURE

Roman Symbols

a	Finite volume discretization coefficients
a	Microchannel width, (m)
a^+	Normalized channel width, $\frac{a}{2D_h}$
b	Microchannel height, (m)
b	Source term in the discretized equations
b^+	Normalized channel height, $\frac{b}{2D_h}$
C	Slope of the curve in Equation 6.17
C_p	Specific heat of the fluid $(Jkg^{-1}K^{-1})$
D	Diffusion strength
D_h	Hydraulic diameter (m)
d_r	Distance of microchannel inlet from the disk center (m)
F	Flow strength
f	Friction factor
f_ω	Centrifugal force (N)
f_c	Coriolis force (N)
f_e	Geometric interpolation factor for east face

fRe	Poiseuille number or friction relation
G	Modified axial pressure gradient
G^*	Reduced axial pressure gradient
g	Gravitational acceleration (ms^{-2})
H	$\sum\limits_{CVs} a_{nb}\phi_{nb}$
H	Water column height in dam breaking simulation
$H(\psi)$	Heaviside function
h	Height of the water level in water column breaking simulation
i, j	Index variables associated with the grid points
I_{2h}^{h}	Prolongation operator
I_{h}^{2h}	Restriction operator
k	Thermal conductivity of the fluid ($Wm^{-1}K^{-1}$)
Kn	Knudsen number
L	Length of the microchannel, (m)
$\mathcal{L}$	Perimeter enclosed by the interface
l_k	Kapitza length (m)
N	Size of the problem
np	Number of processors
Nu	Nusselt number

Nx, Ny	Number of control volumes in x and y direction
P	Peclet number
p	Pressure (Pa)
p'	Pressure correction variable
p^*	Modified pressure (Pa)
p_1, p_2, p_3, p_4	Polynomial coefficients for the correlation of C
Pr	Prandtl number
R	Residual
$\mathcal{R}$	Set of real numbers
R^2	Regression coefficient
Re	Flow Reynolds number
Re_ω	Rotational Reynolds number
Ro	Rossby number (Re_ω/Re)
S	Source term
s_1, s_2, s_3	Smoothness estimators for WENO-5 scheme
T	Temperature (^oC)
t	Time (sec)
$\mathcal{T}$	Time period (sec)
u, v, w	Velocity in x, y, z-directions (ms^{-1})

$\mathbf{V}$	Velocity vector (ms^{-1})
$\mathcal{V}$	Volume of fluid element
$\mathcal{V}'$	Volume error
W	Non dimensional velocity, $w/(D_h^2/\mu\frac{\partial p^*}{\partial z})$
w_{slip}	Slip velocity (ms^{-1})
X	Non dimensional x, x/D_h
x^+	Normalized x-coordinate, x/a
x_i	Distance in x, y, z-directions for i=1,2,3 respectively (m)
Y	Non dimensional y, y/D_h
y^+	Normalized y-coordinate, y/b
z^+	Normalized z-coordinate, z/L

Acronyms

CDS	Central Difference Scheme
CV	Control Volume
FAS	Full Approximation Scheme
FMG	Full Multigrid
MG	Multigrid
PLS	Power Law Scheme
RMS	Root Mean Square

RPM	Revolution Per Minute
SG	Single Grid

Greek Symbols

α	Aspect ratio, a/b
$\alpha_u, \alpha_v, \alpha_p$	Under-relaxation factor for u, v and p variables respectively
β	Ratio of the Coriolis force to the centrifugal force
$\Delta x, \Delta y$	Control volume length in x and y directions
$\delta x, \delta y$	Diffusion length in x and y directions
$\delta(\psi)$	Dirac delta function
Γ	Diffusion coefficient
γ	Finite difference stencils
$\Gamma(t), \delta\Omega$	Interface between the two fluid regions
κ	Curvature of the interface (m^{-1})
μ	Dynamic viscosity of the fluid (Pa-s)
Ω	Convergence factor
ω	Rotational frequency ($rad.s^{-1}$)
Ω^+, Ω^-	Two fluid regions separated by the interface
ϕ	Generic flux variable
$\psi(\mathbf{x}, t)$	Level set function

ρ	Density of the fluid (kgm^{-3})
σ	Surface tension (Nm^{-1})
θ_c	Contact angle (^{o})
ε	Bandwidth of numerical smearing
φ_k	Eigenvalues defined in Equation 6.9
ϖ	Weights of WENO-5 scheme
ξ_m, ξ_n	Eigenvalues defined in Equation 5.10
$\mathbf{n}$	Normal vector to the interface
λ	Slip length, or slip coefficient (m)

Subscripts

app	Apparent
avg	Average
cr	Critical
eff	Effective
$exit$	Exit/outlet of the microchannel
f	Fluid
g	Gas
$h, 2h$	Fine and coarse grid respectively
i, j	Index variables for the tensor notations

in	Inlet of the microchannel
l	Liquid
nb	Neighbor node
P, W, E, S, N	Center, west, east, south, and north nodal points, respectively
pc	Pressure correction
w, e, s, n	West, east, south, and north faces, respectively
$wall$	Wall surface

Superscripts

$'$	Correction to the fine grid variable
$''$	Correction to the coarse grid variable
$*$	Approximate solution
$\widehat{\ }$	Coarse grid variable
$\widetilde{\ }$	Restricted quantities in coarse grid
$h, 2h$	Fine and coarse grid respectively
l	Value from previous iteration
n	Index variable associated with the time step

TABLE OF CONTENTS

LIST OF FIGURES

LIST OF TABLES

1. INTRODUCTION

1.1 Centrifugal Microfluidics: An Overview

Centrifugally actuated miniaturized microfluidic devices have revolutionized the area of chemical analysis and biomedical diagnostic applications in the recent years [1–4]. In these devices, an array of microchannels is etched on a circular substrate which is then rotated at a certain frequency. This kind of arrangement is popularly known as a *Lab–on–a–CD* or *LabCD* [3,5,6]. The objective of this compact disk-like platform is to combine various liquid handling steps in order to integrate all the bio-chemical processes in a flexible way [7]. By controlling the rotating frequency of this platform, different functions such as mixing, separation, routing, capillary valving, siphoning, volume splitting and droplet generation [2,4,7] can be performed on various samples.

A successful design of centrifugal microfluidic devices requires a clear understanding of fluid flow inside rotating microchannels. The nature of fluid flow inside rotating microchannels is primarily governed by the pseudo forces, namely the centrifugal and the Coriolis forces, arising as a consequence of expressing the governing equations in rotating reference frame. At low rotation speed, the flow is purely driven by the centrifugal force. At higher rotation, the Coriolis force becomes dominant and a significant secondary flow is introduced perpendicular to the primary flow direction. The effective operation of a centrifugal microfluidic platform depends on regulating these forces in a controlled manner. For example, the working principle of a capillary burst valve depends on the balance between the centrifugal force and the surface tension force [8]. On the other hand, mixing is enhanced in microchannels when Coriolis force dominates over centrifugal force [9]. The process becomes more complicated when heat transfer is included in the scenario. In some cases it is necessary to maintain the fluid within specific temperature zones while rotating it inside microchannel. For instance, polymerase chain reaction (PCR) requires repeated thermocycling of the analyte nucleic acid in a microchamber [6]. With the secondary flow effect, thermal homogeneity can be achieved for PCR amplification on a spinning disk. Therefore, in order to compute the correct temperature distribution of the fluid inside a rotating microchannel, the effect of rotation on convective heat transfer should be taken into consideration.

1.1.1 Recent Progresses: A Brief Literature Review

A number of researchers performed experimental and numerical investigations of centrifugal microfluidics using the continuum assumption approach. Duffy et al. [10] compared the experimental flow rate and Hagen–Poiseuille flow rate of microfluidics channels of different widths (20 µm − 500 µm), depths (16 µm − 340 µm), and lengths (12.5 mm − 182 mm) subjected to different rates of rotation (400 RPM − 1,600 RPM). Comparing the experimental and theoretical flow rates in a log-log graph, they showed that centrifugally driven microchannel flows can be treated as Hagen–Poiseuille flows for a wide range of attributes. Siegrist et al. [6] numerically and experimentally analyzed the rotating polymerase chain reaction (PCR) microchamber filling behavior at different inlet pressure boundary conditions (0.5 kPa − 2 kPa). Their study has shown that, due to the induced centrifugal and Coriolis forces, the mechanism of chamber filling is different for the rotating case from that for the stationary case. Ducree et al. [11] investigated the patterning of flow and mixing in radially rotating microchannels and identified that the key impact parameters governing the Coriolis force-induced reshaping of the contact surface between two fluids are the channel length, aspect ratio and the rate of rotation. They also invented a multilamination technique on a planar split-and-recombine structure to accelerate mixing of liquids in rotating microchannels [12]. All of the numerical studies used commercial CFD software to conduct the simulations. A state-of-the-art literature review on the applications of rotating microchannels can be found in [13].

1.1.2 What is Missing?

Two non-dimensional numbers, namely flow Reynolds number (Re) and rotational Reynolds number (Re_ω) characterize the physics of rotating channel flows. Reynolds number $\left(Re = \frac{\rho W_{\mathrm{avg}} D_{\mathrm{h}}}{\mu}\right)$ is the ratio of the inertial force to the viscous force and rotational Reynolds number $\left(Re_\omega = \frac{\rho \omega D_{\mathrm{h}}^2}{\mu}\right)$ is the ratio of the rotating inertial force to the viscous force. If a parabolic axial velocity profile is assumed in the primary flow direction, then it can be shown that [12] the axial velocity (w) is in the order of $\left(\sim \frac{\rho \omega D_{\mathrm{h}}^2 d_{\mathrm{r}}}{8\mu}\right)$. Thus, the ratio of the Coriolis force ($2\omega w$) and the centrifugal force ($\omega^2 d_r$) becomes $\beta = \frac{\rho \omega D_{\mathrm{h}}^2}{8\mu}$, which is nothing but a multiple of rotational Reynolds number (Re_ω). This means that, a high rotational Reynolds number will induce a high Coriolis force resulting in a strong secondary flow. In a recent article on the mixing behavior in rotationally actuated microfluidics devices, Chakraborty et al. [9] identified three distinct mixing regimes based on the change of mixing patterns with the change of β. The three regimes are: (1) diffusion-based mixing (at low rotation speeds, $0 \leq \beta \leq 1.0$); (2) Coriolis force-based mixing (at intermediate rotation speeds, $1.0 \leq \beta \leq 2.0$); and (3) mixing based on flow instability (at high rotation speeds, $\beta \geq 2.0$). It is interesting to note that, although the Coriolis force-based mixing regime starts at $\beta = 1.0$ the efficient mixing occurs when β exceeds 1.35 which corresponds to $Re_\omega \geq 10.8$. Using numerical simulation of flow through rotating straight pipes, Lei and Hsu [14] showed that, when $Re_\omega \leq 10$ and $Re_\omega G \leq 100$, the axial velocity profile is not significantly affected by the rotational forces and thus remains parabolic and axisymmetric. Here, $G = \frac{G^* D_{\mathrm{h}}^3}{\rho v^2}$ where G^* is the reduced axial pressure gradient, which includes the effect of centrifugal force. The striking similarity of these two reported values of Re_ω indicates that there must be a cut-off value of Re_ω over which the effect of rotation becomes dominant and the Coriolis force-based secondary flow becomes dominant over the centrifugally driven axial flow. One of the aims of this work is to establish a criteria for this critical rotational Reynolds number ($Re_{\omega,cr}$, in order to differentiate between the diffusion dominated region and secondary flow dominated region.

1.2 Liquid Slip in Rotating Microchannels

It is well established that flow in macroscale is governed by the Navier-Stokes equations with no slip boundary conditions at the solid-fluid interfaces [15]. However, in microscale, the assumption of the no-slip boundary condition may not be valid [16]. The recent progress in the applications of microfluidic devices has resulted in an increased interest on the possibility of the slip boundary condition. The size of these devices is so small that regulating fluid by pressure driven mechanisms becomes very difficult. This is because, for a fixed flow rate, the pressure gradient along the microchannel increases exponentially as the characteristic length of the microchannel is decreased [17]. Exploring the slip boundary condition can be a possible alternative to reduce the large amount of hydrodynamic resistance encountered in microfluidic applications.

1.2.1 Liquid Slip: A Continuum Phenomena

The phenomenon of slip can occur for both gases and liquids. However, there is a fundamental difference between the slip in gas microflows and the slip in liquid flows. Slip flow in gas results from a possible breakdown of the continuum hypothesis i.e. when the characteristic length of the microchannel is on the order of the dimension of gas molecules, the flow can no longer be considered as a continuum medium and the gas molecules can exhibit slip at the solid boundary [15]. On the other hand, slippage in liquid is encountered as a consequence of the interaction between a coated or structured solid wall and the adjacent liquid particle. Thus, liquid slip can occur even when the continuum hypothesis is perfectly valid.

Knudsen number (Kn), which is the ratio of the mean free path of the fluid molecules and the characteristic length, is often used as a validity indicator of the continuum hypothesis assumption [18–20]. For $Kn < 0.01$, the fluid can be considered as a continuum. As the Knudsen number approaches unity, the continuum equations begin to fail, but for $Kn < 0.1$ the no slip boundary condition can still be adjusted using a slip parameter [21]. The region $(0.01 < Kn < 0.1)$ is called the slip regime, to distinguish it from the transition regime $(0.1 < Kn < 10)$, in which the Boltzmann equations are solved directly.

For liquid, such as water, Knudsen number Kn falls well within the continuum region, where Navier Stokes equations with no slip boundary conditions are applicable for any practical range of microchannel size. However, even for water flow in microchannels, contradictory results on the validity of the no slip boundary conditions have been reported in the literature. Garimella and Sobhan [22] conducted a comparative study on transport in microchannels and concluded that analyses based on Navier-Stokes and energy equations can adequately predict the flow and heat transfer characteristics in microchannels having a hydraulic diameter greater than 50 µm, provided that the experimental conditions and measurements are correctly identified and simulated. Another critical review on single phase liquid friction factors in microchannels was performed by Steinke and Kandlikar [23]. By analyzing over 150 papers that directly deal with the pressure drop measurements in microchannels, they generated a database of over 5,000 data points with the Reynolds number ranging from 0.002 to 5,000 and hydraulic diameter ranging from 8 µm to 990 µm. They argued that the studies which reported a deviation of friction factor from conventional theory did not account for the entrance or exit effect or the developing region in the microchannel. Therefore, it was concluded that the classical correlations are reliable in predicting the flow and heat transfer phenomena in microchannels as long as the entrance or exit effect and the experimental uncertainties are taken into account.

1.2.2 Experimental Evidence of Liquid Slip in Microchannels

In the studies mentioned above, the microchannel wall was made of one of the following materials: silicon, stainless steel, copper, aluminum, fiber glass, and glass - all of which are hydrophilic in nature. A hydrophilic surface has a strong affinity to water with a typical contact angle of less than 90 degrees [24]. In case of a hydrophilic surface, experimental studies have confirmed the validity of the no-slip boundary condition down to the resolution of a few nanometers [25], although evidence of slip in hydrophilic surfaces has also been published [26]. On the contrary, a large number of experimental studies have reported some form of liquid slip at the solid surface coated with hydrophobic materials. Due to the repellent nature of the hydrophobic surface, the fluid molecules adjacent to the surface (located at a distance in the order of the mean free path of fluid molecules) do not stick to the solid boundary resulting in an overall velocity slip. This slip velocity w_{slip} is related to the normal velocity gradient of the fluid adjacent to the wall with a slip length λ. Figure 1.1 shows the diagram of a microchannel with hydrophobic walls and the equivalent channel with slip flow parameters. Tretheway et al. [27] experimentally showed an apparent fluid slip in 30 µm × 300 µm microchannels with hydrophobic walls using micron-resolution particle image velocimetry. The slip velocity at the wall was approximately 10% of the free stream velocity which produced a slip length of about 1 µm. Pit et al. [28] provided experimental evidence of liquid slip at the wall for hexadecane flowing between two rotating parallel disks kept at a distance of 190 µm. They measured a slip length of 400 nm when the sapphire (solid) surface was coated with octadecyltrichlorosilane (OTS). Watanabe et al. [29] experimentally demonstrated slip phenomena of Newtonian fluid over a highly water-repellent wall of a rectangular duct with a relatively large cross-sectional area (15 mm × 15 mm). Comprehensive reviews of the recent investigations on the evidence of liquid slip at solid-liquid interfaces of microfluidic systems can be found in [15, 30].

Another way to engineer large slip is to use superhydrophobic surfaces, which can dramatically reduce the hydrodynamic resistance [31]. The superhydrophobic surfaces consist of micro-pillars or micro-grooves, coated with a thin hydrophobic layer, creating very small cavities between these pillars/grooves [32]. The liquid cannot penetrate these cavities because of its surface tension effect, which induces an artificial slip over the structured surface. The amount of slip in the solid-fluid interface and in the air-fluid interface is different. Hence, an effective slip length λ_{eff} is necessary to calculate the slip velocity w_{slip}. Figure 1.2 shows a schematic of a superhydrophobic microchannel surface and an equivalent microchannel with an effective slip length λ_{eff}. Using these specially engineered surfaces, a drag reduction of 12-14% has been reported by Watanabe et al. [33, 34] and a slip length as high as 185 µm has been reported by Choi and Kim [35]. A review of slip phenomena over superhydrophobic surfaces can be found in [31].

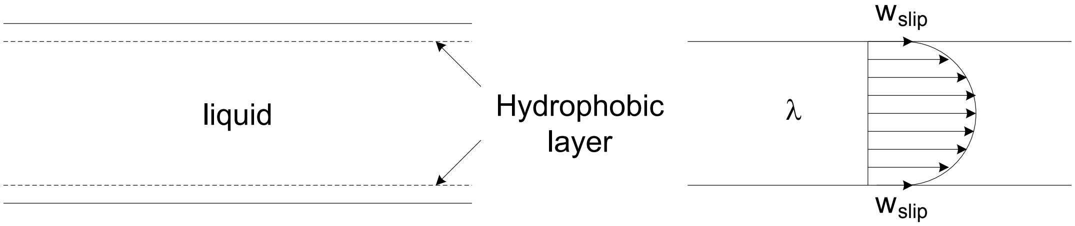

Figure 1.1: Hydrophobic layer in a microchannel (left) and equivalent microchannel with a slip velocity w_{slip} and a slip length λ (right)

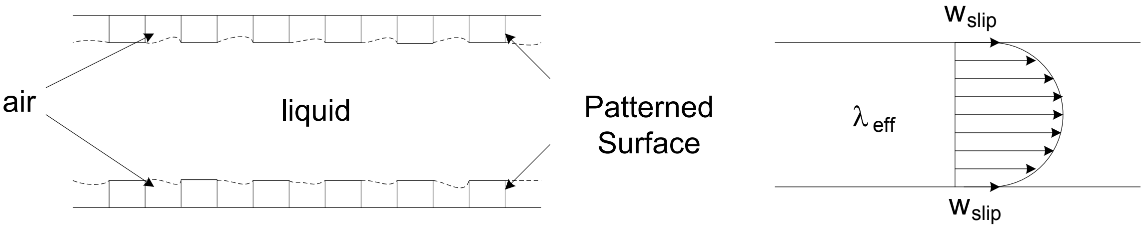

Figure 1.2: Superhydrophobic surface in a microchannel (left) and equivalent microchannel with a slip velocity w_{slip} and a slip length λ_{eff} (right)

1.2.3 Slippage in Rotating Microchannels: A New Concept

In case of centrifugal microfluidics, the primary focus has been on the regulation of fluid (mixing, separation, and the like) under the influence of rotation assuming no slip boundary condition. In spite of a large number of published experimental and a few numerical studies, the investigation of liquid slip in rotating microchannels has only been recently reported by Roy et al. [36]. Thus, one of the objectives of this work is to thoroughly investigate the liquid slip flow phenomena inside a microchannel subjected to a uniform rotation.

1.3 Numerical Simulation: A Parallel Finite Volume Multigrid Solver

In order to investigate the flow physics in the rotating microchannel, numerical solutions of the Navier-Stokes equations are necessary. In this work, we aim to develop both serial and parallel codes to solve two-dimensional, and three-dimensional, steady, and unsteady, incompressible Navier-Stokes equations. A finite volume method will be applied to discretize the governing equations. A non-linear multigrid technique will be applied to accelerate the convergence of the solver. The solution to one-dimensional convection-diffusion equation will be represented by power-law scheme (PLS) or central difference scheme (CDS). Velocity and pressure variables were linked by SIMPLE algorithm, details of which can be found in Patankar [37]. A line by line method, which is a combination of tri-diagonal matrix algorithm (TDMA) and Gauss-Seidel method, will be used to solve the discretized equations.

1.3.1 Evolution of Interface: A Level Set Method

A level set method is an interface capturing method first introduced by Osher and Sethian [38]. In this method, a level set function $\psi(x,t)$ is introduced, which implicitly carries the information of the interface and an evolution equation for $\psi(x,t)$, which is an initial-value advection equation, is solved to track the propagating surface. The evolving interface is embedded as a zero-level set of the level set function i.e. $\psi(x,t) = 0$. In this way, the merging and separation of fluid surfaces can be naturally handled without any special treatment. A smoothed Heaviside function is used to calculate the fluid properties inside and outside the interface. In our work, we propose to apply a level set method in the above mentioned finite volume code to track the fluid meniscus in a microchannel under the influence of different body forces. The application of the level set method will enable us to implement the capillary effect, which is of crucial importance in liquid microflows.

1.4 Objectives of the Study

The primary objectives of the present work are following :

1. To develop serial and parallel finite volume solvers in order to solve two-dimensional, and three-dimensional, steady, and unsteady, incompressible Navier-Stokes equations and energy equations with constant, and variable thermo-physical properties.
2. To apply a non-linear multigrid technique for accelerating the convergence of the finite volume solver and assess the affects of parallelization on the multigrid elements.
3. To study the effect of rotational speed, hydraulic diameter, and aspect ratio on the liquid flow inside rotating microchannels, and to define a critical rotational Reynolds number, above which the effect of secondary flow becomes dominant.
4. To investigate how liquid slip in hydrophobic or superhydrophobic surfaces reduces the drag in a rotating microchannel flow, and how the convective heat transfer is affected by a combined influence of rotation and liquid slip.
5. To couple a level set method with the finite volume solver in order to incorporate the microscale effects in two-phase flow simulations.

1.5 Organization

The dissertation is organized as follows. Chapter 2 presents the numerical methodology used to solve the incompressible Navier-Stokes equations. Chapter 3 describes the parallelization technique of the finite volume solver using distributed memory processors. The development of a non-linear multigrid solver and its parallel performance is presented in chapter 4. The analysis of three-dimensional steady flows in rotating microchannels is presented in chapter 5. The effects of the liquid slip boundary condition on rotating microchannel flows are described in chapter 6. Chapter 7 presents a level set method to capture the interface during two phase flow simulations. In chapter 8, the primary contributions of this research work will be summarized.

2. NUMERICAL METHODOLOGY

2.1 Governing Equations

The conservation equations of mass, momentum and energy for an unsteady, incompressible flow can be expressed in the following vector form:

$$\nabla.\mathbf{V} = 0 \tag{2.1}$$

$$\frac{\partial \mathbf{V}}{\partial t} + \mathbf{V}.(\nabla \mathbf{V}) = -\frac{1}{\rho}\nabla p + \frac{1}{\rho}\nabla.(\mu \nabla \mathbf{V}) + S \tag{2.2}$$

$$\frac{\partial T}{\partial t} + \mathbf{V}.(\nabla T) = \frac{1}{\rho c_p}\nabla.(-k\nabla T) \tag{2.3}$$

Equation 2.1 is the continuity equation for an incompressible flow which ensures a divergence free velocity field. Equation 2.2 is the so called Navier-Stokes equations which contain an unsteady term and a convective term on the left hand side and a pressure gradient term and viscous diffusion term on the right hand side. For constant properties fluid and laminar flow, the convective term is the only non-linear term in the Navier-Stokes equation. Equation 2.3 is the thermal energy equation for constant thermal properties fluid, which is unsteady and linear in nature.

If we closely examine the momentum and energy equations, we can find that both of them share some common features e.g. unsteadiness, convective terms, viscous terms and source terms. As a result, we can express them in the following generic flux variable form [37]:

$$\frac{\partial}{\partial t}(\rho\phi) + \nabla.(\rho\mathbf{V}\phi) = \nabla.(\Gamma\nabla\phi) + S \tag{2.4}$$

Here, Γ is the diffusion coefficient and S is the source or sink term. The scalar variable

ϕ can represent velocities (e.g. u, and v in 2D) or temperature (T). The advantage of expressing the governing equations in generic scalar form is that once we formulate a discretization method in order to numerically solve this generic equation, then the method is readily applicable to all the governing equations.

Before describing the discretization, we note that, the pressure variable only appears in the momentum equations. For a compressible flow, the equation of continuity carries a density term and the pressure is related to density by the equation of state. Consequently, the pressure can be calculated explicitly from the equation of state at each time step and the numerical solution can be marched in time. But, in case of incompressible flow, density is not present in the equation of continuity. As a result, there is no way pressure can be calculated explicitly. This poses a serious difficulty in solving the incompressible Navier-Stokes equations. Fortunately, this problem was first overcome by Harlow and Welch [39] and later by Spalding and Patankar [40], where at each time step momentum equations are solved iteratively by guessing the pressure and correcting the other primitive variables accordingly. This is the so called semi-implicit pressure linked equation (SIMPLE) method which is the basis of current pressure based solvers for incompressible flow.

2.2 Finite Volume Discretization

In this section, we will describe the finite volume discretization scheme of the generic scalar equation. While discretizing the momentum equations, a straightforward application of central difference scheme to the pressure gradient term can result in a checkerboard type pressure field, which might be a wrong depiction of the reality. Similarly, the discretization of the first derivative of velocity terms in the continuity equation can lead us to a non-physical wavy velocity field as a solution. One remedy of this problem is to discretize the pressure and velocity variables in a staggered grid, which was first proposed by Harlow and Welch [39]. However, the book-keeping of all the variables in displaced locations of a staggered grid is cumbersome and difficult, especially for parallel algorithms, multi-grid techniques or curvilinear coordinates. The main reason for failure of early attempts to use the collocated grid approach was the delinking of the pressure and velocities at the node of a given control volume when discretizing the pressure gradient terms in the momentum equations. Rhie and Chow [41] developed a special interpolation technique to calculate velocities at the control volume faces of a collocated grid. The special interpolation technique is known as 'momentum interpolation.' Instead of linear interpolation at the control volume interfaces, it uses discretized momentum equations of two adjacent control volumes to calculate the face velocities. Figure 2.1 shows a typical two-dimensional (2D) control volume for the collocated grid approach. The two-dimensional velocity vector $\mathbf{V}$ contains the x-component u and the y-component v, i.e., $\mathbf{V} = (u, v, 0)$. It can be seen from this figure that both pressure p and velocities u and v are computed at the same node. On the other hand, in a staggered grid, the pressure p is located in the control volume nodes whereas the velocities u and v are located in the control volume faces. In this work, both staggered and collocated grid approaches have been applied to build the finite volume solvers. However, we will describe only the collocated grid algorithms since the staggered grid algorithms are well documented in the literature [37].

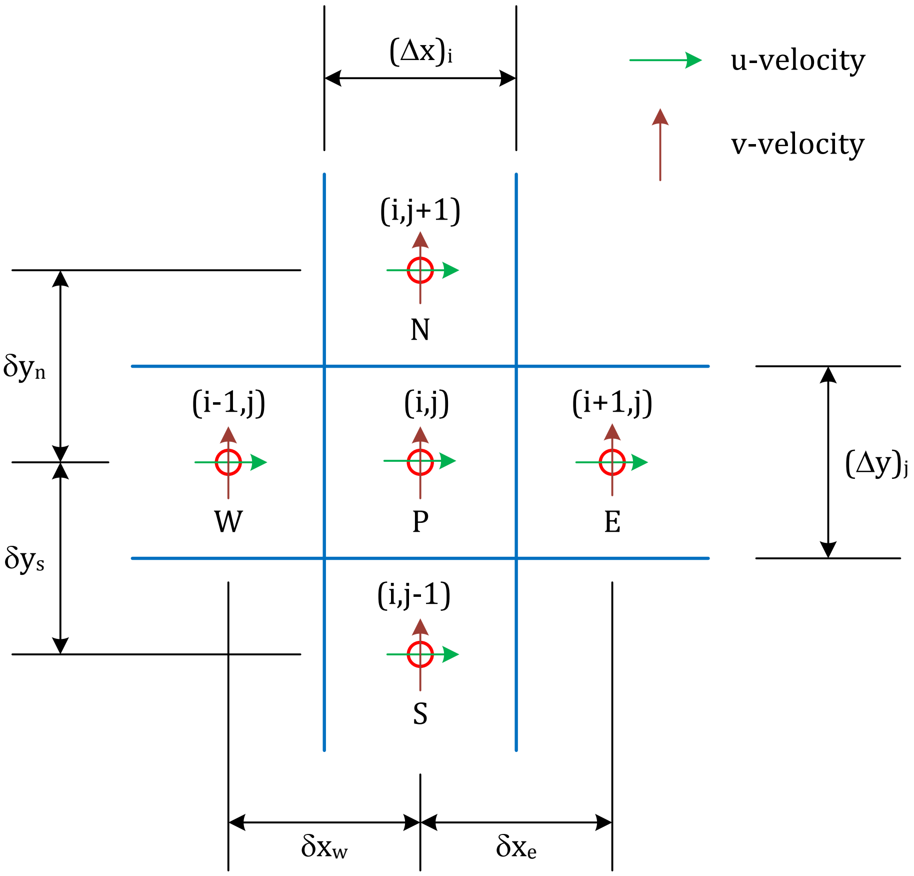

Figure 2.1: A typical control volume (CV) in a collocated grid approach

Equation 2.4 can be rearranged in the following way:

$$\frac{\partial}{\partial t}(\rho\phi) = -\nabla.(\rho\mathbf{V}\phi) + \nabla.(\Gamma\nabla\phi) + S \tag{2.5}$$

The above equation can be integrated over the control volume:

$$\int_{CV} \frac{\partial}{\partial t}(\rho\phi)\mathrm{d}\mathcal{V} = -\int_{CV} \nabla.(\rho\mathbf{V}\phi)\mathrm{d}\mathcal{V} + \int_{CV} \nabla.(\Gamma\nabla\phi)\mathrm{d}\mathcal{V} + \int_{CV} S\mathrm{d}\mathcal{V} \tag{2.6}$$

If a backward Euler scheme is applied to discretize the transient term, then the two-dimensional discretized equation can be written in the following form [37]:

$$a_P\phi_P = a_E\phi_E + a_W\phi_W + a_N\phi_N + a_S\phi_S + b \tag{2.7}$$

where,

$$a_E = D_e A(|P_e|) + \max(-F_e, 0) \tag{2.8a}$$

$$a_W = D_w A(|P_w|) + \max(F_w, 0) \tag{2.8b}$$

$$a_N = D_n A(|P_n|) + \max(-F_n, 0) \tag{2.8c}$$

$$a_S = D_s A(|P_s|) + \max(F_s, 0) \tag{2.8d}$$

$$b = S_C\Delta x\Delta y + \frac{\rho\Delta x\Delta y}{\Delta t} \tag{2.8e}$$

$$a_P = a_E + a_W + a_N + a_S - S_P\Delta x\Delta y + \frac{\rho\Delta x\Delta y}{\Delta t} \tag{2.8f}$$

Here, F_e, F_w, F_n, and F_s are the mass flow rates and D_e, D_w, D_n, and D_s are the diffusion conductance through the east, west, north and south faces of the control volume, respectively. If ρu is assumed to be uniform over the whole interface, we can write:

$$F_e = (\rho u)_e\Delta y,\ F_w = (\rho u)_w\Delta y,\ F_n = (\rho v)_n\Delta x,\ F_s = (\rho v)_s\Delta y \tag{2.9}$$

The corresponding conductances are defined by:

$$D_e = \frac{\Gamma_e\Delta y}{\delta x_e},\ D_w = \frac{\Gamma_w\Delta y}{\delta x_w},\ D_n = \frac{\Gamma_n\Delta x}{\delta y_n},\ D_s = \frac{\Gamma_s\Delta x}{\delta y_s} \tag{2.10}$$

P is the Peclet number which is defined by the ratio of the strengths of convection (F) and diffusion (D). Thus, at the control volume faces the corresponding Peclet numbers are:

$$P_e = \frac{F_e}{D_e},\ P_w = \frac{F_w}{D_w},\ P_n = \frac{F_n}{D_n},\ P_s = \frac{F_s}{D_s} \tag{2.11}$$

The function $A(|P|)$ is calculated by using a power law scheme (PLS) or a central difference scheme (CDS) by the following formula:

$$PLS:\ A(|P|) = max\left(0, (1 - 0.1|P|)^{0.5}\right) \tag{2.12}$$

$$CDS:\ A(|P|) = max\left(0, (1 - 0.5|P|)\right) \tag{2.13}$$

The source term S in Equation 2.6 is linearized by:

$$S = S_C + S_P \phi_P \tag{2.14}$$

Equation 2.7 is the discretized form of the Navier-Stokes equations where the value of the variable ϕ at point P (refer to 2.1) is calculated from the neighboring ϕ variables at points E, W, N, and S. The coefficients a_E, a_W, a_N, and a_S carry the information of convection and diffusion from the neighboring points of P. The non-linearity of the Navier-Stokes equations are also buried in these coefficients. Although the pressure gradient term is considered as a source term and included in the expression of b, it needs special treatment which will be discussed in the subsequent subsections.

Due to the strong non-linear and coupled nature of the momentum equations, the above discretization method may not result in a converged solution. To avoid divergence, it is a common practice to use an under-relaxation factor in the discretized equation which slows down the actual convergence rate but in the mean time ensures a stable solution [37,42]. Incorporating an under-relaxation factor (α_ϕ) in Equation

2.7 for a node (i,j) and rearranging, we get:

$$\phi_{i,j} = (1-\alpha_\phi)\phi^l_{i,j} + \frac{\alpha_\phi}{a_{i,j}}[H_{i,j} + b_{i,j}] \tag{2.15}$$

where

$$H_{i,j} = a_{i+1,j}\phi_{i+1,j} + a_{i-1,j}\phi_{i-1,j} + a_{i,j+1}\phi_{i,j+1} + a_{i,j-1}\phi_{i,j-1} \tag{2.16}$$

Here, $\phi^l_{i,j}$ is the value of ϕ at node (i,j) from the previous iteration. Also, note that, the neighboring points E, W, N, and S are substituted by the corresponding grid locations.

2.2.1 Calculation of CV Face Velocities

As stated earlier, in order to avoid the checkerboard pressure or velocity, a momentum interpolation method first proposed by Rhie and Chow [41] has been used to calculate the face velocities. In case of the east face of the cell (i,j), the interpolated face variable has the following form [43]:

$$\phi_{e_{i,j}} = (1-\alpha_\phi)\phi^l_{e_{i,j}} + \frac{\alpha_\phi}{\bar{a}_{e_{i,j}}}[\bar{H}_{e_{i,j}} + \bar{b}_{e_{i,j}}] \tag{2.17}$$

The terms with over-bars represent interpolated values at the east face of the control volume. These interpolated values can be calculated by the following linear interpolation formulas:

$$\frac{1}{\bar{a}_{e_{i,j}}} = \frac{f_e}{a_{i,j}} + \frac{(1-f_e)}{a_{i+1,j}} \tag{2.18a}$$

$$\bar{H}_{e_{i,j}} = f_e H_{i,j} + (1-f_e)H_{i+1,j} \tag{2.18b}$$

$$\bar{b}_{e_{i,j}} = f_e b_{i,j} + (1-f_e)b_{i+1,j} \tag{2.18c}$$

where the interpolation factor f_e is calculated by:

$$f_e = \frac{\Delta x_{i+1}}{\Delta x_i + \Delta x_{i+1}} \tag{2.18d}$$

2.2.2 Correction of Velocity and Pressure Fields by Enforcing Incompressibility Condition

The calculated interface velocities in the previous subsection will not, in general, satisfy the continuity equation (Eq. 2.1). Thus, the velocity and pressure fields have to be corrected in each iteration. In order to accomplish this, a pressure correction equation is solved, which can be derived by expressing the velocities as a summation of a guessed value ($u*$) and a correction term (u') i.e. $u = u^* + u'$ and substituting them into the continuity equation. After re-arrangement, the equation for the pressure correction p' takes the following form:

$$a^{pc}_{i,j} p' = a^{pc}_{i+1,j} p'_{i+1,j} + a^{pc}_{i-1,j} p'_{i-1,j} + a^{pc}_{i,j+1} p'_{i,j+1} + a^{pc}_{i,j-1} p'_{i,j-1} + b^{pc}_{i,j} \tag{2.19}$$

where

$$a^{pc}_{i+1,j} = \rho \frac{(\Delta y)_j}{\bar{a}_{e_{i,j}}} (\Delta y)_j \tag{2.20a}$$

$$a^{pc}_{i-1,j} = \rho \frac{(\Delta y)_j}{\bar{a}_{w_{i,j}}} (\Delta y)_j \tag{2.20b}$$

$$a^{pc}_{i,j+1} = \rho \frac{(\Delta x)_i}{\bar{a}_{n_{i,j}}} (\Delta x)_i \tag{2.20c}$$

$$a^{pc}_{i,j-1} = \rho \frac{(\Delta x)_i}{\bar{a}_{s_{i,j}}} (\Delta x)_i \tag{2.20d}$$

$$b^{pc}_{i,j} = \rho(u^*_w - u^*_e)(\Delta y)_j + \rho(v^*_s - v^*_n)(\Delta x)_i \tag{2.20e}$$

The a-coefficients with over-bars are calculated from Equation 2.18a. The source term for pressure (Equation 2.20e) represents the mass imbalance of the CV at node (i,j). Once the solution of the pressure correction equation (Eq. 2.19) is obtained, the interface velocities are corrected with the following expressions:

$$u_{e_{i,j}} = u^*_{e_{i,j}} + \frac{(\Delta y)_j}{\bar{a}_{e_{i,j}}}(p'_{i,j} - p'_{i+1,j}) \tag{2.21a}$$

$$u_{w_{i,j}} = u^*_{w_{i,j}} + \frac{(\Delta y)_j}{\bar{a}_{w_{i,j}}}(p'_{i-1,j} - p'_{i,j}) \tag{2.21b}$$

$$v_{n_{i,j}} = v^*_{n_{i,j}} + \frac{(\Delta x)_i}{\bar{a}_{n_{i,j}}}(p'_{i,j} - p'_{i,j+1}) \tag{2.21c}$$

$$v_{s_{i,j}} = v^*_{s_{i,j}} + \frac{(\Delta x)_i}{\bar{a}_{s_{i,j}}}(p'_{i,j-1} - p'_{i,j}) \tag{2.21d}$$

Similarly, the nodal velocities are corrected:

$$u_{i,j} = u^*_{i,j} + \frac{(\Delta y)_j}{a_{i,j}}(p'_w - p'_e) \tag{2.22a}$$

$$v_{i,j} = v^*_{i,j} + \frac{(\Delta x)_i}{a_{i,j}}(p'_s - p'_n) \tag{2.22b}$$

The nodal pressures are corrected by the following equation:

$$p_{i,j} = p^*_{i,j} + \alpha_p p'_{i,j} \tag{2.23}$$

where α_p is the under-relaxation factor for pressure. The interface pressures p'_w, p'_e, p'_s and p'_n are calculated by an interpolation of the nodal values. The interpolation technique is similar to Equation 2.18c.

2.2.3 Convergence Criteria

Once the pressure and velocities are corrected, the relative changes of these variables over two consecutive iterations are monitored to check convergence. The details of the calculation for convergence criteria can be found in [44]. In this paper, the relative residuals for the generic variables (u, v, and T) are calculated by the following formula:

$$R_\phi = \frac{1}{\sum\limits_{CVs} |a_{i,j}\phi_{i,j}|} \sum_{CVs} |a_{i,j}\phi_{i,j} - (a_{i+1,j}\phi_{i+1,j} + a_{i-1,j}\phi_{i-1,j} + a_{i,j+1}\phi_{i,j+1} + a_{i,j-1}\phi_{i,j-1} + b_{i,j})| \tag{2.24}$$

For a converged pressure field, the only solution to the pressure correction equation is a trivial solution. Thus, instead of checking the relative change in the values of the pressure correction variable, we check the change in residual for mass imbalance b^{pc} (refer to Equation 2.19). The relative residual for mass conservation is:

$$R_{pc} = \frac{\sum\limits_{CVs} |\rho(u_w - u_e)(\Delta y)_j + \rho(v_s - v_n)(\Delta x)_i|}{\rho u_{ref} L_{ref}} \tag{2.25}$$

where u_{ref} is a characteristic or reference velocity and L_{ref} is a reference length, the values of which depend on the geometry and boundary conditions.

3. PARALLEL IMPLEMENTATION*

3.1 Introduction

With the rapid progress of computers in the past few decades, high performance computing (HPC) has become an efficient tool to perform numerical simulations. At present, researchers are conducting simulations in peta-scale parallel computers and looking forward to the next generation exa-scale supercomputers, which will enable them to run simulations in millions of processors. Computational fluid dynamics (CFD) is an ideal candidate to use the power of HPC because an enormous amount of computing power is needed to resolve the wide range of time and length scales of fluid flows. This is due to the unsteady, non-linear, multi-scale and chaotic nature of the Navier-Stokes equations, that govern the fluid flow phenomena. The effective use of HPC requires an in-depth knowledge on the parallel programming techniques. In this chapter we will discuss different parallel programming methods, describe the parallel implementation of the finite volume algorithm and analyze the parallel performance of the proposed algorithm.

3.2 Parallel Programming Methods

In order to parallelize the finite volume algorithm described in the previous chapter, two options have been considered:

(a) Shared memory parallelization

(b) Distributed memory parallelization

---

*Part of this chapter is reprinted with permission from P. Roy, N. K. Anand, and D. Donzis. A parallel multigrid finite volume solver in collocated grid for incompressible Navier-Stokes equations. *Numerical Heat Transfer, Part B: Fundamentals* (in press). Copyright 2014 by Taylor & Francis.

In a shared memory multiprocessor, variables are stored in a shared address space and each processor can access the same variables with relatively low overheads. As a result, parallel extension of a serial code in a shared memory multiprocessor is straightforward. OpenMultiProcessing (OpenMP) is a standard application programming interface (API) for shared memory parallelization. Barbosa et al. [45] used OpenMP to parallelize a SIMPLE based finite volume algorithm in a staggered grid to study the mixed convection over a three-dimensional backward facing step. Although shared memory parallelization is easy to implement, it becomes increasingly difficult and expensive to increase the number of processors arbitrarily in a shared memory system.

On the other hand, in a distributed memory multiprocessor, each processor has its own memory module to store the variables and the modules are connected through a high speed communication network. There is no concept of global address space and if one processor needs to access data from another processor, they have to communicate explicitly. This makes the programmer responsible for maintaining all the details of the communication in a distributed memory architecture. Message passing interface (MPI) is a standard API for inter-process communication in distributed memory multiprocessors. Although great care is needed to perform parallelization with MPI, very efficient and scalable programs can be written using this message passing paradigm in distributed memory multiprocessors [46, 47]. In the following subsections we will describe the parallel implementation of the finite volume solver developed in Chapter 2 by using MPI. For detailed descriptions of the shared memory parallelization and the distributed memory parallelization techniques, the readers are referred to [48] and [49].

3.2.1 Domain Decomposition

The first step towards parallelization is to decompose the computational domain into a number of sub-domains and assign them to different processors. Figure 3.1 presents how the domain is decomposed in two processors. Each processor exchanges data at the corresponding sub-domain boundaries. To accommodate this exchange of data at the boundaries, each boundary node has an extra ghost node for each sub-domain and they overlap each other. In the serial FVM code, the discretized algebraic equations were solved by a line by line method, which is a combination of iterative Gauss-Seidel method and Tri-diagonal matrix algorithm (TDMA). The use of the under-relaxation factor makes the Gauss-Seidel method effectively a weighted Jacobi iteration method. In a two-dimensional line by line method, a tri-diagonal matrix is formed along a chosen line (say in x-direction) and it is solved directly by TDMA. Then a sweeping is performed along the other direction (say in y-direction) for each line. By solving the tri-diagonal matrix system along a line, the boundary conditions are transmitted into the interior points. After one whole sweep in a fixed direction, we can alternate the direction in which TDMA sweeping is employed. In this process, we can quickly bring the information from all the boundaries into the interior of the domain [37]. The switching of directions in a line by line method can accelerate the numerical solution especially for elliptic problems with Dirichlet boundary conditions. For a parallel code, this is difficult to employ since the sub-domain has to be transposed alternatively in order to employ the line by line TDMA in both directions (Figure 3.2). MPI provides a useful collective communication operation (*MPI_Alltoall*) to perform a domain transpose. To properly conduct the domain transpose in different processors, three steps are needed: (i) a local in-core transpose, (ii) an *MPI_Alltoall* operation, and (iii) another local in-core transpose.

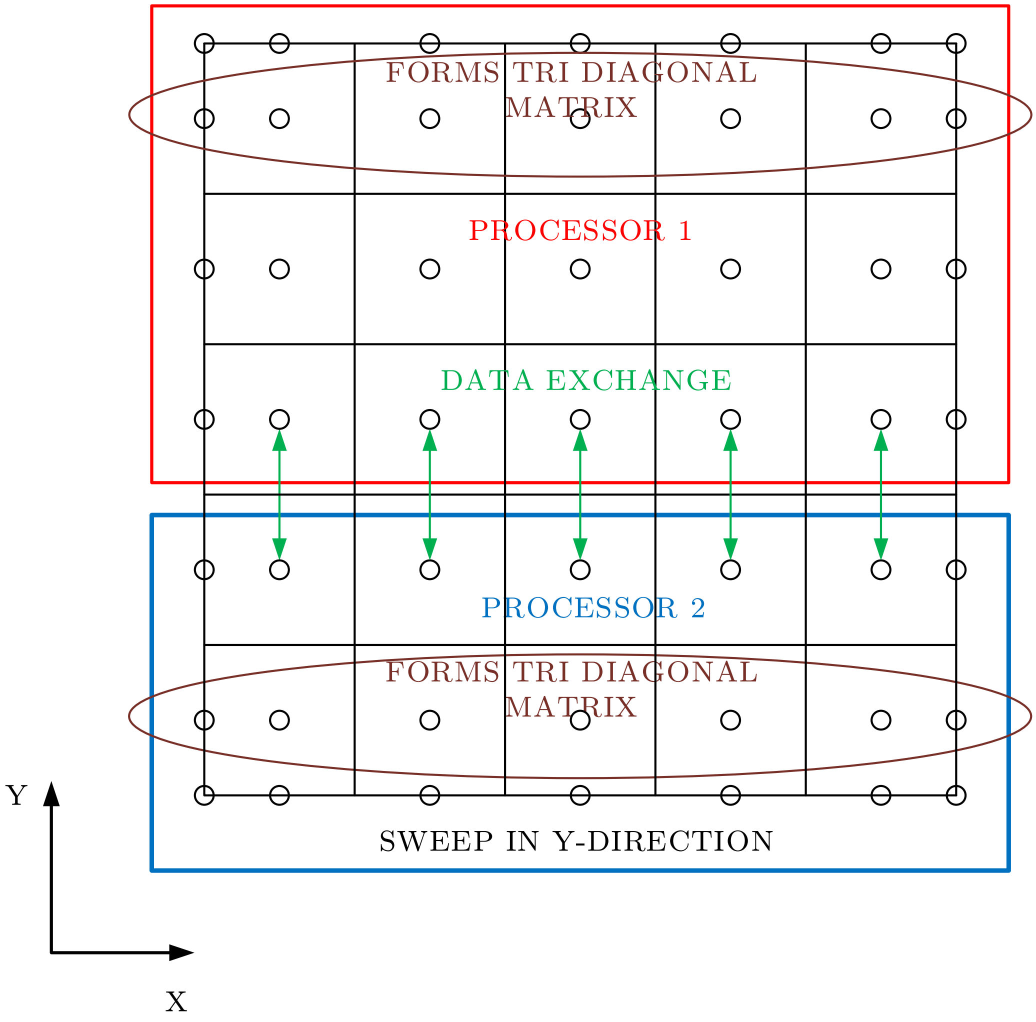

Figure 3.1: Domain decomposition of a 5 × 5 CV grid

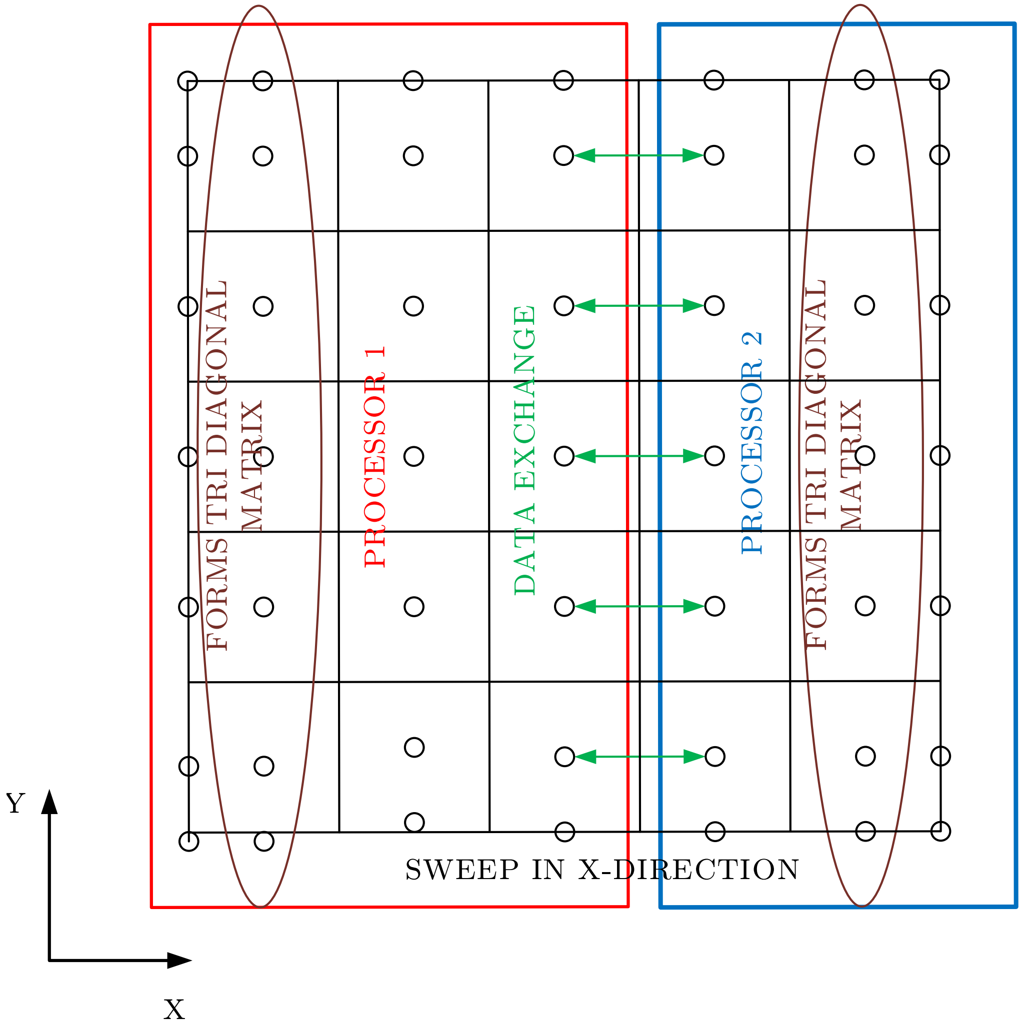

Figure 3.2: Domain decomposition with a transposed 5 × 5 CV grid

However, the iterative solver for momentum equations will call *MPI_Alltoall* function every time the domain needs to be transposed. Since it may take thousands of iterations to get a converged solution at each time step, transposing the domain can highly increase the communication overhead which may adversely affect the parallel performance of the code. Another limitation of domain transpose is that the number of grid points must be a multiple of the number of processors. This problem can be overcome by using an *MPI_Alltoallv* function which allows different processors to send a different amount of data and provide displacements for the input and output messages, increasing significantly the complexity of the code. Taking all these issues into consideration, domain transpose was avoided and sweeping along only one direction was performed.

3.2.2 Parallel Algorithm

The following sequence of instructions is carried out by the processes:

1. Read the input data with root processor (processor 0).
2. Broadcast the input data from root processor to all other processors.
3. Perform domain decomposition i.e. map the domain into different processors.
4. Calculate all the relevant thermo-fluid properties, diffusion lengths, and control volume lengths.
5. Initialize the data in all processors. Store guessed values for pressure and interface velocities.
6. Impose boundary conditions.
7. Compute the momentum coefficients for u an v velocities by using equations 2.8 through 2.13.
8. Solve the tri-diagonal matrix system of equations for each line in x-direction and traverse in y-direction. Exchange the updated values of u and v at the sub-domain

boundaries.

9. Exchange the values of a_P, H_u and H_v at the sub-domain boundary nodes. These values will be used in the subsequent calculations for momentum interpolation coefficients.

10. Calculate the face velocities at each control volume by using the momentum interpolation technique in Equation 2.17 in fine grid.

11. Calculate the coefficients of the pressure correction equation by using Equation 2.20.

12. Solve the pressure correction equation (Eq. 2.19) using an iterative solver e.g. line by line method.

13. Correct the interface velocities using nodal pressure correction values by applying equations 2.21a – 2.21d.

14. Correct the pressure variables at each node using Equation 2.23 .

15. Correct the nodal velocities using equations 2.22a and 2.22b. For evaluating these equations we will need to interpolate the pressure corrections at interfaces, which is similar to Equation 2.18c.

16. Solve for other scalar variables such as temperature, species concentration, and the like.

17. Calculate the relative residuals by using equations 2.24 and 2.25. Perform a collective reduction operation using *MPI_Allreduce*[1] to get the summation of the relative residuals.

18. Check for convergence. If the solution is converged, go to step 19.

19. Store the velocities from the previous time step. If instructed, write the output into a file. Proceed to the next time step.

---

[1] *MPI_Allreduce* combines data from all processes and distributes the reduced data back to all processes [50]

3.3 Code Validation

Lid driven cavity flow has been widely used as a benchmark problem to validate and verify incompressible Navier-Stokes solvers. The geometric simplicity coupled with rich flow physics and the ease of applying boundary conditions make it a suitable candidate for benchmarking the code. The parallel finite volume code has been tested and validated in several steps. First, the lid driven cavity flow problem was solved using 10 × 10 control volumes. Both left and right plates were maintained at the same velocity and no slip boundary conditions were applied to all boundaries. The symmetry of the steady state solution in the u and v-velocities were checked. Figure 3.3 presents the normalized centerline v-velocity along the x-axis. The symmetry of the solution was confirmed up to six decimal places. Then the number of processors was increased to check that the results are processor independent.

Additionally, the unsteady solution of a lid driven cavity flow with the upper plate moving at a Reynolds number of 400 has been validated against the simulation results of Ijaz [51]. From Figure 3.4, it can be observed that the present simulation results are in good agreement with the results of Ijaz [51].

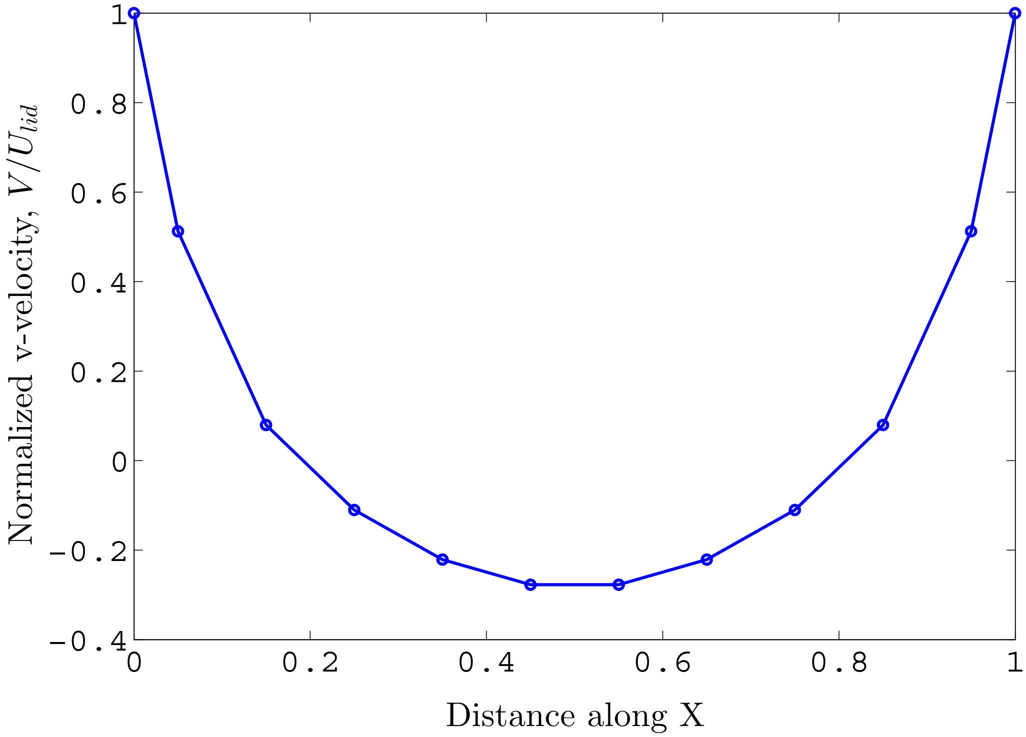

Figure 3.3: Centerline v-velocity profile along x for Re = 100 with both side plates moving at the same velocity

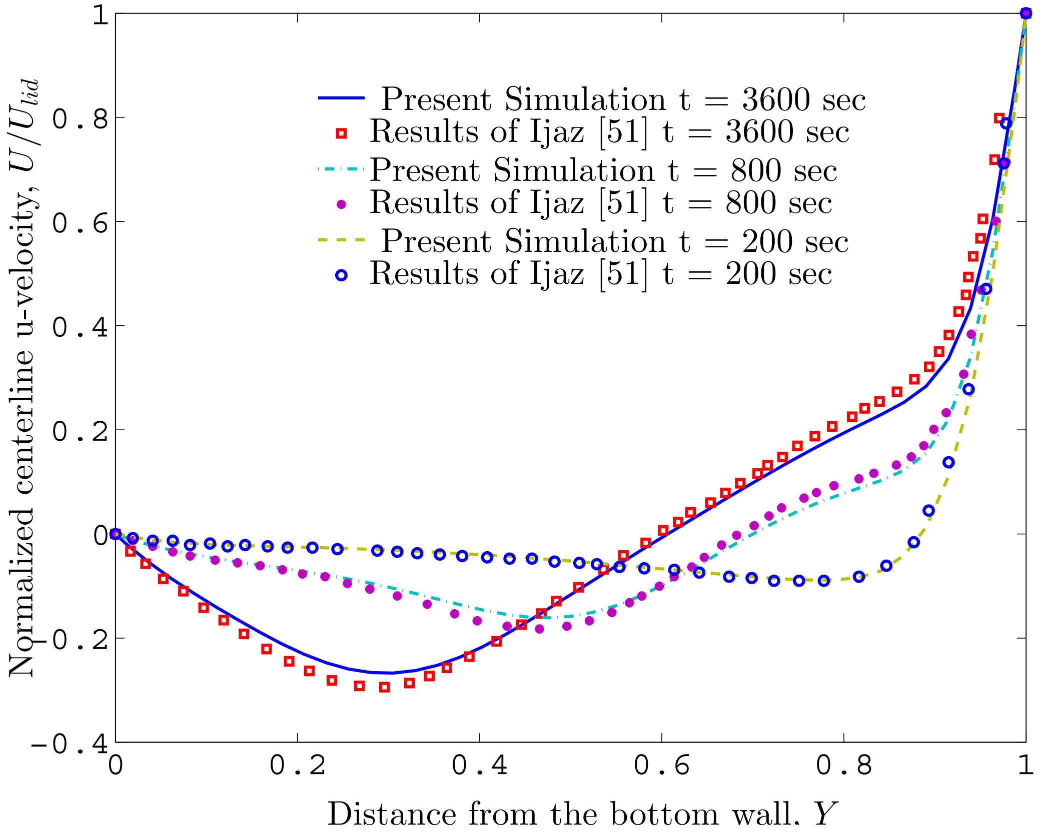

Figure 3.4: Centerline u-velocity profiles along y at different time instants with the upper plate moving at Re = 400

3.4 Parallel Performance on Single Grid

Before studying the performance of the parallel multigrid solver, a performance analysis on a single grid was conducted. Parallel scalability was assessed by performing strong scaling studies, where the number of processors is increased for a fixed problem size. In ideal scaling, the simulation time is inversely proportional to the number of processors. Departures from this ideal scaling indicate overheads associated with parallelism, such as inter-processor communication, which leads to a degradation in the efficiency of the code. In order to test the strong scaling, three grid sizes were chosen: 128×128, 256×256, and 512×512 CVs. For each case, the total CPU time, the average computation time and the average communication time were calculated. The simulations were conducted using up to 64 processors on the Texas A&M Eos supercomputer, which is an IBM Linux cluster with 8-core (Nehalem) nodes connected through a high-speed infiniband fabric.

Figure 3.5 shows the comparison of communication and computation time for a grid size of 128×128 CVs. For this coarse grid size, a good scalability is found only up to eight processors. As the number of processors increase, the communication time increases relative to the computation time which decreases on a per-core basis, resulting in a reduction of the parallel performance. Figure 3.6 shows the comparison of simulation time for a grid size of 256×256 CVs. In this case, a better scalability can be observed than the previous case, as the percentage computation time is much higher than the percentage communication time. The scalability increases up to sixteen processors and performance degrades after the choke point as the communication overhead becomes dominant. From Figure 3.7, it can be observed that strong scalability can be achieved up to sixty-four processors for a grid size of 512×512 CVs.

Figure 3.8 presents the comparison of parallel speedup for all three cases. The parallel speedup indicates how much faster the code runs using multiple processors as opposed to the single processor. It is evident from this graph that superior speedup can be achieved for finer grid size. An ideal speedup curve is a starlight-line with a unit slope, passing through the origin. For the grid size of 512×512 CVs, almost linear speedup can be observed. The reason is - for finer grid size, the ratio of computation time to the communication time is very high. Although the communication time increases with the increase in number of processors, the portion of communication overhead in comparison to the computation time is low. Therefore, as long as the communication time is a small percentage of the total execution time, good speedup is more likely to be achieved. In Figure 3.8, it can also be seen that in the case of twenty-four processors, the speedup deviated a bit from the regular trend of the curves. This might be due to the load imbalance among the processors. In the finite volume formulation, the total number of grid points is two more than the number of control volumes. So, all the grid points may not be equally distributed among the processors, which may result in a load imbalance situation.

3.5 Conclusion

A parallel finite volume solver was developed to simulate two dimensional incompressible Navier-Stokes equations. The code was tested and verified by conducting lid driven cavity flow simulations. Good parallel scaling was observed up to 64 processors for a grid size of 512×512 CVs on single grid simulations. The analysis showed that, as long as the communication time is small compared to the computation time, the parallel speedup can be achieved up to a large number of processors.

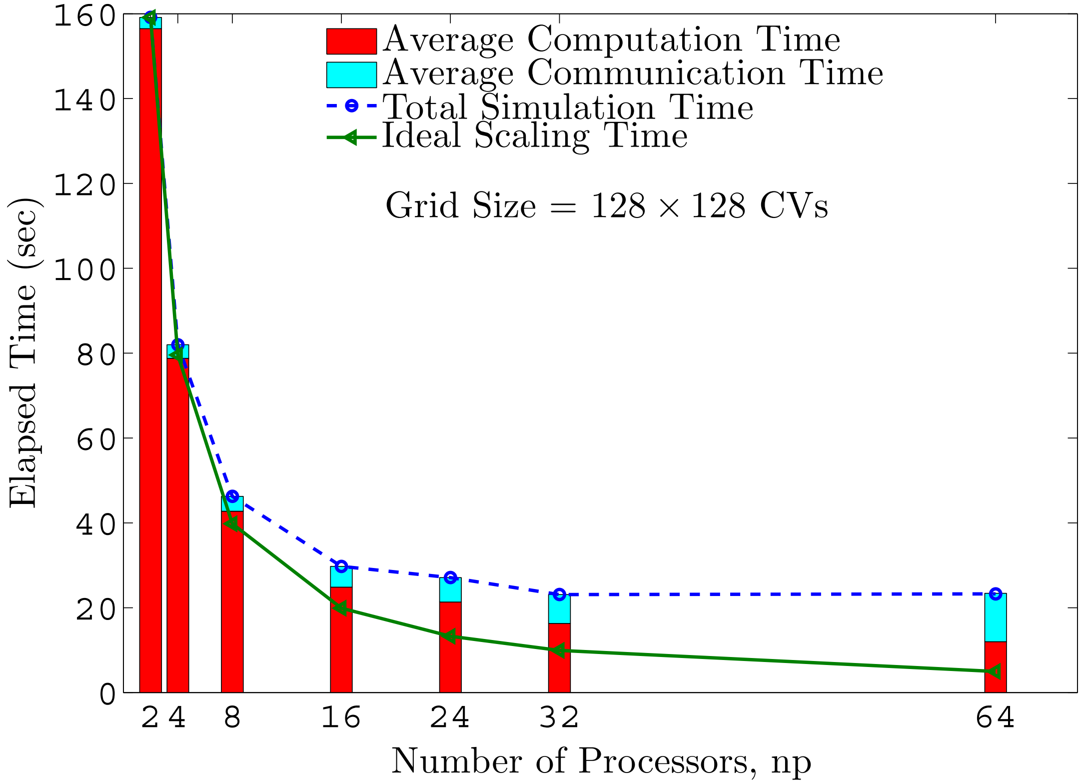

Figure 3.5: Strong scaling for lid driven cavity flow with top plate moving for 128×128 CVs ($Re = 10,000$)

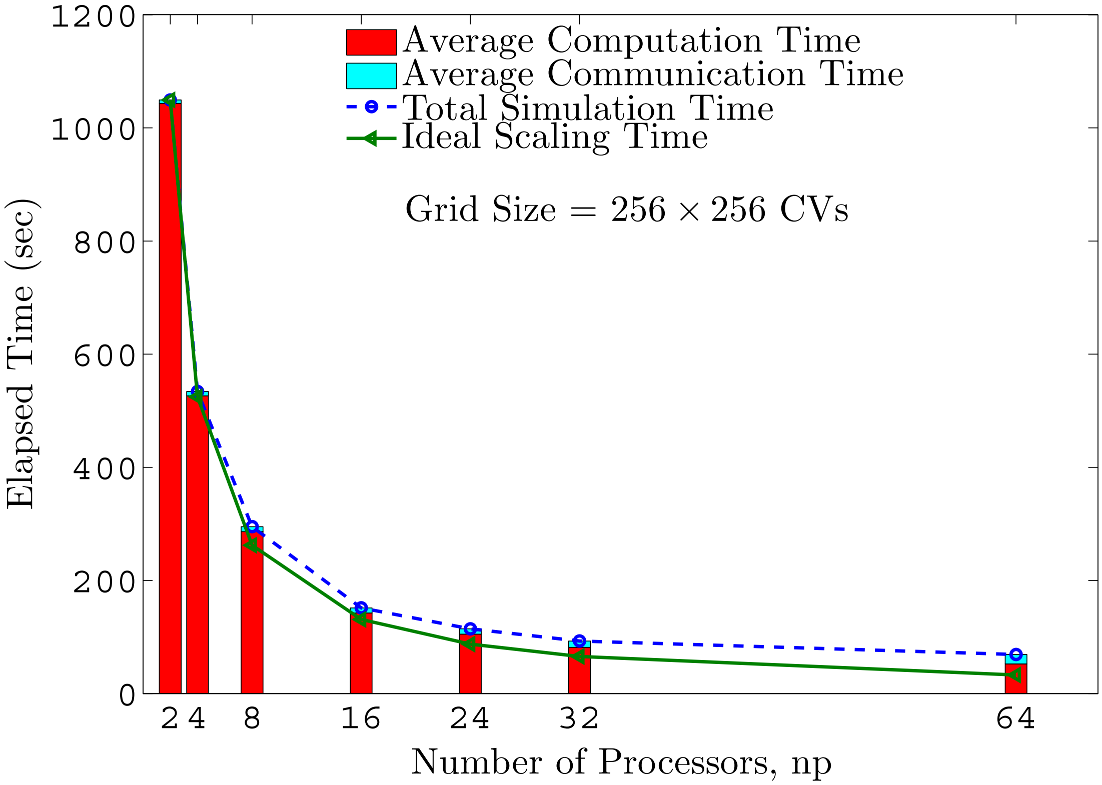

Figure 3.6: Strong scaling for lid driven cavity flow with top plate moving for 256×256 CVs ($Re = 10,000$)

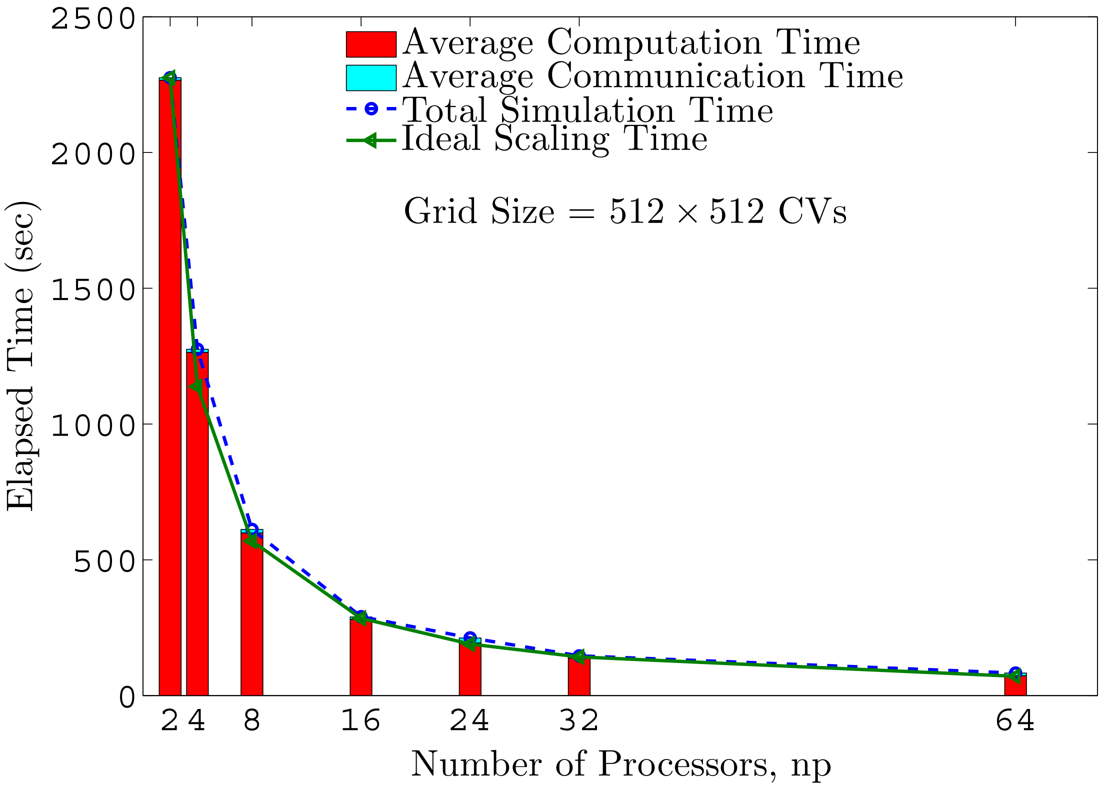

Figure 3.7: Strong scaling for lid driven cavity flow with top plate moving for 512×512 CVs ($Re = 10,000$)

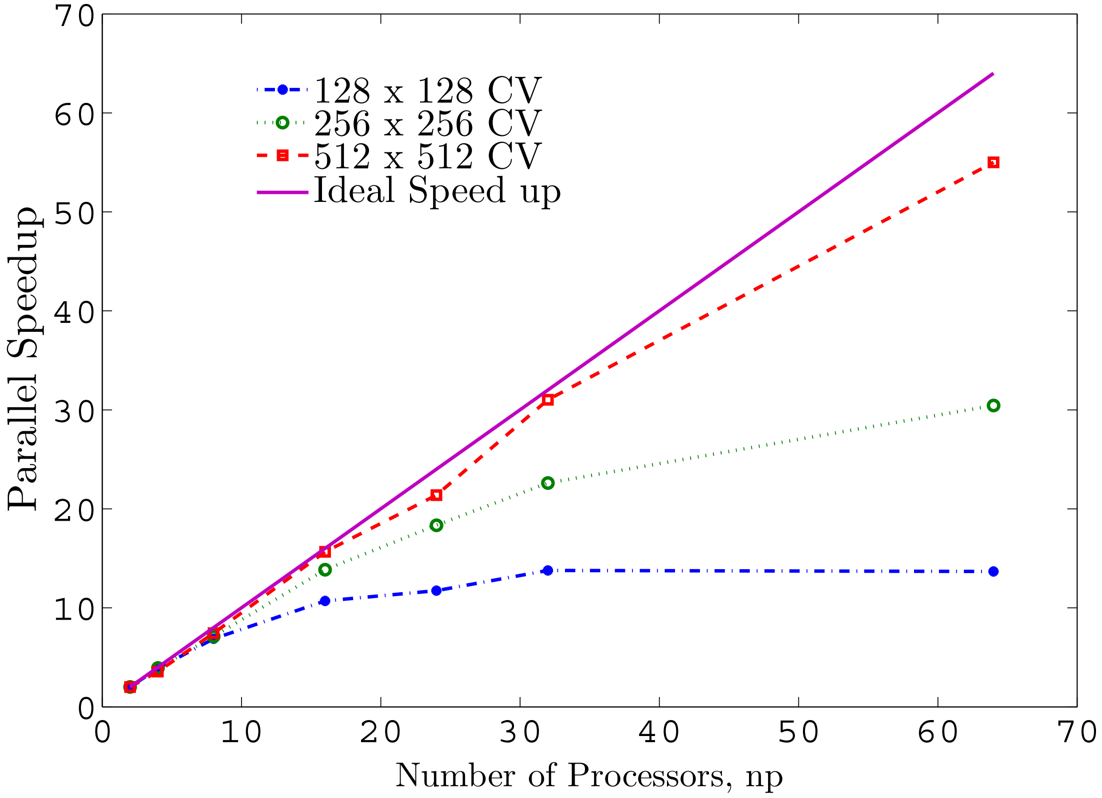

Figure 3.8: Comparison of parallel speedup with different grid sizes for lid driven cavity flow problem ($Re = 10,000$)

4. MULTIGRID TECHNIQUES*

4.1 Introduction

Multigrid methods are increasingly being used as an acceleration technique for the solution of Navier-Stokes equations. The basic idea of the multigrid technique lies on the principle of error smoothing of iterative solvers. A simple analogy can be the propagation of sound in air. The high frequency component of sound, commonly known as ‘treble’, dissipates quickly due to the friction of sound waves with the air. However, the low frequency component, known as ‘bass’ is not easily damped by the air medium and can propagate through a long distance. Few animals e.g. elephants can detect these low frequency components which helps them to communicate with each other over a long distance. The computational grid of iterative solvers act like the air medium and the solution error resembles the sound wave in this example. Similar to the sound wave, the solution error of iterative solvers are composed of high frequency components and low frequency components. During the initial phase of iterations, the iterative solvers tend to smoothen the high frequency components (treble) of the solution errors quickly, resulting in a high convergence rate. However, the low frequency parts of the solution error (bass) are not easily damped by the solver and propagates a long way before dying down completely. For this reason, the convergence rate of most iterative solvers decreases significantly after exhibiting fast convergence during the initial stage of iterations[1].

As most of the standard iterative methods tend to smoothen out the high frequency or oscillatory components of the error, they are commonly known as smoothers.

---

*Part of this chapter is reprinted with permission from P. Roy, N. K. Anand, and D. Donzis. A parallel multigrid finite volume solver in collocated grid for incompressible Navier-Stokes equations. *Numerical Heat Transfer, Part B: Fundamentals* (in press). Copyright 2014 by Taylor & Francis.

[1] A physical explanation of this smoothing property has been given in Appendix A.

After a few iterations of these smoothers, the high frequency errors are quickly eliminated while the low frequency errors remain unchanged. These low frequency errors can be adequately represented on a coarse grid due to the inherent smoothness. However, the low frequency errors in a fine grid are treated as high frequency errors in the coarse grid, and hence iterations in a coarse grid can remove the low frequency errors quickly. The basic idea of multigrid methods is to accelerate the convergence of iterative solvers by eliminating high and low frequency errors through repeated application of fine and coarse grid iterations.

As depicted by Achi Brandt [52], the golden rule of multigrid methods is the following: *"The amount of computational work should be proportional to the amount of real physical changes in the computed system."* In a single grid, the computational work increases as $O(N^d)$, where N is the number of grid points and d is the dimension of the system. Thus, for a two-dimensional system, the computational work increases quadratically whereas for a three-dimensional system, the increase is cubic in nature. The golden rule of Brandt predicts that an efficient multigrid method should be linearly dependent on the number of grid points N i.e. it should exhibit an $O(N)$ increase in the computational work. One of the objectives of this study is to achieve this $O(N)$ increase in computation time for pressure based incompressible Navier-Stokes solvers in multiple processors.

The pressure based solvers of the incompressible Navier Stokes equations rely on a predictor corrector technique to reach the final solution. As the velocity and pressure variables are not known *a priori*, guessed values are used to solve the momentum equations to predict new velocities. Since the predicted velocities are not divergence free as required by the incompressibility condition, a pressure correction equation is solved to correct them. A number of researchers investigated the application of multigrid methods in pressure based incompressible Navier-Stokes solvers. Hortmann et al. [53] presented a finite volume multigrid solution of the laminar natural convection problem in a square cavity for different Rayleigh numbers. High fidelity benchmark solutions on a grid size as fine as 640×640 were provided. As desired, the computation time for multigrid solution in a collocated grid increased linearly as the grid is refined, whereas the single grid computing time showed a quadratic increase. Lien and Leschziner [54] incorporated multigrid acceleration techniques into a non-orthogonal collocated finite volume solver for laminar and turbulent flows. Compared to single grid solution, the computation speedup for multigrid solution was as high as 70 times for 2D flows, and 10 times for 3D flows. They concluded that, the effectiveness of the multigrid scheme can be affected by the type of flow (i.e. laminar or turbulent, two-dimensional or three-dimensional), boundary conditions, turbulence-model equations and Reynolds number. A multigrid solution for lid driven cavity flow was presented in recent work by Kumar et al. [55]. Multigrid acceleration into SIMPLEC algorithm was applied in a collocated grid to produce a benchmark solution on a uniform 513×513 grid. Pressure based multigrid methods in staggered grids for recirculating and complex fluid flows were developed by Shyy and Sun [56] and Thakur et al. [57]. CPU time speedup ratio for the multigrid method was as high as 25 for second-order upwind convection scheme on a 81×81 grid. Multigrid procedures for three-dimensional laminar incompressible flows on non-orthogonal collocated grids were presented by Smith et al. [58]. They emphasized the consistent evaluation of coarse grid mass fluxes after solving the momentum equations. CPU time speedup of 4 to 5 was achieved for three-dimensional curved pipe flow. Yan and Thiele [59] developed a modified full multigrid method and applied it to the SIMPLE algorithm on collocated grids. They demonstrated a maximum speedup of 25 for lid driven square cavity flow.

In all of the above mentioned studies, segregated pressure based solvers were used to solve the incompressible flow equations. Multigrid methods were successfully applied to another type of pressure based solvers, namely coupled solvers, primarily developed by Vanka [60]. The initial attempts were limited to the staggered grid approach [60,61]. However, as the complexity of the problem and the computational power of the CPUs increased, multigrid procedures for coupled solvers in collocated grids were developed [62,63].

With the rapid progress of computers in the past few decades, parallel multigrid methods have been developed to solve large-scale computational problems. At present, researchers are conducting simulations in massively parallel computers and looking forward to the next generation of peta-scale supercomputers, which will enable them to run simulations in millions of processors. The question – whether parallel processors should be used in conjunction with multigrid methods, is justified in the review on parallel multigrid methods by Jones and McCormick [64]. Durst and Schäfer [65] presented a parallel block-structured multigrid finite volume solver for incompressible flows in complex geometries. Their results indicated that the combination of parallel computers and the multigrid acceleration technique can produce an improved computational performance. A parallel multigrid finite volume solver for three-dimensional thermal convective flows was studied by Wang and Ferraro [66]. Good parallel scaling up to 128 processors was achieved for a 128^3 grid size. However, the effect of parallel processing elements on multigrid speedup was not reported. In a recent survey on parallel multigrid solvers, Chow et al. [67] provided a brief account on the treatments of computationally efficient parallel multigrid methods. They discussed the parallel computation issues of standard multigrid algorithms such as spatial partitioning, parallel coarsening and complexity, and coarse grid solution strategy. In spite of the above mentioned studies, a comprehensive investigation on the influence of parallel processing elements on a finite volume multigrid solver in collocated grid has only been performed recently by the author [68], which forms the primary topic of this chapter. In particular, we:

(i) describe a non-linear multigrid algorithm with modified coarse grid equations using the momentum interpolation method to solve incompressible Navier-Stokes equations in collocated grid, and

(ii) develop a parallel multigrid algorithm and investigate the effect of parallel processing elements on multigrid efficiency. The chapter is arranged as follows. Section 4.2 presents the multigrid method and the derivation of the coarse grid equations using SIMPLE algorithm [37]. The parallel multigrid algorithm is described in section 4.3. The results are presented and discussed in section 4.4, and finally the conclusions are given in section 4.5.

4.2 Multigrid Algorithm

The basic principle of the multigrid algorithm is to eliminate the approximate solution error efficiently by alternatively iterating on fine and coarse grids. The first step of this algorithm is to derive a set of coarse grid equations from the existing fine grid discretized equations. It is important to note that, in the coarse grid, the original discretized equations for SIMPLE algorithm are not solved, rather correction equations are solved. Due to the non-linear nature of the governing equations, the correction equations are derived from the discretized equations for SIMPLE algorithm. This process of obtaining the correction equations is known as Full Approximation Scheme (FAS). After deriving the coarse grid correction equations with FAS, suitable grid transfer operators are chosen to interchange the coarse and fine grid values without losing essential information. Transferring the fine grid information to the coarse grid is known as *restriction*. On the other hand, transferring the coarse grid information into the fine grid is called *prolongation.* In the next subsections, these essential multigrid elements will be described.

4.2.1 Coarse Grid Equations

The system of linear equations (Eq. 2.7) can be expressed in the following form:

$$A\phi = b \tag{4.1}$$

Here, ϕ is the exact solution of the problem, A is the coefficient matrix and b is the source term. A is composed of a linear part, $L(\phi)$ (pressure difference term) and a non-linear part, $N(\phi)$ (convection-diffusion term). Thus, we can write:

$$N\phi + L\phi = b \tag{4.2}$$

After a few outer iterations (ν_1), the approximate solution ϕ^* satisfies the following equation:

$$N^*\phi^* + L\phi^* = b^* + R \tag{4.3}$$

where R is the residual. By subtracting 4.3 from 4.2, we get:

$$N\phi - N^*\phi^* + L\phi' = b - b^* - R \tag{4.4}$$

Here, ϕ' is the difference between the exact and approximate solution, i.e. $\phi' = \phi - \phi^*$. The coarse grid equation is assembled from Equation 4.4 by restricting the fine grid variables and using them as a fixed source term on the coarse grid:

$$\widehat{N}\widehat{\phi} = \widehat{b} - \widehat{L}(\phi') + \underline{\widetilde{N}\widetilde{\phi} - \widetilde{b} - \widetilde{R}} \tag{4.5}$$

The coarse grid variables are denoted by caret '$\hat{}$', and the restricted quantities are denoted by tilde '$\tilde{}$'. The underlined terms are kept frozen during the coarse grid iterations. Thus, Equation 4.5 estimates the difference $(\widehat{\phi} - \widetilde{\phi})$ that is driven by residual R. This difference $(\widehat{\phi} - \widetilde{\phi})$ is known as the coarse grid correction. In view of Equation 4.5, the coarse grid correction equations for u-velocity and v-velocity are as follows:

$$\widehat{a}_P \widehat{u}_P = \sum_{nb} \widehat{a}_{nb} \widehat{u}_{nb} + \Delta y (p'_w - p'_e) + \widehat{S}_u + \underline{\widetilde{a}_P \widetilde{u}_P - \sum_{nb} \widetilde{a}_{nb} \widetilde{u}_{nb} - \widetilde{S}_u - \widetilde{R}_u} \tag{4.6}$$

$$\widehat{a}_P \widehat{v}_P = \sum_{nb} \widehat{a}_{nb} \widehat{v}_{nb} + \Delta x (p'_s - p'_n) + \widehat{S}_v + \underline{\widetilde{a}_P \widetilde{v}_P - \sum_{nb} \widetilde{a}_{nb} \widetilde{v}_{nb} - \widetilde{S}_v - \widetilde{R}_v} \tag{4.7}$$

Denoting the underlined terms with $\widetilde{f}_u$ and $\widetilde{f}_v$, we can compute the face velocities similarly:

$$(\widehat{a}_P)_e \widehat{u}_e = \left(\sum_{nb} \widehat{a}_{nb} \widehat{u}_{nb} \right)_e + (\Delta y)_e \, (p'_P - p'_E) + (\widehat{S}_u)_e + (\widetilde{f}_u)_e \tag{4.8}$$

$$(\widehat{a}_P)_n \widehat{v}_n = \left(\sum_{nb} \widehat{a}_{nb} \widehat{v}_{nb} \right)_n + (\Delta x)_n \, (p'_P - p'_N) + (\widehat{S}_v)_n + (\widetilde{f}_v)_n \tag{4.9}$$

The coarse grid steps for SIMPLE algorithm can be summarized as follows:

1. Start with the guess:

$$\widehat{u} = \widetilde{u}, \quad \widehat{v} = \widetilde{v}, \quad p' = 0 \tag{4.10}$$

2. A number of relaxation sweeps on coarse grid momentum equations are performed to get approximate solutions $\widehat{u}^*$ and $\widehat{v}^*$.

3. Face velocities are calculated with the modified momentum interpolation method:

$$\widehat{u}_e^* = (1-\alpha_u)\widehat{u}_e^l + \frac{\alpha_u}{(\widehat{a}_P)_e}\left(\left(\sum_{nb}\widehat{a}_{nb}\widehat{u}_{nb}\right)_e + (\Delta y)_e\,(p'_P - p'_E) + (\widehat{S}_u)_e + (\widetilde{f}_u)_e\right) \tag{4.11}$$

$$\widehat{v}_n^* = (1-\alpha_v)\widehat{v}_n^l + \frac{\alpha_v}{(\widehat{a}_P)_n}\left(\left(\sum_{nb}\widehat{a}_{nb}\widehat{v}_{nb}\right)_n + (\Delta x)_n\,(p'_P - p'_N) + (\widehat{S}_v)_n + (\widetilde{f}_v)_n\right) \tag{4.12}$$

4. An equation for correction to pressure correction is solved:

$$a_P p''_P = \sum_{nb} a_{nb} p''_{nb} + b''_p \tag{4.13}$$

$$b''_p = \rho[(\widehat{u}_w^* - \widetilde{u}_w) - (\widehat{u}_e^* - \widetilde{u})](\Delta y) + \rho[(\widehat{v}_s^* - \widetilde{v}_s) - (\widehat{v}_n^* - \widetilde{v}_n)](\Delta x) \tag{4.14}$$

5. Nodal and face velocities are corrected by using p'':

$$\widehat{u}_e = \widehat{u}_e^* + \frac{(\Delta y)}{(\widehat{a}_P)_e}(p''_P - p''_E) \tag{4.15}$$

$$\widehat{v}_n = \widehat{v}_n^* + \frac{(\Delta x)}{(\widehat{a}_P)_n}(p''_P - p''_N) \tag{4.16}$$

$$\widehat{u}_P = \widehat{u}_P^* + \frac{(\Delta y)}{(\widehat{a}_P)}(p''_w - p''_e) \tag{4.17}$$

$$\widehat{v}_P = \widehat{v}_P^* + \frac{(\Delta x)}{(\widehat{a}_P)}(p''_s - p''_n) \tag{4.18}$$

Similarly, the pressure correction variables are updated through:

$$p'_P = p'_P + \alpha_p p''_P \tag{4.19}$$

6. Return to step 2 to complete one outer relaxation sweep.

The coarse grid sequence may look similar to the ones described by Lien and

Leschziner [54]. However, there is a subtle difference which lies in the expression of coarse grid face velocities. In their coarse grid formulations, the cell-face velocities become equal to the average of the node velocities when the pressure correction terms are zero. This is not the case in the present coarse grid formulation.

4.2.2 Grid Transfer Operators

In order to achieve the favorable $O(N)$ convergence behavior, as predicted by Brandt [52], a multigrid method should satisfy the *smoothing property* and the *approximation property* [69]. The smoothing property is responsible for the rapid elimination of the oscillatory or high frequency modes of the error leaving the smooth modes [70]. Most iterative solvers including the one used here (line by line method) exhibit the smoothing property. It should be noted that, although in single grid methods, this smoothing property can be seen as a serious drawback, for multigrid methods, this smoothing property is desirable. The approximation property requires that $m_P + m_R > M$, where m_P and m_R are the order of accuracy plus one for the prolongation and restriction schemes, respectively and M is the highest derivative of the variable under consideration in the governing equations [69, 71]. In the incompressible Navier-Stokes equations, M = 1 for pressure, and M = 2 for velocity components. Thus, first order accurate interpolation schemes (e.g. bilinear interpolation for a 2D problem and trilinear interpolation for a 3D problem) should be sufficient to satisfy the approximation property.

In the collocated grid arrangements, the variables are located at the center of the control volumes (CVs). In this type of cell-centered discretization, the coarse grid points do not coincide with the fine grid points (as shown in Figure 4.1). As a result, special care is needed for grid transfer operations i.e. for restriction and prolongation. A four-point average was used for restriction and a bilinear interpolation was used for

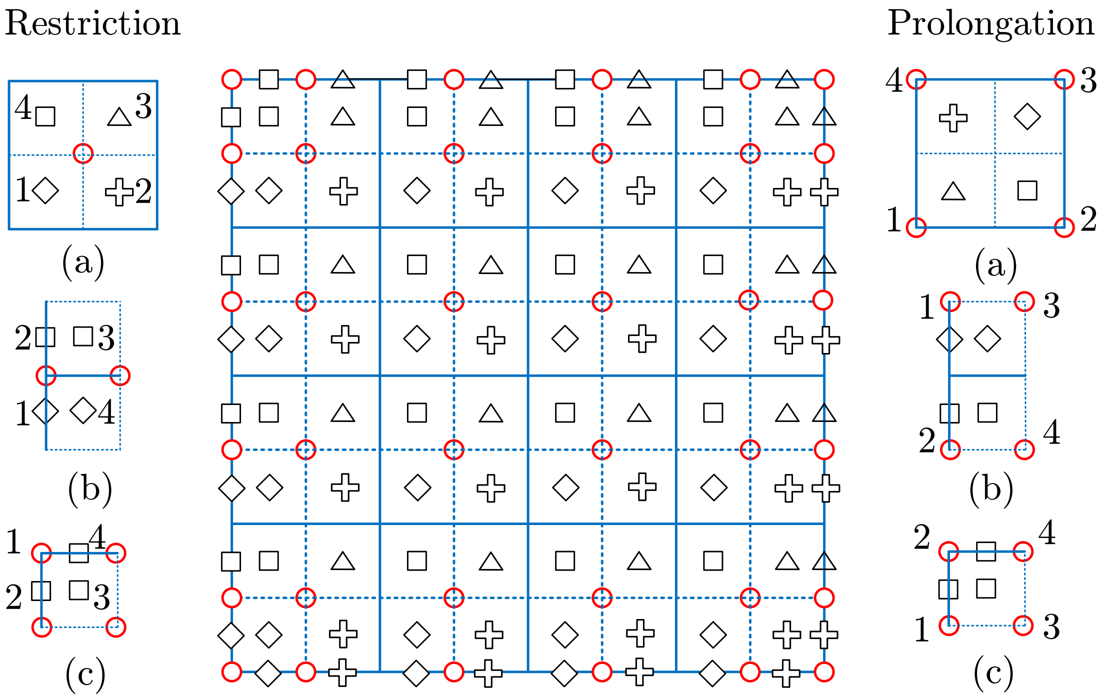

Figure 4.1: Finite volume collocated grid with symbols explaining the grid transfer operators. Red circles denote the coarse grid points and all other symbols denote the fine grid points. For restriction and prolongation: (a) Interior cells (b) West boundary cells (c) North-west cells

prolongation [54,72]. During the restriction for the 2D case, the coarse grid variables are calculated as an area-weighted average of the surrounding fine grid variables. For the 3D case, volume weighted average is used. Mathematically, the fine to coarse grid operation can be expressed as:

$$\phi^{2h} = I_h^{2h} \begin{bmatrix} \phi_1 \\ \phi_2 \\ \phi_3 \\ \phi_4 \end{bmatrix}^h \tag{4.20}$$

For inner region (excluding the boundary cells), the restriction operator is:

$$I_h^{2h} = \frac{1}{4} \begin{bmatrix} 1 & 1 & 1 & 1 \end{bmatrix} \tag{4.21}$$

For west boundary cells:

$$I_h^{2h} = \frac{1}{4} \begin{bmatrix} 2 & 2 & 0 & 0 \end{bmatrix} \tag{4.22}$$

For north-east corner cell:

$$I_h^{2h} = \frac{1}{4} \begin{bmatrix} 4 & 0 & 0 & 0 \end{bmatrix} \tag{4.23}$$

The residuals are restricted differently from the variables. In the finite volume formulations, the residuals represent flux imbalances through the CV faces. Therefore, the coarse grid residual must be computed as the sum of the surrounding fine grid residuals. The resulting prolongation operator for residuals is:

$$I_h^{2h} = \begin{bmatrix} 1 & 1 & 1 & 1 \end{bmatrix} \tag{4.24}$$

The fine grid variables are corrected in the following way:

$$\phi_h^{new} = \phi_h^{old} + \alpha_{MG}\delta\phi_h = \phi_h^{old} + \alpha_{MG} I_{2h}^h (\hat{\phi}_{2h} - \widetilde{\phi}_{2h}) \tag{4.25}$$

where, α_{MG} is an under-relaxation factor. The coarse grid to fine grid operation i.e. prolongation can be expressed as:

$$\begin{bmatrix} \delta\phi_1 \\ \delta\phi_2 \\ \delta\phi_3 \\ \delta\phi_4 \end{bmatrix}^h = I_{2h}^h \begin{bmatrix} \delta\phi_1 \\ \delta\phi_2 \\ \delta\phi_3 \\ \delta\phi_4 \end{bmatrix}^{2h} \tag{4.26}$$

The prolongation operators are as follows:

For the interior region:

$$I_{2h}^h = \frac{1}{16} \begin{bmatrix} 9 & 3 & 3 & 1 \\ 3 & 9 & 1 & 3 \\ 3 & 1 & 9 & 3 \\ 1 & 3 & 3 & 9 \end{bmatrix} \tag{4.27}$$

For west boundary cells:

$$I_{2h}^h = \frac{1}{8} \begin{bmatrix} 0 & 0 & 6 & 2 \\ 0 & 0 & 2 & 6 \\ 3 & 1 & 3 & 1 \\ 1 & 3 & 1 & 3 \end{bmatrix} \tag{4.28}$$

For north-west corner cell:

$$I_{2h}^{h} = \frac{1}{4}\begin{bmatrix} 2 & 2 & 0 & 0 \\ 0 & 0 & 0 & 4 \\ 1 & 1 & 1 & 1 \\ 0 & 2 & 0 & 2 \end{bmatrix} \tag{4.29}$$

4.2.3 Multigrid Cycles

Once the coarse grid correction equations are derived and suitable grid transfer operators are chosen, the multigrid algorithm can be applied by a recursive operation of smoothing and inter-grid transfer. This recursive process is commonly known as multigrid cycle (MGC). The most basic cycle is called a V-cycle. In a V-cycle, the fine grid errors are restricted to the coarse grid. After a few iterations, namely pre-smoothing operations, the coarse grid errors are restricted to the next coarser level. This process is continued until the coarsest grid level is reached, where the computational work for solving the residual equation is so cheap that a converged solution to the discretized equation can easily be calculated, either by using a direct solver or an iterative solver. Once the converged solution is found in the coarsest grid the error is prolongated into the next fine grid and the old error on the fine grid is corrected using this prolongated value. After a few post-smoothing operations on the corrected error, it is further prolongated to the next finer level, and the process is continued until the finest grid level is reached. A schematic of the V-cycle is shown in Figure 4.2. The down arrow indicates a restriction, whereas the up arrow indicates a prolongation. The circles at each level imply smoothing operations to obtain an approximate solution. The square box at the coarsest level signifies a converged solution of the residual equation.

There are a number of variations to the V-cycle, of which Full Multigrid (FMG)

V-cycle is the most popular one [53, 54]. Instead of starting the MG V-cycle on a given fine grid, we can first apply it on a very coarse grid, where a few number of cycles would produce converged solution. This converged solution on the coarse grid then can be prolongated on the next fine grid to provide a good initial guess to the solution of the next level. If this process is applied consecutively, then we will already have a very good initial guess when the finest grid level is reached. Thus, a faster convergence rate than a V-cycle can be achieved by using FMG V-cycle. Figure 4.3 presents a schematic of the FMG V-cycle. In terms of computational complexity, the MG V-cycle has a cost of $O(N)$, where N is the number of unknown variables in the fine grid system, as described earlier. However, the initial guess for the pressure/velocity variables introduce an error of $O(1)$, and it takes $O(NlogN)$ V-cycle operations to reduce the error below the convergence criteria [64]. Although this is a large reduction in the computational work from $O(N^d)$ operations in a single grid, it does not exactly satisfy the 'golden rule' of multigrid [52, 73]. Fortunately, this limitation is overcome by FMG V-cycle which can effectively reduce the number of operations to $O(N)$ by successively introducing good initial guesses on each fine grid.

As discussed above, during FMG V-cycle, the converged solution in the coarse grid is prolongated to the next fine grid. The prolongation can be performed in several ways, of which the bilinear interpolation described in the previous subsection and the upwind based interpolation are very common. In this work, a bilinear interpolation was used for node velocities and pressures. A momentum interpolation was applied to obtain the face velocities. It was observed that, the momentum interpolation method results in better initial guesses for the fine grid iterations than the upwind based interpolation scheme.

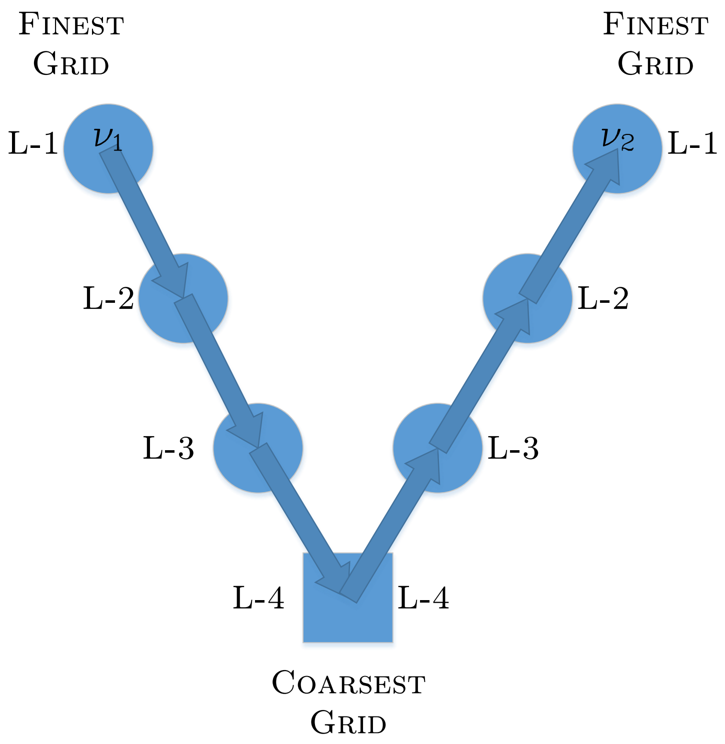

Figure 4.2: Multigrid V cycle with ν_1 pre-smoothing and ν_2 post-smoothing iterations

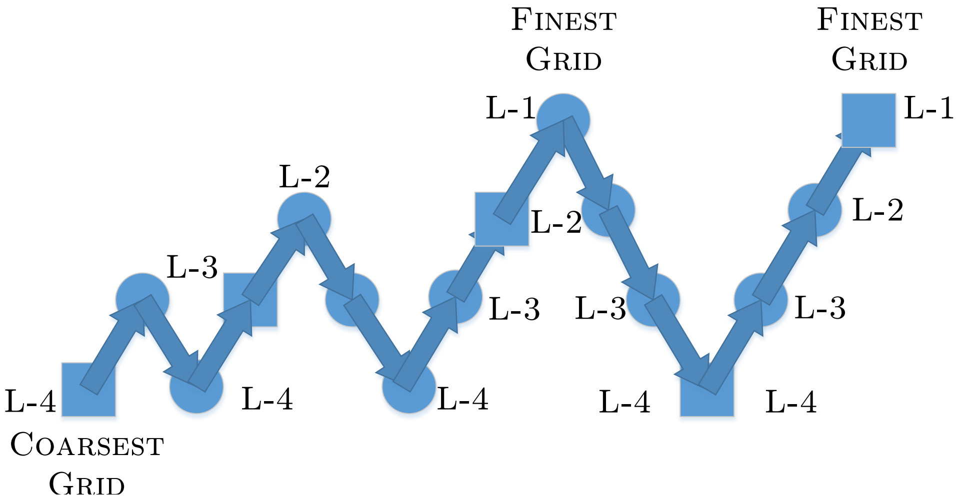

Figure 4.3: Full multigrid (FMG) V-Cycle with 4 levels

4.3 Parallel Multigrid Algorithm

The following sequence of instructions are carried out by the processes:

1. Read the input data with root processor (processor 0).

2. Broadcast the input data from root processor to all other processors.

3. Perform domain decomposition i.e. map the domain into different processors.

4. Calculate all the relevant thermo-fluid properties, diffusion lengths, and control volume lengths.

5. Initialize the data in all processors. Store guessed values for pressure and interface velocities.

6. Impose boundary conditions.

7. At each multigrid level, execute the following steps:

a) Compute the momentum coefficients for u and v velocities by using equations 2.8 through 2.13.

b) Solve the tri-diagonal matrix system of equations for each line in x-direction and traverse in y-direction. Exchange the updated values of u and v at the sub-domain boundaries.

c) Exchange the values of a_P, H_u and H_v at the sub-domain boundary nodes. These values will be used in the subsequent calculations for momentum interpolation coefficients.

d) Calculate the face velocities at each control volume by using the momentum interpolation technique in Equation 2.17 in fine grid or by equations 4.11 and 4.12 in coarse grid.

e) Calculate the coefficients of the pressure correction equation by using Equation 2.20. Use Equation 4.14 for coarse grid mass imbalance calculation.

f) Solve the pressure correction equation (2.19 in fine grid or 4.13 in coarse grid) using an iterative solver (e.g. line by line method).

g) Correct the interface velocities using nodal pressure correction values by applying equations 2.21a - 2.21d.

h) Correct the pressure variables at each node using Equation 2.23.

i) Correct the nodal velocities using equations 2.22a and 2.22b. For evaluating these equations we will need to interpolate the pressure corrections at interfaces, which is similar to Equation 2.18c.

j) Solve for other scalar variables such as temperature, kinetic energy, and the like.

k) Calculate the relative residuals by using equations 2.24 and 2.25. Perform a collective reduction operation using *MPI_Allreduce* [2] to get the summation of the relative residuals.

8. Check for convergence. If the solution is converged, prolongate the velocities and pressures into the next fine level and go to step 7. If the solution is converged at the finest multigrid level, go to step 9.

9. Store the velocities from the previous time step. If instructed, write the output into a file. Proceed to the next time step.

4.4 Results and Discussions

4.4.1 Multigrid Performance on Parallel Machines

In order to assess the multigrid performance of the parallel code, steady two-dimensional lid driven cavity flow simulations were conducted for a range of Reynolds number (Re = 100-7,500). The simulation parameters including the under-relaxation factors and the number of coarse grid iterations are tabulated in Table 4.1. It should be noted that, for high Reynolds numbers ($Re > 6,000$), the flow becomes inher-

---

[2] *MPI_Allreduce* combines data from all processes and distributes the reduced data back to all processes [50]

ently unsteady, three-dimensional, and turbulent [74]. Thus, a steady state two-dimensional laminar solution of high Reynolds number lid driven cavity flow may not be physically accurate, but has been reported in the literature for benchmarking purposes [75, 76]. Since in the coarsest level the number of grid points is very low, it is not possible to increase the number of processors arbitrarily. Otherwise, a degradation of parallel performance would happen and the number of processors may well exceed the number of coarse grid points. Therefore, in the present study, the maximum number of processors for parallel multigrid code has been limited to eight. However, there are ways to overcome this limitation. Interested readers are directed to Chow et al. [67] for a survey of specialized parallel multigrid methods.

Table 4.1: Specifications of simulation parameters

Reynolds Number	α_u	α_v	α_p	α_{pc}	α_{MG}	Coarse Grid Iterations
100	0.5	0.5	0.8	1.0	0.8	45
400	0.5	0.5	0.8	1.0	0.8	50
1,000	0.5	0.5	0.8	1.0	0.8	50
3,200	0.4	0.4	0.7	1.0	0.8	120
5,000	0.4	0.4	0.6	1.0	0.7	150
7,500	0.4	0.4	0.6	1.0	0.7	180

From this point on, single grid will be referred to by SG and multigrid by MG. Two parameters are commonly used as MG performance indicators: CPU Time and Work

Unit (WU). CPU Time is defined as the total execution time of the problem. While CPU Time is a machine dependent measurement, WU is machine independent. As shown in Figure 4.2, in one v-cycle, ν_1 iterations are performed during pre-smoothing and ν_2 iterations are performed during post-smoothing in the finest grid. One WU is defined as the computation work needed to complete one MG cycle, in this case which is $\nu_1 + \nu_2$ iterations during one outer relaxation sweep over the finest grid. Table 4.2 compares the multigrid performance of a lid driven cavity flow simulation with the top plate moving for different Reynolds numbers and grid sizes. The simulations were conducted using four processors. It can be observed that, significant speedup over single grid performance can be achieved both in CPU Time and WU with the multigrid method. As the number of grid points increases, the speedup increases. For 512×512 CVs, the CPU Time in single grid is about 400 times higher than that in multigrid. The MG performance declines with the increase of Reynolds number, which is in accordance with the findings of other researchers [54, 56]. It is surprising that, the SG/MG ratio of WU is much higher than the ratio of CPU Time in all the cases. Since WU is a machine independent measure of the work done in each MG cycle, it's ratio should be close to the speedup in CPU Time, as reported in the literature [54]. This seemingly contradictory result can be explained by looking at the communication time of the parallel processors in Table 4.3. The communication time has been presented as a percentage of total execution time for all the SG and MG cases. As shown in Table 4.3, the percentage of communication time for MG is considerably higher than that of SG due to the very few number of nodes on each processor in the coarsest MG level. Thus, for the grids under consideration, the CPU time of multigrid simulations is dominated by the communication overhead resulting in a low parallel efficiency. Consequently, a higher number of computational work is done on a single grid than predicted by the CPU Time ratio.

Table 4.2: MG performance for different Reynolds numbers
(Number of processors = 4)

	Re = 100		Re = 400		Re = 1,000	
Grid Size	CPU Time SG/MG	WU SG/MG	CPU Time SG/MG	WU SG/MG	CPU Time SG/MG	WU SG/MG
128 × 128	13.9	75.2	11.41	49.54	4.5	13.71
256 × 256	89.3	283.66	64.9	190.6	19.95	45.92
512 × 512	404.1	1040.11	307.8	643.75	110.99	264.77
1024 × 1024	1371.6	2940.7	1182.7	2297.92	509.04	1100.93

Table 4.3: Percentage of communication time for different Reynolds numbers
(Number of processors = 4)

	Re = 100		Re = 400		Re = 1,000	
Grid Size	%Comm Time (SG)	%Comm Time (MG)	%Comm Time (SG)	%Comm Time (MG)	%Comm Time (SG)	%Comm Time (MG)
128 × 128	15.83	67.80	10.68	79.13	10.44	58.31
256 × 256	3.82	51.54	3.58	41.11	3.88	35.28
512 × 512	1.93	21.23	2.08	22.62	2.11	20.25
1024 × 1024	1.39	7.74	1.25	6.18	1.51	9.50

4.4.2 Convergence Rate and Convergence Factor

Figures 4.4-4.6 demonstrates the convergence of residuals as a function of WU for single grid and multigrid simulations with Re = 400. A steep decrease of multigrid residuals are observed from these graphs, whereas the single grid exhibits very slow convergence. To quantify the convergence rate, we can introduce a convergence factor which is roughly the maximum factor by which the error is reduced by each work unit [70]. In other words, the lower the convergence factor, the greater the convergence rate. Since in practice the exact solution is not known, the error cannot be computed during the iterations. Thus, we define a convergence factor Ω based on the residuals which indicates the number of iterations required to reduce the residual by a factor of $10^{-\zeta}$. Let K be the smallest integer that satisfies -

$$\frac{\|R^{(K)}\|}{\|R^{(0)}\|} \leq 10^{-\zeta} \tag{4.30}$$

The condition is approximately satisfied if -

$$\Omega^{K} \leq 10^{-\zeta} \tag{4.31}$$

Thus, we can approximate Ω from the following equation:

$$-log_{10}(\Omega) \leq \frac{\zeta}{K} \tag{4.32}$$

Figure 4.7 shows the asymptotic value of the convergence factors as a function of the number of grid points. For relatively low Reynolds number cases (Re = 100-1,000), the convergence factor is lower and it decreases with the increase of grid points resulting in a fast convergence rate. But, for a higher Reynolds number case (Re = 3,200), the convergence factor remains very close to 0.98 indicating a degradation of FMG performance. The reason is, the prolongation of converged coarse grid values to the next finer grid may not be very accurate due to the effect of large convection at a higher Reynolds number. Thus, although in theory we are expecting a “good” initial guess for the next finer level, in practice this may not be achievable at a higher

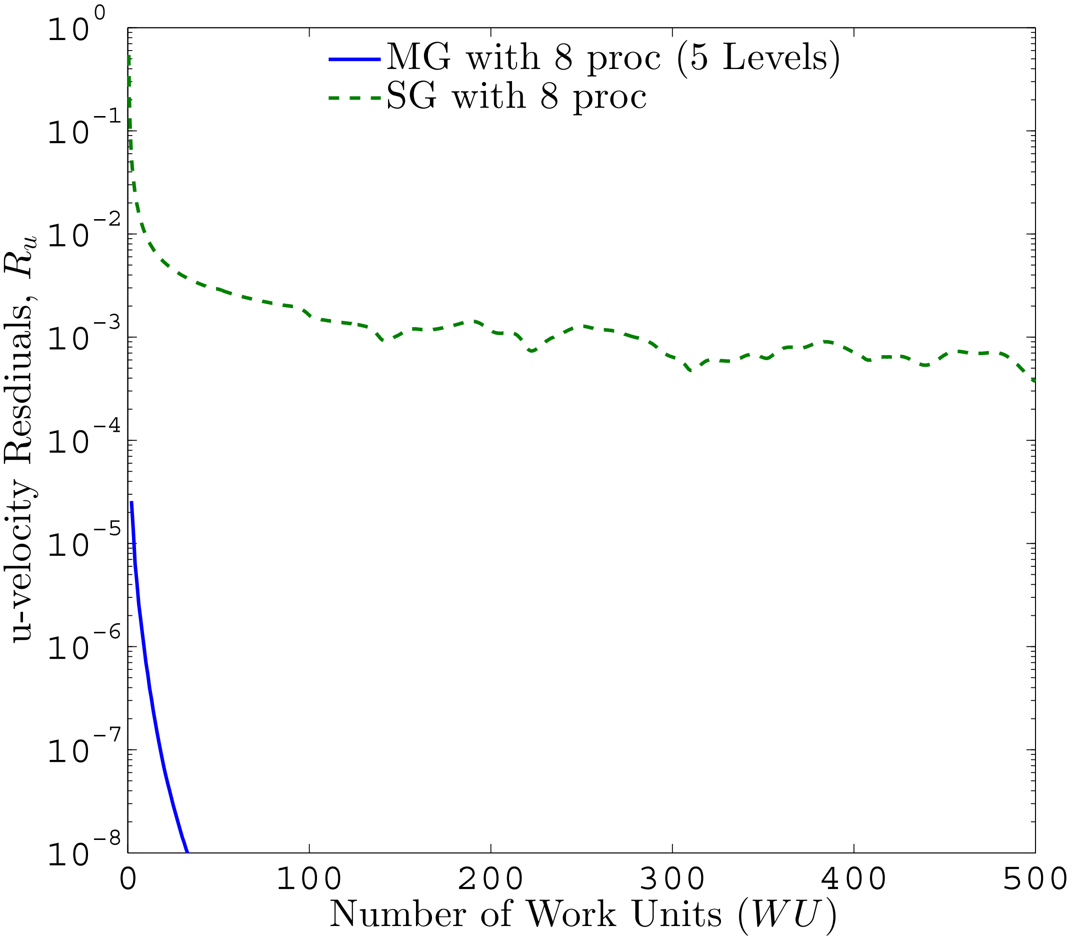

Figure 4.4: u-velocity residuals on a 512 × 512 CV grid as a function of Work Units (WU) for Re = 400

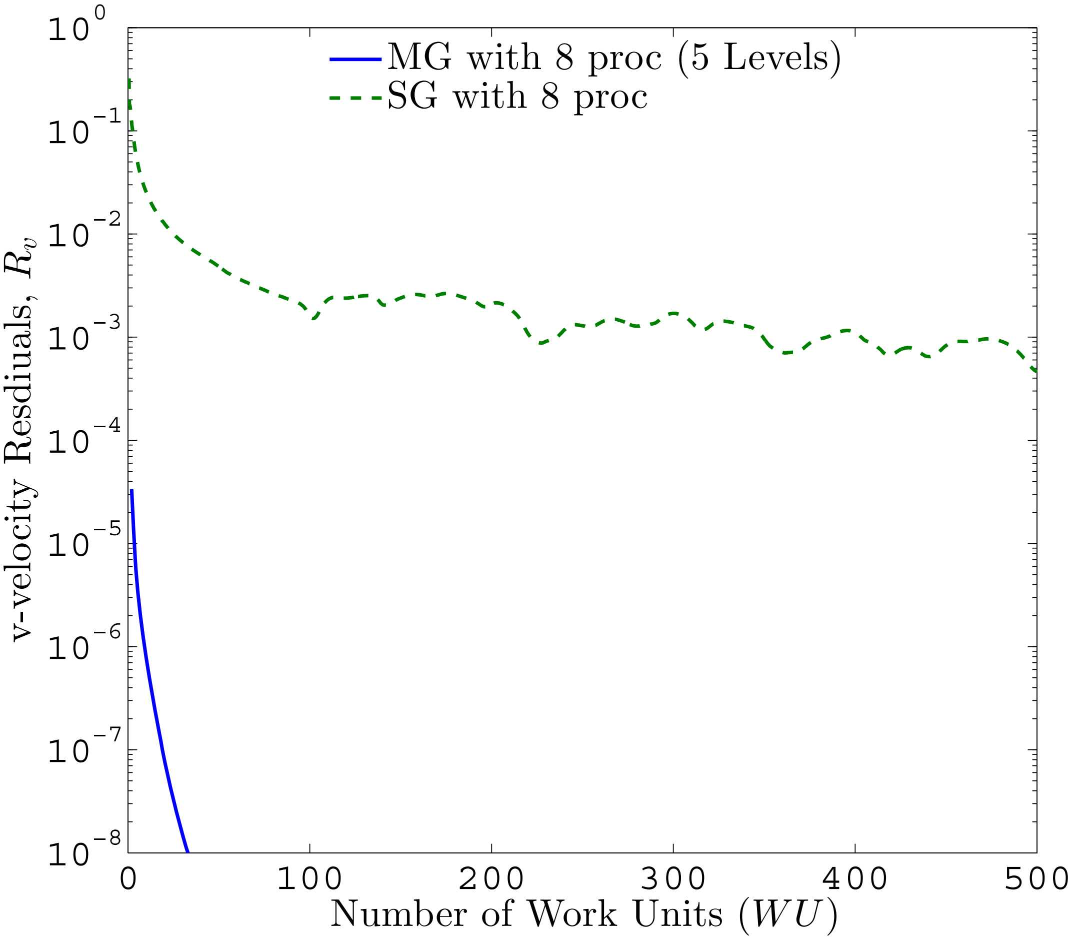

Figure 4.5: v-velocity residuals on a 512×512 CV grid as a function of Work Units (WU) for Re = 400

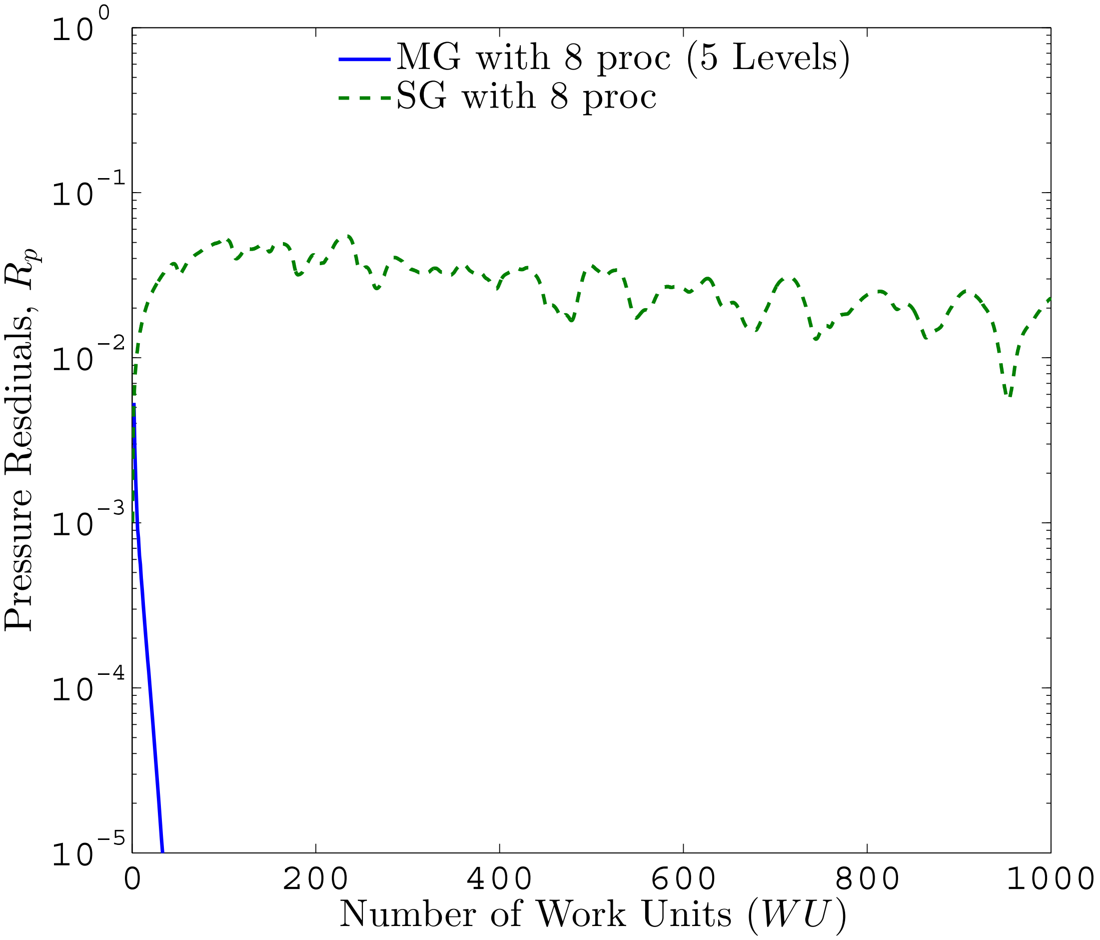

Figure 4.6: Pressure residuals on a 512×512 CV grid as a function of Work Units (WU) for Re = 400

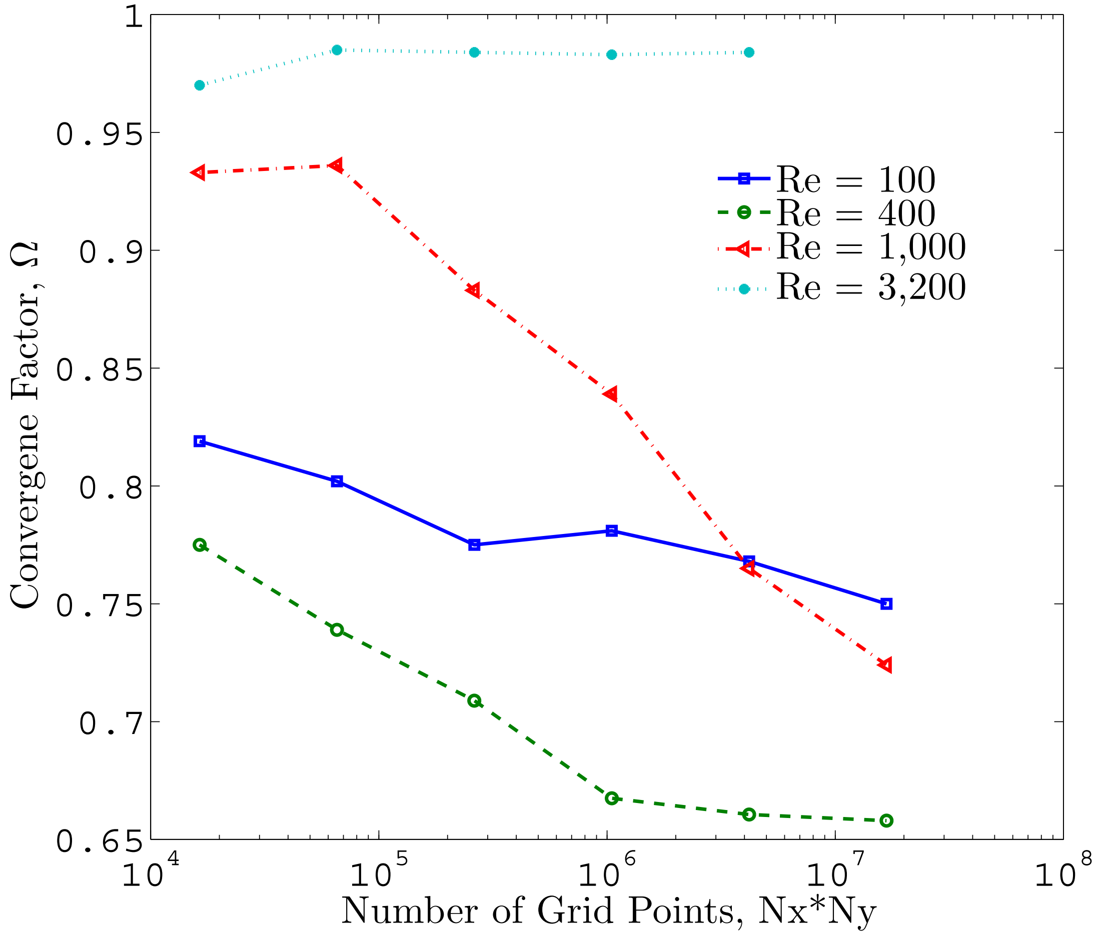

Figure 4.7: Asymptotic value of convergence factor for different Reynolds number (Number of processors= 4)

Reynolds number. For the same reason, degradation of multigrid performance has been observed for turbulent flows. This observation is in complete accordance with the previous work of Lien and Leschziner [54] and Muzaferija [77].

4.4.3 Computational Complexity

In order to compare the computational work between single grid (SG) and multigrid (MG) methods, we plotted the CPU Time against the number of grid points in Figure 4.8. For single grid simulations with eight processors, the CPU Time increases almost quadratically ($O(N^2)$), as expected. On the other hand, for multigrid simulations, the increase in CPU Time follows an $O(N)$ trend for both four and eight processors. The slight deviation of the curves from their ideal behavior may be attributed to the communication overhead due to the use of parallel machines.

Figure 4.9 demonstrates the effect of Reynolds number on the computational complexity. Although the CPU Time increases with the increase of Reynolds number, the increase of computational work follows an $O(N)$ trend for a fixed Reynolds number. The variation of trend for Re = 3,200 at lower grid sizes is again due to the very high communication overhead (74% and 45% respectively) which occurs during a large number of coarse grid iterations.

4.4.4 Benchmark Results for Lid Driven Cavity Flow

One of the objectives of multigrid simulations is to conduct simulations in very fine grids and produce high fidelity results. This is due to the fact that several orders of magnitude of speedup in CPU Time can be achieved with the multigrid method as compared to the single grid method. In this study, lid driven cavity flow simulations were performed using a grid of 1024 × 1024 CVs. Figures 4.10 – 4.14 present the centerline u-velocity and v-velocity profiles along y and x directions, respectively for Reynolds numbers ranging from 400 to 7,500. The results are compared with

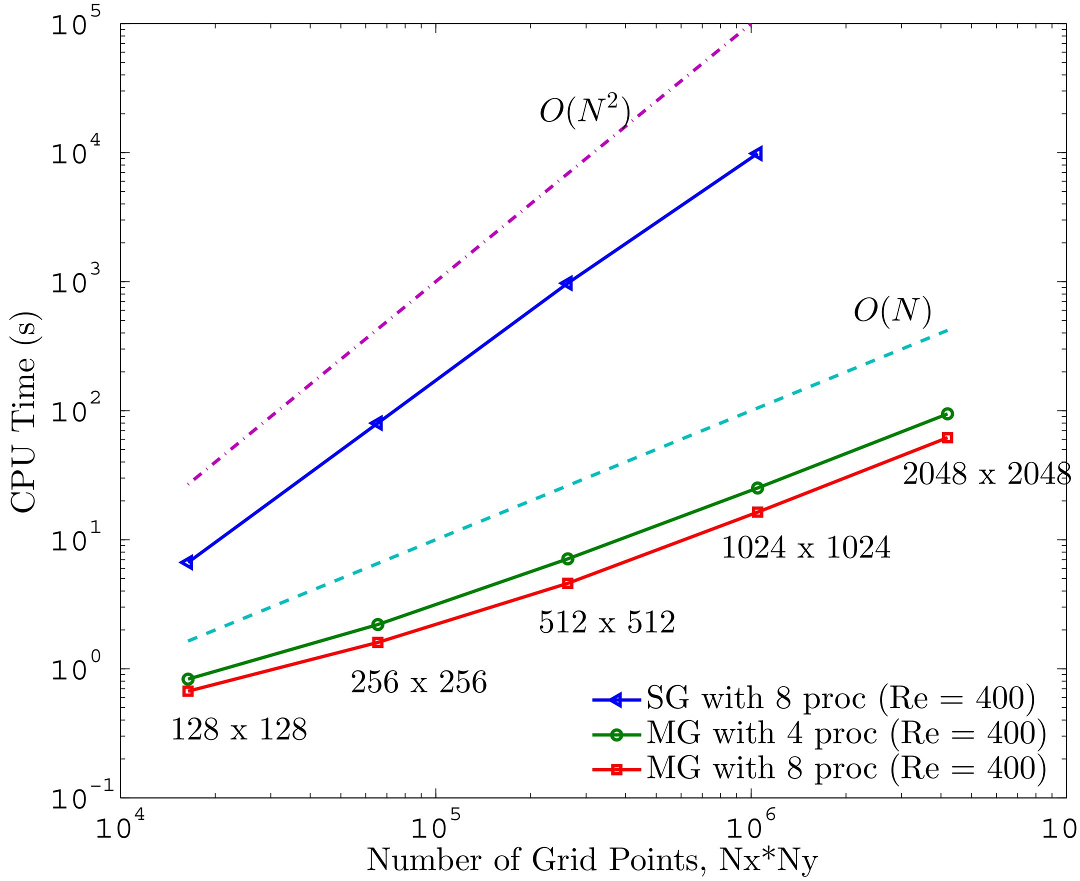

Figure 4.8: Comparison of parallel MG performance with SG for Re = 400. The dashed line has a slope 1 indicating MG efficiency. The dashed-dotted line has a slope 2 indicating SG efficiency.

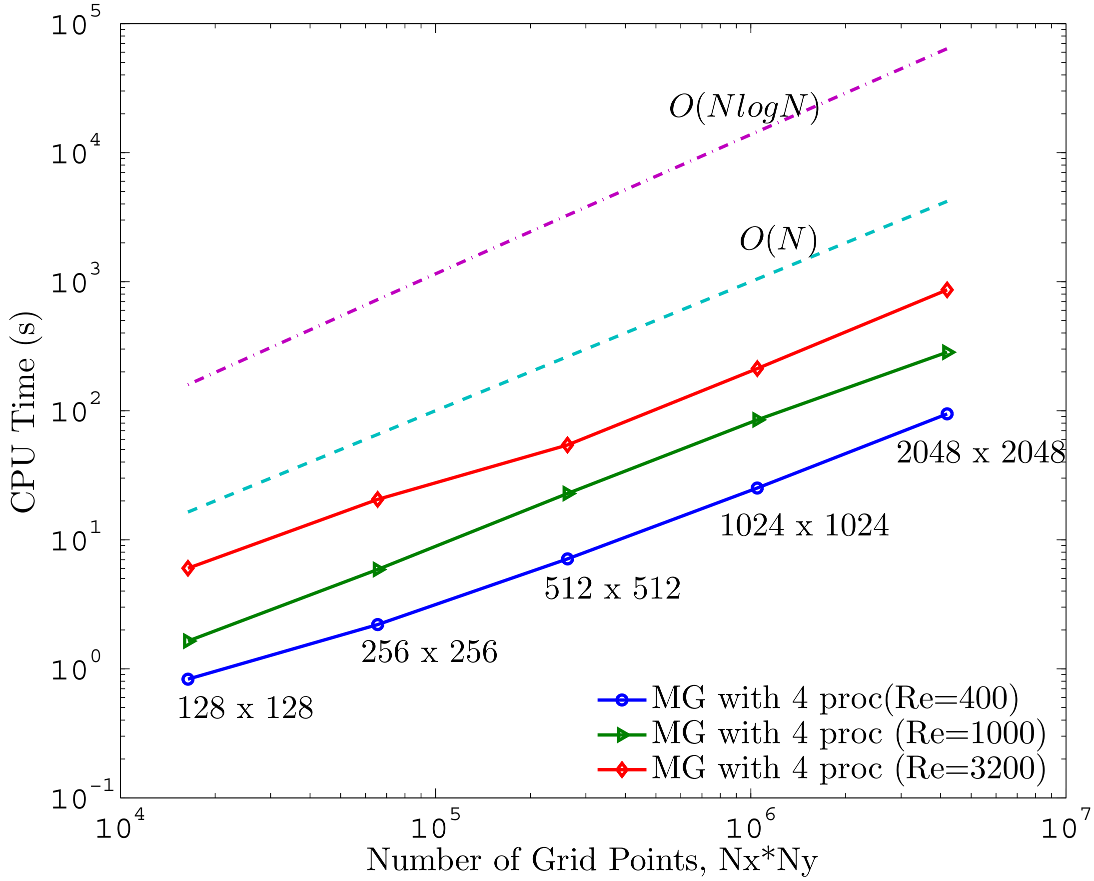

Figure 4.9: Effect of Reynolds number on parallel MG performance

Ghia et al. [75] and Erturk et al. [76]. Very good agreement can be observed for low Reynolds number case Re = 400. For Re = 1,000 and 3,200, small deviations from Ghia et al. [75] near the peak values of the velocity profiles can be identified. As the Reynolds number increases further, these deviations become more prominent. It should be noted that, the numerical scheme used by Ghia et al. is spatially second order accurate and the benchmark results were presented for 256×256 grid. Thus, it is quite possible that at high Reynolds numbers, the results may not be very accurate. Erturk et al. [76] also used a second order accurate spatial discretization scheme, but they presented the benchmark results for a relatively fine grid of 601×601. The velocity profiles from present simulations match very well with the results of Erturk et al. [76] for Re = 1,000 and 5,000. For Re = 7,500, slight differences near the peak regions are seen. It has been tested in the present study (not shown though) that 1024×1024 CVs form a suitable grid to sufficiently capture the large gradients at high Reynolds numbers. Tables 4.4 and 4.5 tabulates the velocity profiles along the vertical and horizontal centerlines of the cavity at different Reynolds number. Since a second order accurate central difference scheme (CDS) has been applied to generate the simulation results, they can be used as benchmark values for future code validation.

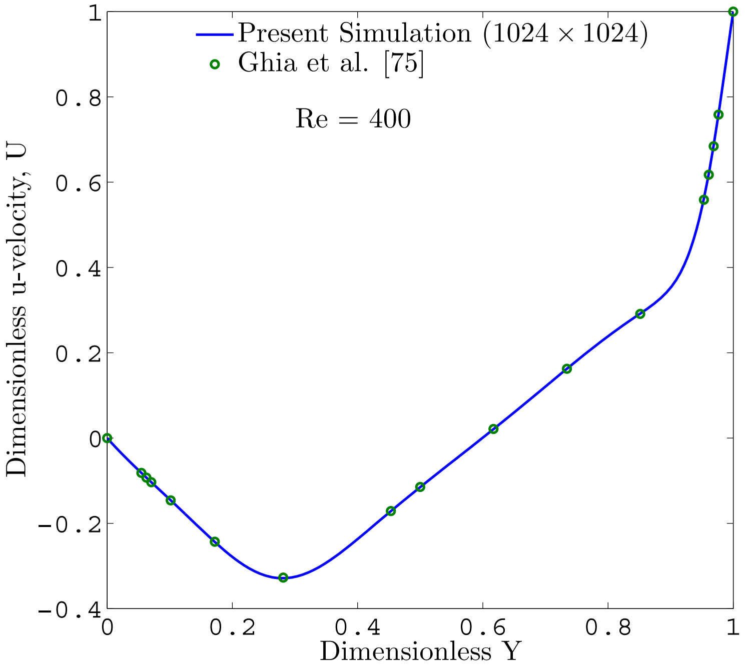

(a) u-velocity for Re = 400

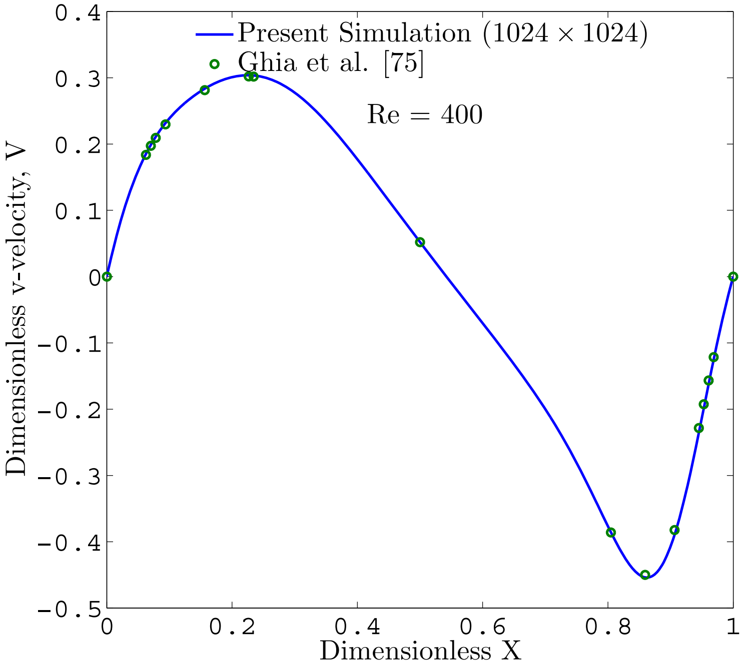

(b) v-velocity for Re = 400

Figure 4.10: Centerline velocity profiles for Re = 400

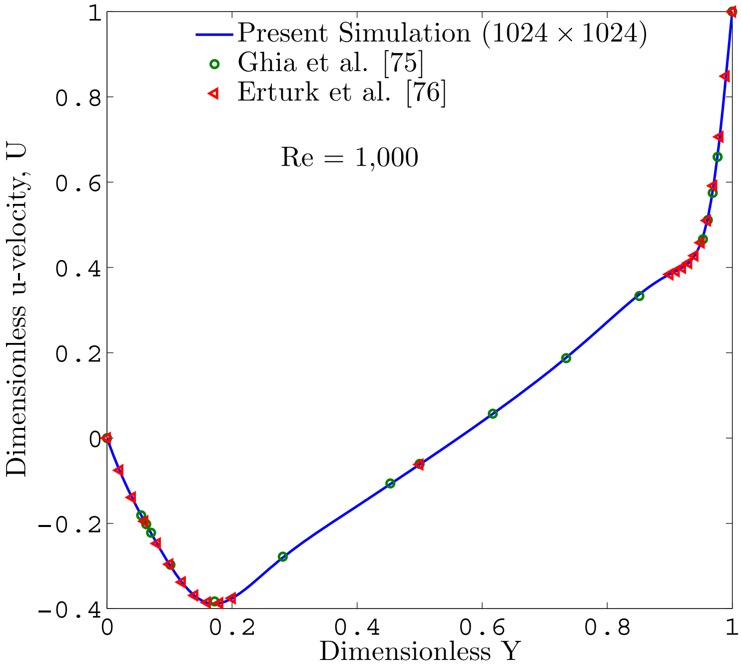

(a) u-velocity for Re = 1,000

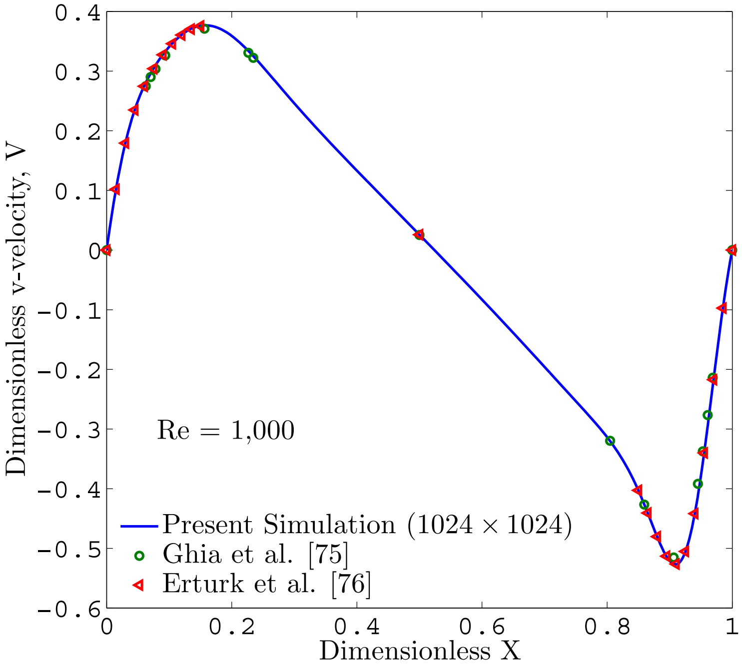

(b) v-velocity for Re = 1,000

Figure 4.11: Centerline velocity profiles for Re = 1,000

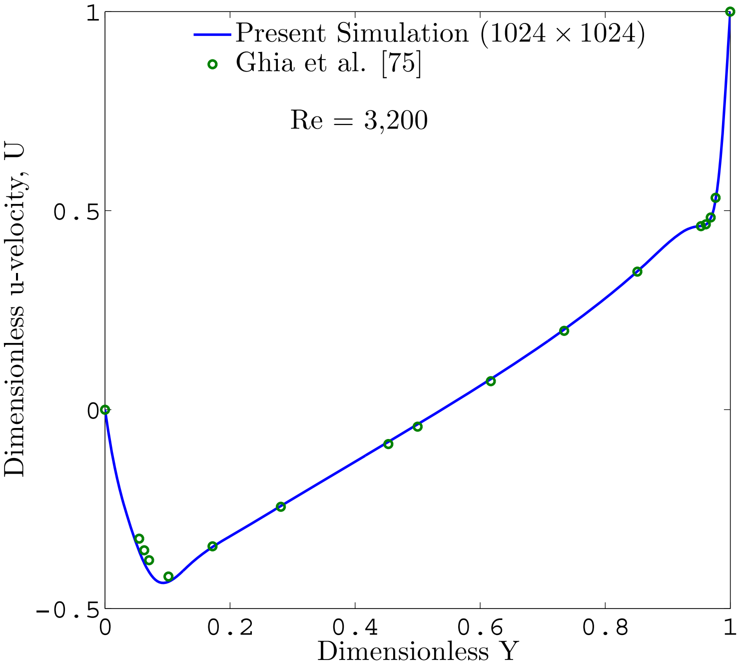

(a) u-velocity for Re = 3,200

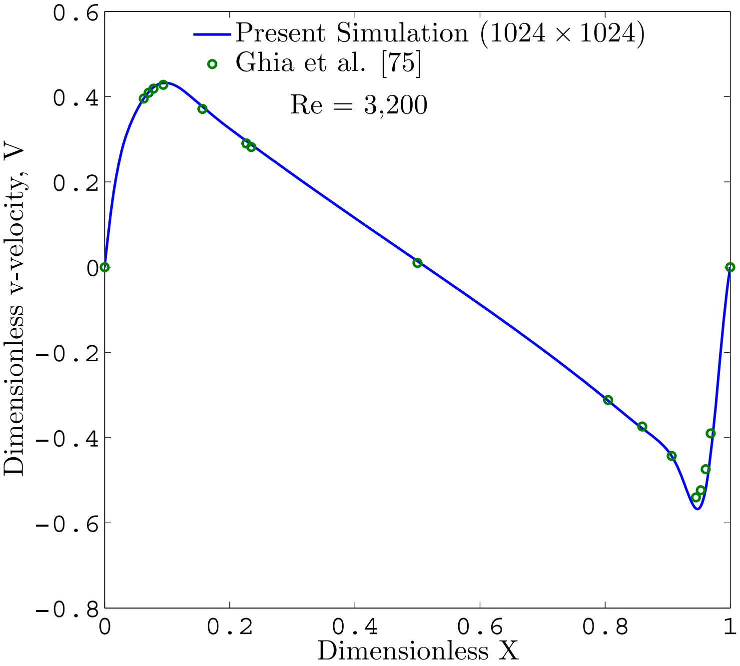

(b) v-velocity for Re = 3,200

Figure 4.12: Centerline velocity profiles for Re = 3,200

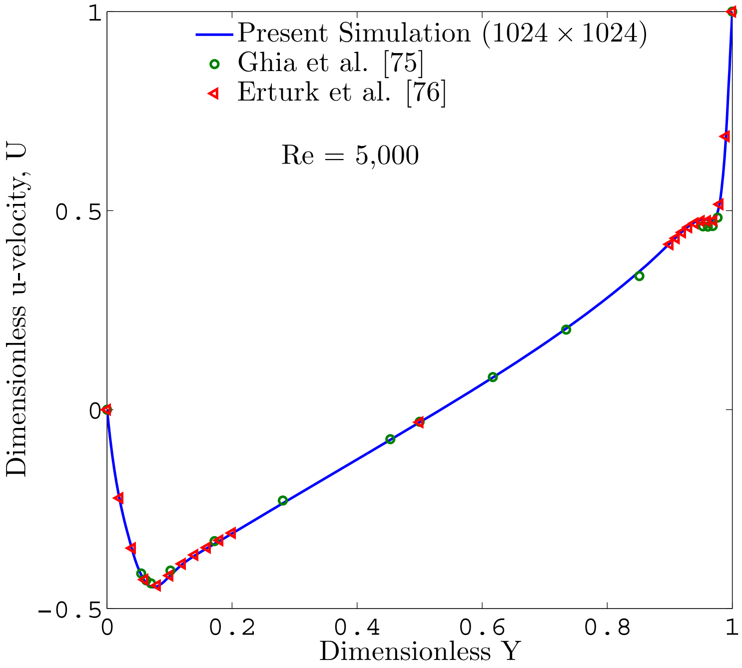

(a) u-velocity for Re = 5,000

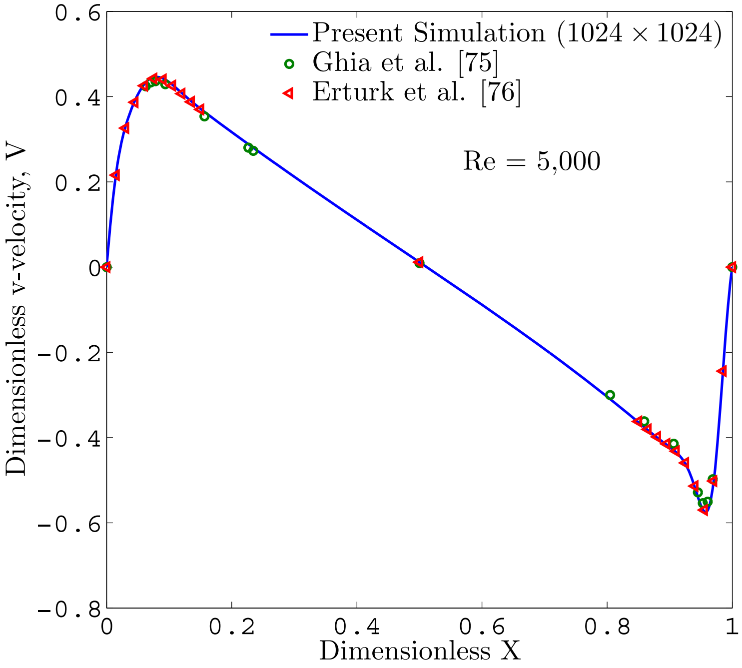

(b) v-velocity for Re = 5,000

Figure 4.13: Centerline velocity profiles for Re = 5,000

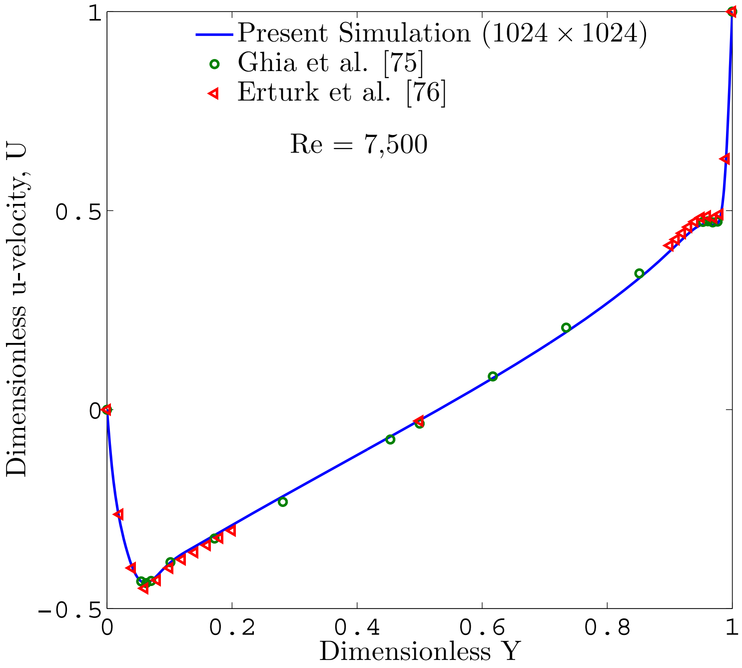

(a) u-velocity for Re = 7,500

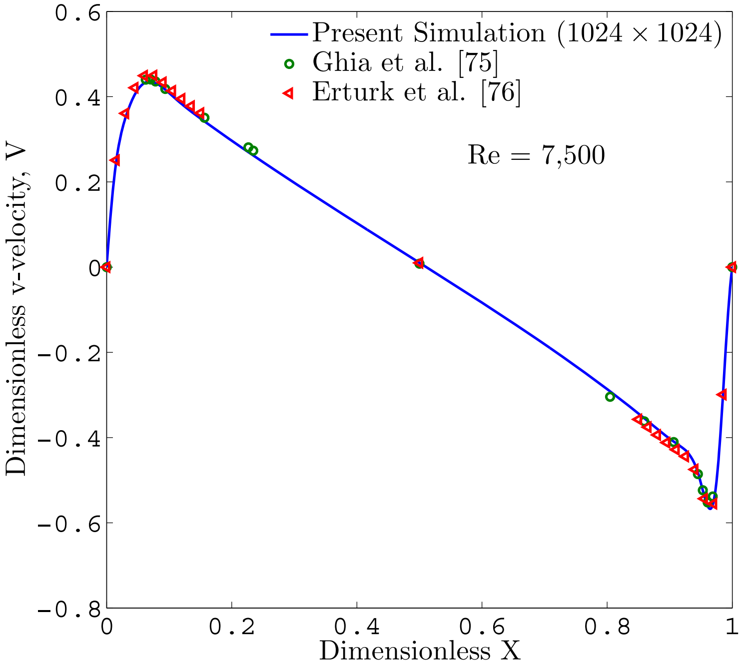

(b) v-velocity for Re = 7,500

Figure 4.14: Centerline velocity profiles for Re = 7,500

Table 4.4: Non-dimensional u-velocity along the y-centerline for different Reynolds numbers. The top plate is moving with a uniform velocity. No slip boundary conditions were used at the walls. The grid size is 1024 × 1024 CVs.

Y	Re = 400	Re = 1,000	Re = 3,200	Re = 5,000	Re = 7,500
0.0000	0.00000	0.00000	0.00000	0.00000	0.00000
0.0200	-0.03177	-0.07603	-0.17777	-0.22495	-0.27754
0.0405	-0.06189	-0.14120	-0.29262	-0.35426	-0.39631
0.0601	-0.08923	-0.19577	-0.37658	-0.43066	-0.43509
0.0806	-0.11732	-0.24927	-0.42746	-0.44392	-0.41603
0.1001	-0.14410	-0.29689	-0.43339	-0.41856	-0.38573
0.1206	-0.17257	-0.33989	-0.41101	-0.38853	-0.36219
0.1401	-0.19996	-0.36975	-0.38285	-0.36682	-0.34424
0.1606	-0.22849	-0.38617	-0.35711	-0.34766	-0.32580
0.1802	-0.25458	-0.38717	-0.33688	-0.32978	-0.30805
0.2007	-0.27956	-0.37527	-0.31763	-0.31067	-0.28948
0.5005	-0.11446	-0.06151	-0.03633	-0.03149	-0.02628
0.9009	0.35427	0.38479	0.41898	0.41901	0.39897
0.9106	0.37502	0.39215	0.43189	0.43391	0.41373
0.9204	0.40187	0.40008	0.44321	0.44822	0.42854
0.9302	0.43679	0.41073	0.45216	0.46100	0.44270
0.9409	0.48695	0.43021	0.45838	0.47176	0.45607
0.9507	0.54512	0.46149	0.46082	0.47691	0.46438
0.9604	0.61626	0.51371	0.46447	0.47686	0.46695
0.9702	0.70001	0.59432	0.48617	0.47842	0.46387
0.9800	0.79419	0.70664	0.56396	0.51934	0.47856
0.9907	0.90472	0.85977	0.76162	0.70875	0.64723
1.000	1.00000	1.00000	1.00000	1.00000	1.00000

Table 4.5: Non-dimensional v-velocity along the x-centerline for different Reynolds numbers. The top plate is moving with a uniform velocity. No slip boundary conditions were used at the walls. The grid size is 1024 × 1024 CVs.

X	Re = 400	Re = 1,000	Re = 3,200	Re = 5,000	Re = 7,500
0.0000	0.00000	0.00000	0.00000	0.00000	0.00000
0.0151	0.05951	0.10292	0.18196	0.21956	0.24578
0.0308	0.11028	0.18283	0.29182	0.33292	0.35341
0.0454	0.14906	0.23661	0.34983	0.39131	0.40595
0.0600	0.18047	0.27521	0.39019	0.42905	0.431754
0.0747	0.20578	0.30403	0.41760	0.44543	0.43417
0.0903	0.22746	0.32819	0.43135	0.44258	0.42059
0.1049	0.24397	0.34645	0.43078	0.42821	0.40201
0.1206	0.25854	0.36149	0.41957	0.40821	0.38208
0.1352	0.27001	0.37111	0.40330	0.38937	0.36494
0.1450	0.27667	0.37494	0.39111	0.37749	0.35419
0.5005	0.05146	0.02526	0.01373	0.01119	0.00988
0.8501	-0.44994	-0.40326	-0.36762	-0.36416	-0.34357
0.8647	-0.45381	-0.44028	-0.38430	-0.38208	-0.36106
0.8804	-0.44362	-0.48158	-0.40198	-0.40059	-0.37991
0.8950	-0.41888	-0.51369	-0.42160	-0.41680	-0.39706
0.9106	-0.37613	-0.52674	-0.45415	-0.43483	-0.41371
0.9253	-0.32251	-0.50508	-0.50317	-0.46228	-0.42972
0.9399	-0.25931	-0.44280	-0.55640	-0.51565	-0.46188
0.9546	-0.19118	-0.34384	-0.55560	-0.57221	-0.532543
0.9702	-0.11873	-0.21597	-0.42028	-0.50375	-0.54975
0.9849	-0.05590	-0.09848	-0.19571	-0.24939	-0.30553
1.000	0.00000	0.00000	0.00000	0.00000	0.00000

4.5 Conclusions

A parallel multigrid finite volume solver was developed for simulating two-dimensional incompressible Navier-Stokes equations. In the multigrid framework, the maximum number of processors is limited by the coarse grid size. The parallel multigrid code showed superior convergence over the single grid counterpart. Multigrid speedup as high as 1370 was achieved for the finest grid size (1024×1024). The ratio of work units between single grid and multigrid is not close to the ratio of CPU time. This is due to the large communication overhead occurring at the coarsest grid level during the multigrid iterations. It has been shown that the computational effort on a multigrid increases proportionally to the number of grid points. Thus, the 'golden rule' of the multigrid method, as proposed by Brandt [52], has been validated for a range of Reynolds numbers. The convergence factors for different Reynolds numbers were analyzed and a favorable convergence rate has been shown for low Reynolds number flows. Using the parallel multigrid solver, very high fidelity solution for lid driven cavity flow has been documented, which can be used for future benchmarking purposes.

5. STEADY FLOW IN ROTATING MICROCHANNELS*

5.1 Introduction

In this chapter we will analyze the steady flow inside an array of radially rotating microchannels by introducing a model problem. In particular, we want to accomplish the following tasks:

(i) By varying the rotational speed, hydraulic diameter, and aspect ratio we want to demonstrate how the rotational Reynolds number is affected by these parameters, which in turn affect the extent of secondary flow.

(ii) By comparing the root mean square (RMS) deviation of the axial velocity profiles with the approximate analytical results of purely centrifugal flow for different aspect ratios, we want to identify the critical values of the flow parameters in order to demarcate the secondary flow dominant regions.

5.2 Model Problem

In most of the centrifugal microfluidic devices, the fluid is placed in a microchamber connected to an array of microchannels. Figure 5.1a depicts a simplified diagram of an array of rectangular microchannels aligned radially on a circular disk. As the disk is rotated around an axis perpendicular to the plane of the disk, the liquid advances through the microchannels along the radially outward direction due to the induced centrifugal force f_ω. This is analogous to a pressure driven flow in a microchannel where the driving force of the liquid is pressure difference between the

---

*Part of this chapter is reprinted with permission from P. Roy, N. K. Anand, and D. Banerjee. Numerical simulation of fluid flow and heat transfer in radially rotating microchannels. *Microfluidics and Nanofluidics*, 15(3):397-413,2013. Copyright 2013 by Springer.

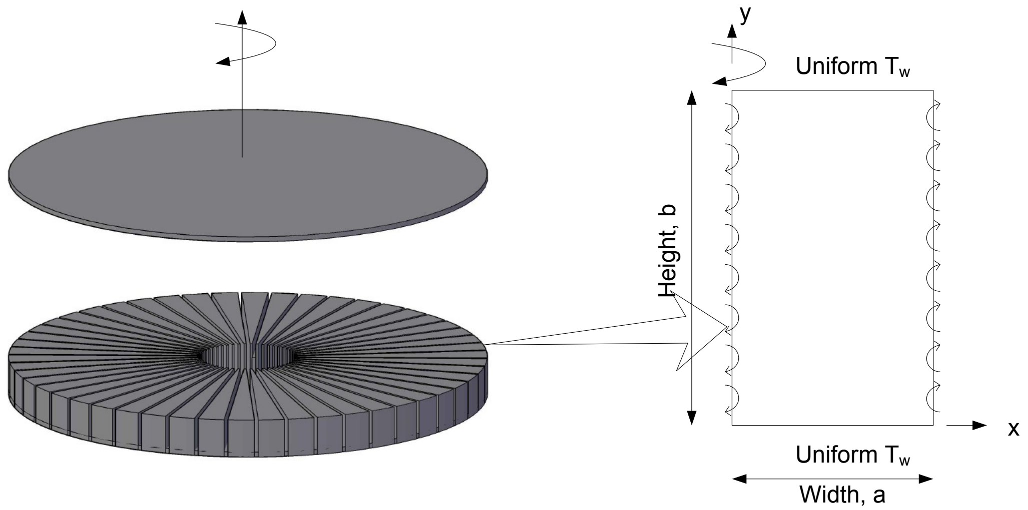

(a) Three dimensional microchannel array (left) and cross-sectional area of a single microchannel (right)

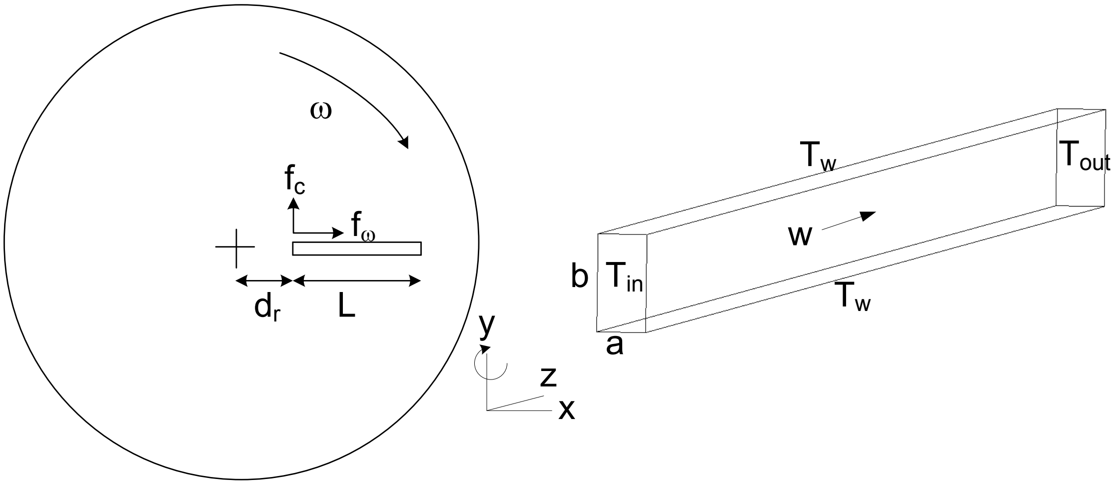

(b) Schematic of the rotating disk (left) and computational domain of a single microchannel (right)

Figure 5.1: Schematic diagram of the simplified model problem

inlet and outlet of the channel instead of the centrifugal force. At this stage, the velocity of the liquid and the shape of the liquid meniscus are primarily governed by the centrifugal force and the surface tension force. Once the microchannel is filled up with the liquid, a continuous flow of liquid is established along the microchannel and the surface tension effect can be neglected. The rotation induces another force, which acts in the perpendicular direction to the centrifugal force on the disk plane, and is known as the Coriolis force f_c. As can be seen later, this Coriolis force (f_c) is responsible for generating secondary flow phenomena in rotating microchannel flow.

The model problem can be simplified by taking the advantage of the repetitive nature of the microchannel array and considering the fact that the angle between two successive microchannels is very small. A single microchannel can be used as a solution domain with repeated thermal boundary conditions at the side walls [78]. Since the wall thickness is very small, the wall conduction effect can be neglected. The schematic diagram of the solution domain and the corresponding coordinate system and boundary conditions are depicted in Figure 5.1b. The inlet of the microchannel is located at a radial distance d_r from the disk center and the rotating frequency of the disk is ω. The three-dimensional rectangular microchannel has a width a, height b, and length L. The aspect ratio (α) of the channel is defined by the ratio of the width to height i.e. $\alpha = a/b$. Water ($Pr = 7.0$) was considered as the test fluid. Table 5.1 shows the independent parameters used for the simulations performed in this study.

Table 5.1: Geometrical and rotational parameters

Channel Width a (μm)	Channel Height b (μm)	Channel Length L (mm)	Hydraulic Diameter D_h(μm)	Aspect Ratio α	Rotational Speed (RPM)	Reynolds Number (Re)
180	57	10	86.58	3.16	57 - 2,847	50-400
110	1,000	20	200.0	0.11	400-4,200	8-896
125	500	20	200.0	0.25	400-4,200	9-1,056
150	300	20	200.0	0.50	400-4,200	11 -1,239
200	200	20	200.0	1.00	400-4,200	12 -1,354
300	150	20	200.0	2.00	400-4,200	11 - 1,239
500	125	20	200.0	4.00	400-4,200	9-1,056
1,000	110	20	200.0	9.09	400-4,200	9-1,056

5.2.1 Governing Equations

The liquid flow in the microchannel was assumed to be steady, laminar and incompressible with constant thermo-physical properties. Conduction effects inside the channel walls were assumed to be negligibly small. Effects of buoyancy forces and viscous dissipation were neglected. Under these assumptions, the conservation of mass, momentum and energy equations can be written in the following Cartesian tensor form:

Continuity:

$$\frac{\partial u_i}{\partial x_i} = 0 \tag{5.1}$$

$$Momentum: \qquad \rho u_i \frac{\partial u_j}{\partial x_i} = -\frac{\partial p}{\partial x_j} + \mu \frac{\partial^2 u_j}{\partial x_i \partial x_i} + \rho S_j \tag{5.2}$$

$$Energy: \qquad \rho C_p u_i \frac{\partial T}{\partial x_i} = -k \frac{\partial^2 T}{\partial x_i \partial x_i} \tag{5.3}$$

The source terms in the momentum equations for an orthogonal rotation mode can be expressed as [79]:

$$S_1 = -2\omega w + \omega^2 x \tag{5.4a}$$

$$S_2 = 0 \tag{5.4b}$$

$$S_3 = 2\omega u + \omega^2 (d_r + z) \tag{5.4c}$$

From the expressions of the source terms, it can be seen that the centrifugal and the Coriolis forces appear in only x and z-directions. Further inspection reveals that, as the primary flow direction is in the z-direction and the microchannel is rotating clockwise around the y-axis, the centrifugal force acts in the z-direction ($f_{\omega,z} = \omega^2(d_r + z)$) and the Coriolis force acts in the x-direction ($f_{c,x} = -2\omega w$). However, a portion of the centrifugal force acts in the x-direction ($f_{\omega,x} = \omega^2 x$) and similarly a portion of the Coriolis force acts in the z-direction ($f_{c,z} = 2\omega u$). These forces appear as a result of expressing the governing equations in an Eulerian frame, fixed to the rotating microchannel. Since the width of the microchannel (in x-direction) and the secondary velocity (u) are very small, the values of $f_{\omega,x}$ and $f_{c,z}$ are negligible. Thus, any future reference to the centrifugal force will mean the centrifugal force is acting in z-direction, i.e. $f_\omega = f_{\omega,z}$. Similarly, reference to the Coriolis force will mean the Coriolis force is acting in the x-direction, i.e. $f_c = f_{c,x}$.

5.2.2 An Approximate Analytical Solution

For low rotational Reynolds numbers ($Re_\omega \sim O(1)$), the Coriolis force (f_c) is very small and hence can be neglected. Furthermore, the centrifugal force term (f_ω) can be included in the pressure gradient term to produce a modified pressure gradient in the z-momentum equation. If a steady laminar fully developed flow with negligible Coriolis force is assumed, the flow can be considered as a purely centrifugal flow. As a result, the z-velocity (w) becomes a function of x and y only and the z-momentum equation simplifies to the following Poisson equation:

$$\frac{\partial^2 w}{\partial x^2} + \frac{\partial^2 w}{\partial y^2} = \frac{1}{\mu}\frac{\partial p^*}{\partial z} \tag{5.5}$$

where p^* is the modified pressure defined by:

$$p^* = p - \rho\omega^2 \left(d_r z + \frac{z^2}{2} \right) \tag{5.6}$$

The corresponding boundary conditions at the walls are:

$$w(0, y) = w(a, y) = 0 \tag{5.7}$$

$$w(x, 0) = w(x, b) = 0 \tag{5.8}$$

As there is no Coriolis force term in Equation 5.5, the velocity profile $w(x, y)$ is perfectly symmetric about the centerlines $x = a/2$ and $y = b/2$ at any cross-section of the microchannel. Equation 5.5 can be solved with the given boundary conditions to yield the following analytical solution:

$$w(x,y) = \frac{16}{\pi^2 \mu}\left(-\frac{dp}{dz} + f_\omega\right)\sum_{m=1}^{\infty}\sum_{n=1}^{\infty}\frac{1}{(2m-1)(2n-1)\Theta_{m,n}} sin\left(\frac{\xi_m y}{a}\right) sin\left(\frac{\xi_n y}{b}\right) \tag{5.9}$$

where

$$f_\omega = \rho\omega^2\left(d_r + z\right) \tag{5.10a}$$

$$\Theta_{m,n} = \frac{\xi_m^2}{a^2} + \frac{\xi_n^2}{b^2} \tag{5.10b}$$

$$\xi_m = (2m-1)\pi,\ \xi_n = (2n-1)\pi \tag{5.10c}$$

The above solution given in Equation 5.9 is slightly different from that of Liu et al. [80] and Chakraborty et al. [81] due to the shifting of the coordinates. The average velocity can be derived by taking an area weighted average of the axial velocity distribution:

$$\begin{aligned} w_{avg} &= \frac{1}{ab}\int_0^a \int_0^b w(x,y)dxdy && (5.11a) \\ &= \frac{64}{\pi^4 \mu}\left(-\frac{dp}{dz} + f_\omega\right)\sum_{m=1}^{\infty}\sum_{n=1}^{\infty}\frac{1}{(2m-1)^2(2n-1)^2\Theta_{m,n}} && (5.11b) \end{aligned}$$

The above analytical results will be useful for verifying the numerical results in the fully developed region when the Coriolis effect is negligible. From Eqs. 5.9 and 5.11b, it can be observed that for purely centrifugal flow, the ratio of the axial velocity to the average velocity is independent of the pressure gradient. Thus, a comparison of w/w_{avg} between the simulation results and the analytical results for a purely centrifugal flow can reveal whether the flow is centrifugal flow dominated or the Coriolis force dominated.

5.3 Numerical Solution Method

A finite volume technique described in Chapter 2 was used to discretize the governing equations. Solution to the one-dimensional convection-diffusion equation was represented by the power-law scheme. Velocity and pressure variables were calculated at staggered locations and they were linked by the SIMPLE algorithm [37]. A line-by-line tri-diagonal matrix algorithm (TDMA) was applied to solve the discretized equations in each plane of y and z directions. A cyclic tri-diagonal matrix algorithm (CTDMA) was applied to solve the repeated thermal boundary condition in the cross-stream (x) direction [82]. The convergence of the iterative procedure was declared when the residuals reached arbitrarily small epsilon values ($\sim 1\times10^{-6}$). The solution of energy equation was decoupled from the solution of momentum equations i.e. the temperature field was calculated once the converged solution for velocity and pressure fields were obtained. The serial solver was developed in FORTRAN 90 and a typical simulation took two to five hours on the Texas A&M University Eos supercomputer, which consists of 3168 cores (each 2.8 GHz) with a total memory of 9056 GB and a peak performance of 35.5 TFlops.

5.3.1 Treatment of the Source Terms

The presence of source terms in the discretized momentum equations reduces the diagonal dominance of the solution matrix, resulting in a decrease of the numerical stability of the scheme. Hence, special treatment was needed to get a stable converged numerical solution of the rotating microchannel flow. At the beginning of simulation, a very small rotating frequency was given. As the iteration of the pressure based solver progressed, the rotating frequency was also ramped up by a constant factor with each iteration. Eventually, the desired value of the rotational frequency was reached after a number of iterations. In this way, the numerical stability of the code was confirmed and high rotational speed could be achieved using the above numerical scheme.

5.4 Grid Independence and Code Validation

A uniform grid was considered in the x, y and z directions. As the exact analytical solution to the governing equations is not known, a grid independence test was performed by increasing the grid size until the relative difference between the results for two successive grids is negligible. Table 5.2 demonstrates the results from the grid independence study for a square microchannel rotating at 3000 RPM with a Reynolds number of 691. The top and bottom wall was maintained at a constant temperature whereas a thermally repeated boundary condition was applied in the cross stream direction. From Table 5.2, it can be seen that the percentage differences among the results (w_{max}/w_{in} and Nu_{avg}) for $35 \times 35 \times 90$, $41 \times 41 \times 100$ and $43 \times 43 \times 120$ meshes are very small. Considering the computational efficiency, the grid size $41 \times 41 \times 100$ was declared as grid independent and this grid size was used for all other subsequent simulations in this chapter. For larger aspect ratios, this grid size was scaled accordingly to ensure the grid independent result. In order to ensure its dependability, the code was tested against benchmark problems and the results were reproduced to certain accuracy. For the non-rotating case, the simulation results of a fully developed steady laminar flow through a square duct with uniform wall temperature boundary conditions were compared with Shah and London [83], which are presented in Table 5.3. Another validation of the code was performed by comparing the apparent friction coefficient values with the experimental results of single-phase forced convective flow of water in an array of parallel microchannels etched on a silicon substrate by Kawano et al. [84]. The comparison shown in Figure 5.2 shows that the numerical results are in good agreement between Re = 80 to Re

= 250. For $Re > 250$, the deviation between experimental and simulation results are high. However, in the original work, Kawano et al. [84] reported that for $Re > 200$, the experimental results may be affected by the external disturbances. Thus, the present simulation results can be considered satisfactory considering the experimental uncertainty. These results also closely match with the numerical results of Mlcak et al. [78] for identical geometry and boundary conditions. To validate the rotating channel case, the code was compared against the steady laminar forced convection in rotating square duct solutions by Hsieh et al. [85]. Figure 5.3 presents the fully developed axial velocity profiles along the x axis at $y/H = 1/2$ for $Re = 300$ and $Ro = 0.0167, 0.333$, and 1.667. The results of the present simulation are in good agreement with the fully developed axial velocity profiles of rotating smooth duct reported by Hsieh et al. [85].

Table 5.2: Grid independence study for a laminar flow in a microchannel rotating at 3,000 RPM with a Reynolds number of 691

Grid Size (CV)	Number of CVs	% Diff	$\frac{w_{max}}{w_{in}}$	% Diff	Nu_{avg} (bottom wall)	% Diff
$11 \times 11 \times 20$	2,420	-	1.770	-	20.365	-
$15 \times 15 \times 30$	6,750	178.93	1.796	1.469	18.088	11.18
$21 \times 21 \times 40$	17,640	161.33	1.802	0.334	14.894	17.65
$31 \times 31 \times 60$	57,660	226.87	1.819	0.943	12.987	12.81
$35 \times 35 \times 90$	110,250	91.21	1.820	0.055	12.695	2.25
$41 \times 41 \times 100$	168,100	52.47	1.821	0.055	12.420	2.17
$43 \times 43 \times 120$	221,880	31.99	1.822	0.055	12.365	0.44

Table 5.3: Code validation for laminar forced convection through a square channel with uniform wall temperature

Results	$\frac{w_{max}}{w_{in}}$	fRe	Nu_{avg}
Present Simulation	2.092	14.16	3.007
Shah and London [83]	2.096	14.23	2.976
% Difference	0.19	0.49	1.04

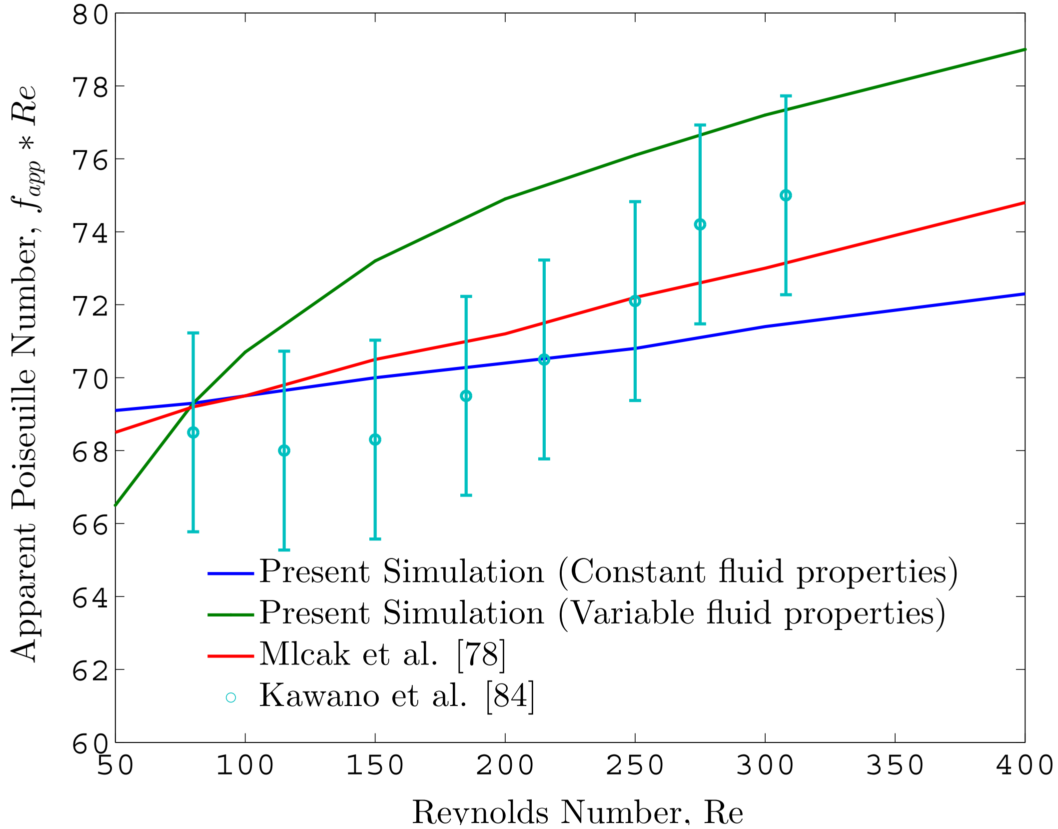

Figure 5.2: Benchmarking of present computational results with the numerical results of Mlcak et al. [78] and the experimental results of Kawano et al. [84]

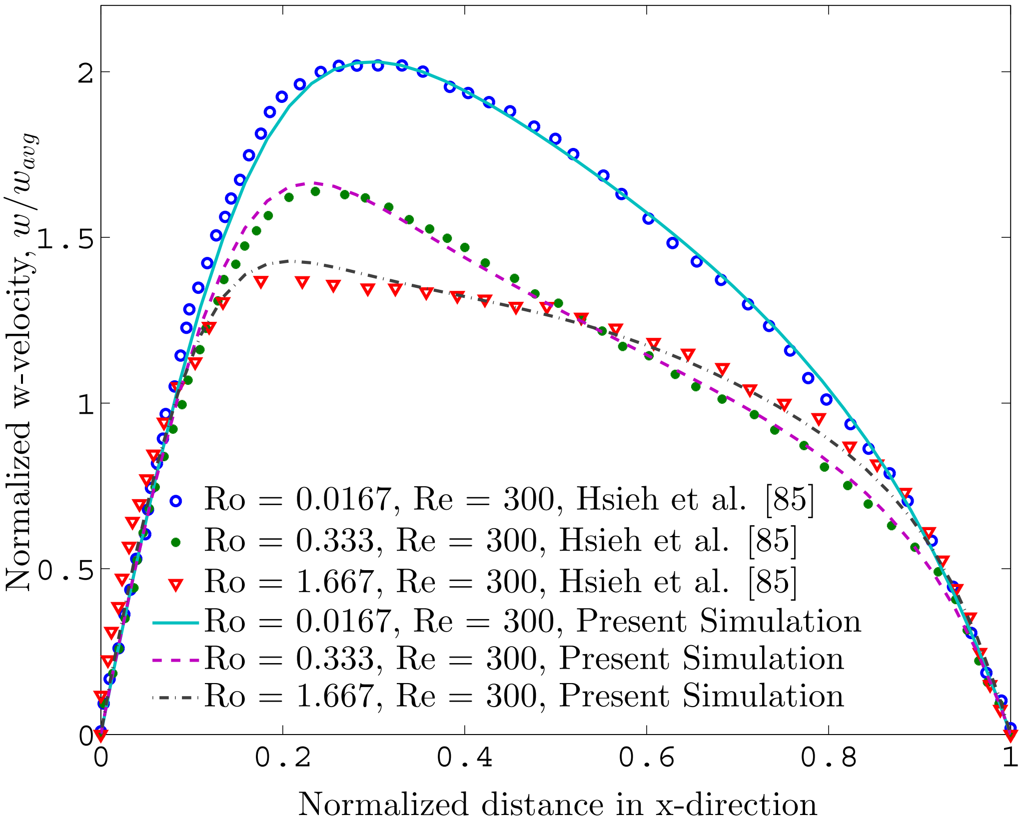

Figure 5.3: Comparison of present simulation results for fully developed axial velocity profiles along x with the numerical results of Hsieh et al. [85]

5.5 Results and Discussions

In this section we will discuss the primary findings of the numerical simulation of liquid flow in radially rotating microchannels with no slip boundary conditions at the walls. The detailed modeling, analysis and results on flow and heat transfer can be found in a recent article published by the author [86].

5.5.1 Flow Analysis

During the numerical simulation it is possible to vary the flow Reynolds number and rotational speed independently. Thus, we can vary one of these two parameters keeping the other constant. Our first numerical experiment will be based on this method. The geometry chosen for this case is the same as that of the experimental work of Kawano et al. [84]. The rotational speed was varied between 0 RPM (no rotation) to 2,850 RPM and for each rotation, the Reynolds number was varied between 50 and 800 in a controlled manner. The case of 0 RPM corresponds to a straight stationary channel flow and the inlet velocity for this case was specified based on the flow Reynolds number. Figure 5.4 shows the fully developed axial (w) velocity profiles along x-axis at y-mid-plane (y = b/2) for Re = 400 and different rotating speeds. Since the Coriolis force term ($2\omega w$) in Equation 5.4 scales directly with $|w|$, we can get an idea of the variation of the Coriolis force from the variation of the w-velocity profile with increase in rotational speed. From Figure 5.4, it can be observed that for low rotation ($\sim$57 RPM), the velocity profile is almost exactly the same as that of a non-rotating (0 RPM) microchannel. As the rotational speed is increased to 570 RPM, the w-velocity profile starts to deviate from its symmetric nature but the deviation is very small. Even at a relatively high rotation speed of 2,850 RPM, the difference from the 0 RPM w-velocity profile is low. Consequently, the flow is not much affected by the Coriolis force for this particular geometry ($a = 180\,\mu\text{m}$ and $b = 57\,\mu\text{m}$). Another interesting observation is that, at a lower Reynolds number, this difference is even smaller. The reason behind this small deviation lies in the dimensionless rotational Reynolds number (Re_ω). Since the height and width of the microchannel is very small, the hydraulic diameter is also very small ($\sim 86.58\,\mu\text{m}$). Consequently, even if the rotational speed is increased up to 2,850 RPM, the rotational Reynolds number Re_ω has a very low value of 3.0. For this case, the Coriolis force is roughly one-third of the centrifugal force (β=0.375). Thus, the flow is dominated by the primary flow direction (a combination of inertia and centrifugal force), and the Coriolis force is negligible. This implies that if this microchannel is used to mix two fluids, the mixing will be diffusion dominated even at a high rotational speed. However, in practice, for microfluidic devices, it is not possible

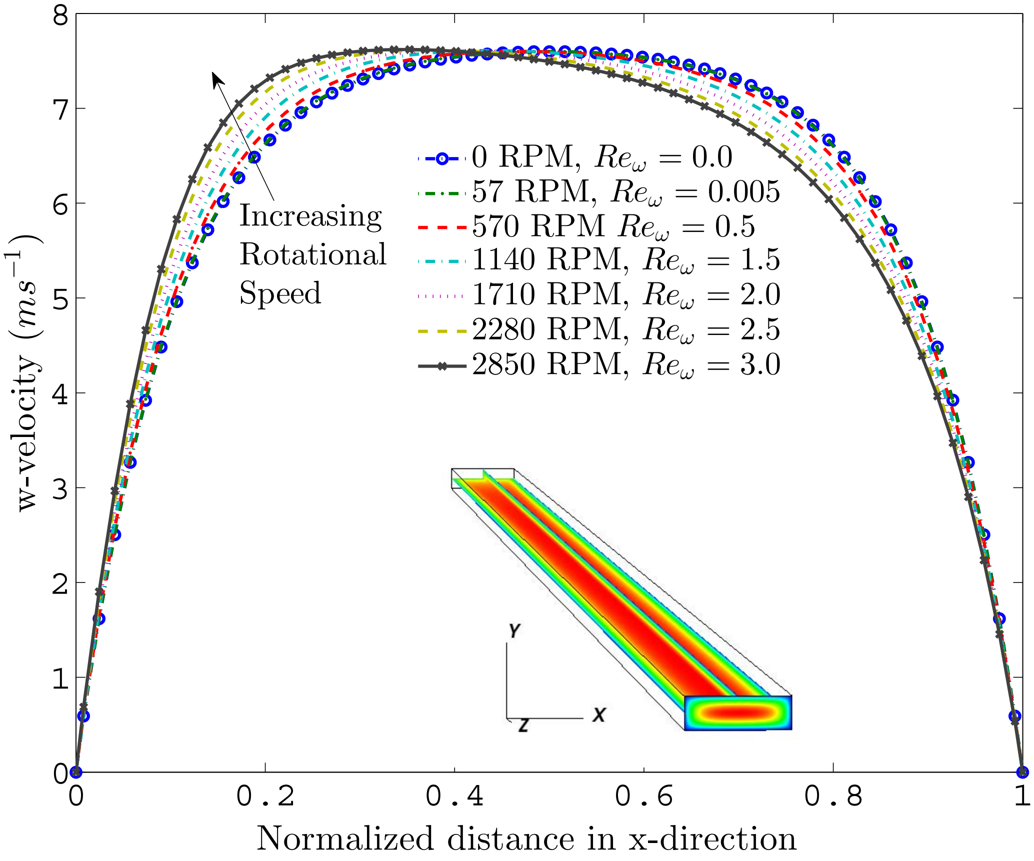

Figure 5.4: Axial velocity profiles along x axis at y-mid-plane (y = b/2) of channel outlet for low rotational Reynolds number. Channel width = 180 µm, Channel height = 57 µm, $\alpha = 3.16$, $Re = 400$. The three-slice of velocity contours for $Re_\omega = 3.0$ is shown in the inset.

to simultaneously control both the rotational speed and Reynolds number. In most of the centrifugal microfluidic devices, the fluid is kept in a reservoir and the disk is rotated at a certain rotating frequency. As a result, fluid from the reservoir flows through the microchannel due to the centrifugal force just like a pressure driven flow

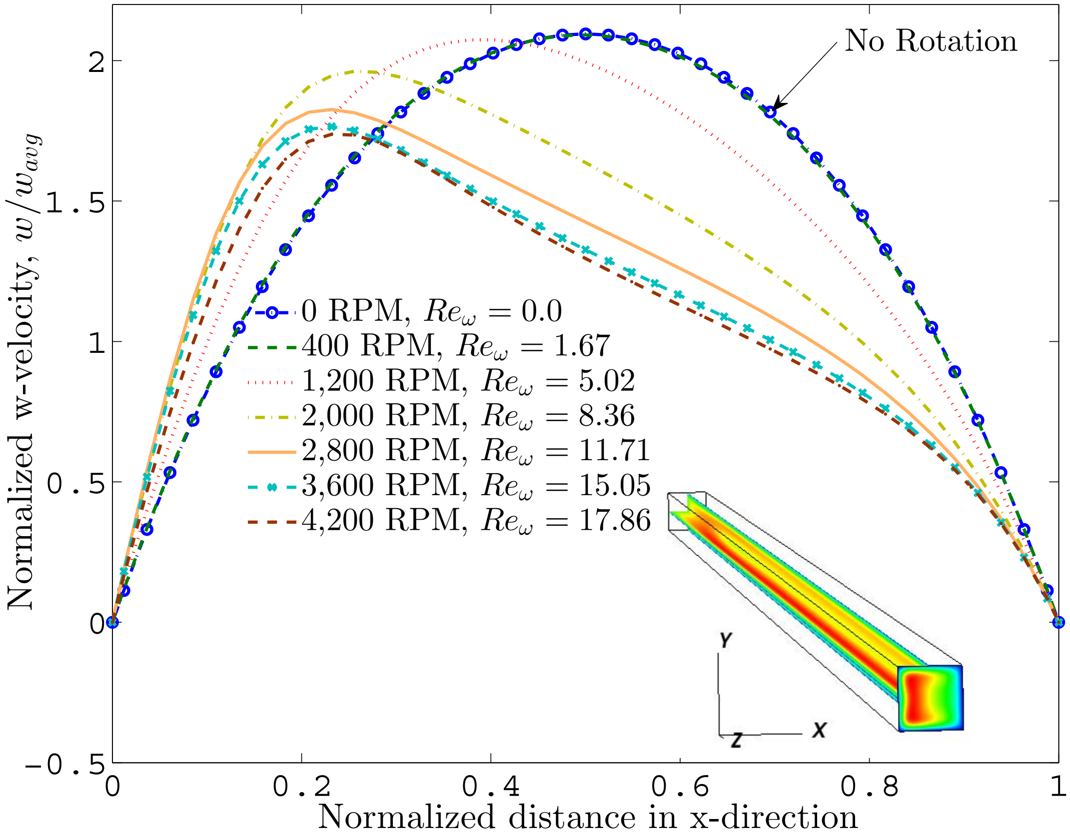

Figure 5.5: Axial velocity profiles along x axis at y-mid-plane (y = b/2) of channel outlet for high rotational Reynolds number. Channel width = 200 µm, Channel height = 200 µm, $\alpha = 1.0$. The three-slice of velocity contours for $Re_\omega = 17.86$ and 4,200 RPM is shown in the inset.

occurs due to the pressure difference between channel inlet and outlet. Once the rotating frequency is fixed, the velocity (and the Reynolds number) of the fluid inside the microchannel is also fixed. Thus, the rotating speed and the Reynolds number or fluid velocity is coupled in a centrifugally driven flow. In order to account for this coupled nature, first we chose a certain rotating speed (RPM) of the disk. With this rotating speed, we then calculated the average fluid velocity inside the microchannel using Equation 5.11b. As the fluid properties and channel dimensions are known, the Reynolds number can be easily calculated at this point. This Reynolds number or the average velocity is given as the boundary condition at the channel inlet.

Our next chosen geometry has a relatively large hydraulic diameter of 200 µm. By applying the procedure discussed above, the average velocities and Reynolds numbers are calculated for rotational speeds ranging from 400 RPM to 4,200 RPM (Table 5.1). For each case, the calculated average velocity is used as the inlet velocity boundary condition. Figure 5.5 shows the variation of axial (w) velocity profiles along x-axis at y-mid-plane (y = b/2) for different rotational speeds for a 200 µm × 200 µm microchannel flow (aspect ratio $\alpha = 1.0$). Comparing Figures 5.4 and 5.5, it is evident that for the same rotational speed, the deviation of velocity profiles from a non-rotating channel flow is much higher for a microchannel with a larger hydraulic diameter. Since the hydraulic diameter is larger in this case, even a low rotational speed can produce a high rotational Reynolds number hence a strong secondary flow can be induced by Coriolis force. The effect of Coriolis force is to generate a transverse velocity component perpendicular to the main flow direction which causes the flow profile to deviate from the usual symmetric profile of a non-rotating channel flow. As a result, the maximum axial velocity shifts from the centerline and the direction of shifting depends on the sense of rotation. In this case, the disk is rotating clockwise around the y-axis and thus the maximum point of axial velocity profile shifts to the left. Consequently, the Coriolis force attains its maximum value at that location since it is directly proportional to the axial velocity, w. The shifting of maximum w-velocity and Coriolis force is more evident in Figure 5.6. It represents the pseudocolor of w-velocity at the cross-section of the channel outlet for different rotational speeds and rotational Reynolds numbers. The minimum and maximum velocities are represented by blue and red regions respectively. It can be seen from Figure 5.6 that at low rotational speeds ($\sim 400\,\mathrm{RPM}-800\,\mathrm{RPM}$), the velocity is lower in the near wall region (marked by blue region) due to the no slip velocity boundary conditions at the walls. In the center of the channel cross-section, a higher velocity region (marked by red region) is observed which is similar to the velocity profile of a non-rotating channel flow. Thus, for low rotational speeds ($\sim 400\,\mathrm{RPM} - 800\,\mathrm{RPM}$), a weak secondary flow is generated which has negligible effect on the primary flow. As the rotation increases ($> 1,200$ RPM), the secondary flow becomes stronger, which drives the axial flow from the center towards the left wall of the microchannel. At a higher rotational speed ($\sim$ 3,600 RPM), the core of the maximum velocity starts to form a concave shape near the left wall region (Figure 5.6j). This shape is more clearly visible for 4,000 and 4,200 RPM. This observation in Figure 5.6(k-l) is an indication of the onset of secondary vortices (transition from two cell state to four cell state), which has been already reported in the literature of roll cell instabilities in rotating channel flow (Hwang and Jen [87]; Tien-Chien et al. [88]). The secondary vortices can be clearly seen from the streamline plot of velocity magnitude at 4,200 RPM in Figure 5.7. In our study, the appearance of secondary vortices have also been proven by simulating rotating flow in a channel with a larger dimension ($500\,\mu\mathrm{m} \times 500\,\mu\mathrm{m}$) where rotational Reynolds number is much higher (not shown here). In a recent numerical study of rotating channel flow by Zhang et al. [89], time-dependent and force-dependent transition of secondary flow from two cell states to four cell states and even six cell states have been reported at low rotational Reynolds number ($Re_\omega < 0.1$). They applied periodic boundary conditions at the inlet and outlet of the channel and assumed that the flow field is independent of the axial direction. However, in their study, as the rotational Reynolds number Re_ω was very low (< 0.1), the secondary vortices were not strong enough to distort the symmetric nature of the primary flow. On the contrary, as reported in our study, at higher Re_ω the generation of secondary vortices shifts the axial flow which can significantly enhance the mixing of two fluids. Thus, when mixing is the purpose of a centrifugal microfluidic device, triggering recirculation zones by secondary vortices at higher rotational Reynolds number can be of crucial importance. In order to analyze the secondary flow strength of the rotating microchannel flow, secondary velocity profiles in a transverse plane have been plotted in Figure 5.8. In this figure, the variation of u-velocity profile along x-axis at y-mid-plane (y = b/2) indicates the effect of Coriolis force. At low rotational speed ($\sim$ 800 RPM), the Coriolis force is small and hence the magnitude of secondary velocity is also very small. As the rotational speed increases, the Coriolis force increases resulting in an increase of the secondary velocity. For example, at 2,400 RPM, the maximum value of u-velocity is approximately two times higher than the inlet or average axial velocity. When the rotational speed is increased further ($\sim$ 4,200 RPM), a flow reversal of u-velocity can be observed near the left wall. This again indicates the generation of secondary vortices at high rotational Reynolds number.

Thus, to effectively utilize the Coriolis force or secondary flow phenomena in a centrifugal microfluidic device, we should choose such a geometry where the rotational Reynolds number is high. For smaller channel dimensions, even if we operate the disk at a high rotating speed, the rotational Reynolds number will still not be so high as to impact the transverse flow. For example, if water flows through a channel

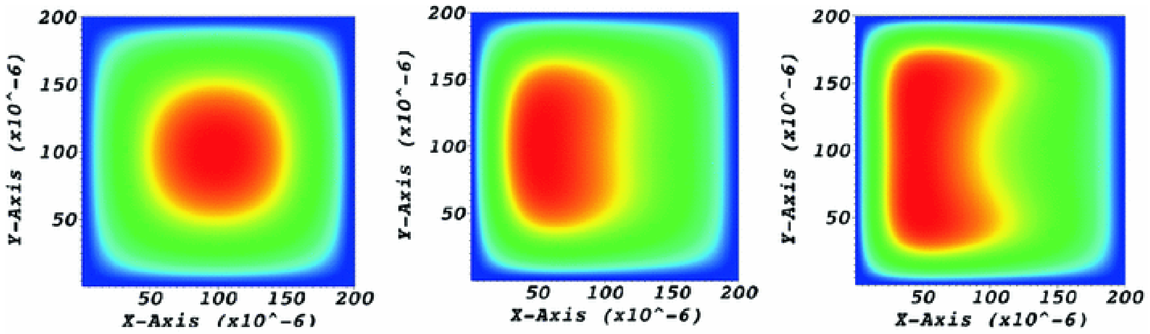

(a) Re = 12, Re_{ω}=1.67, RPM=400 **(e)** Re = 307, Re_{ω}=8.36, RPM=2000 **(i)** Re = 786, Re_{ω}=13.38,RPM=3200

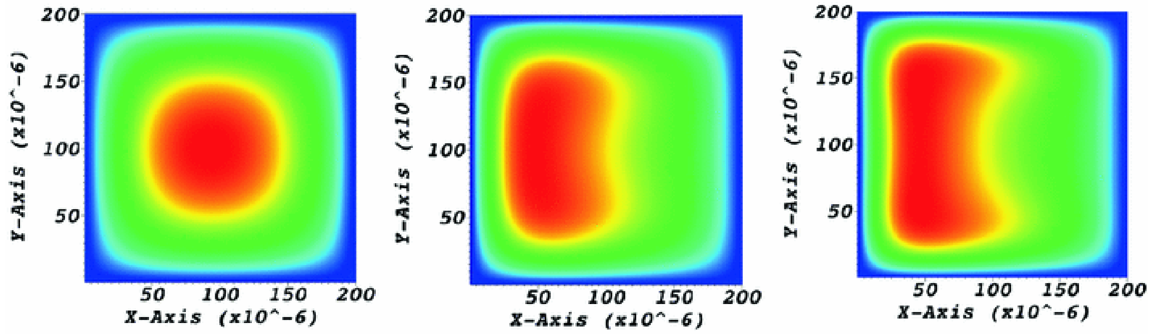

(b) Re = 49, Re_{ω}= 3.34, RPM=800 **(f)** Re = 442, Re_{ω}=10.03, RPM=2400 **(j)** Re = 995, Re_{ω}= 15.05,RPM=3600

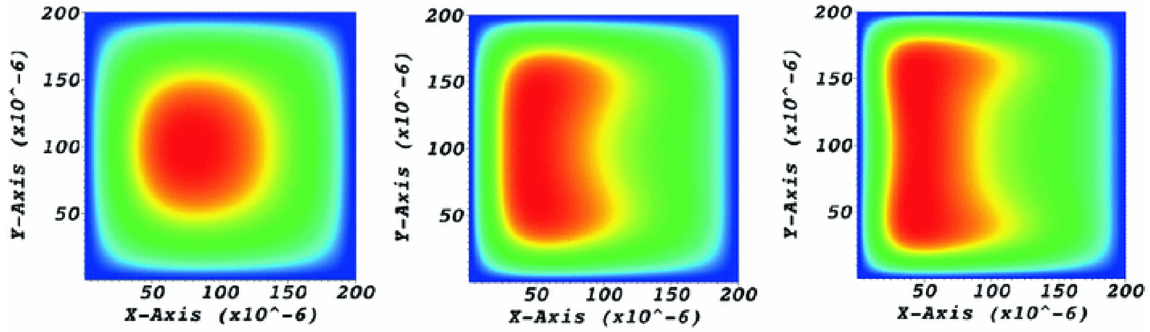

(c) Re =110,Re_{ω}=5.02,RPM=1200 **(g)** Re = 602, Re_{ω}=11.70, RPM=2800 **(k)** Re =1228, Re_{ω}=16.72,RPM=4000

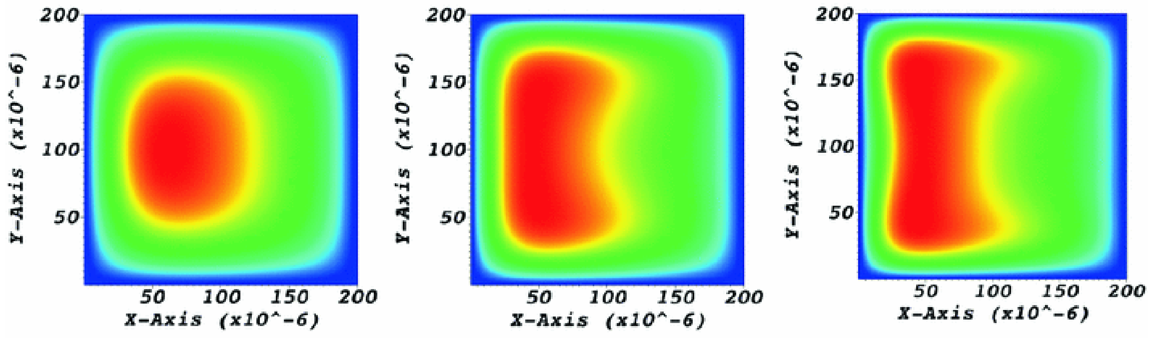

(d) Re =197, Re_{ω}=6.69,RPM =1600 **(h)** Re = 691,Re_{ω}=12.54,RPM=3000 **(l)** Re = 1354, Re_{ω}=17.56,RPM=4200

Figure 5.6: Velocity contour plots at the outlet of a rotating microchannel with $\alpha = 1.0$

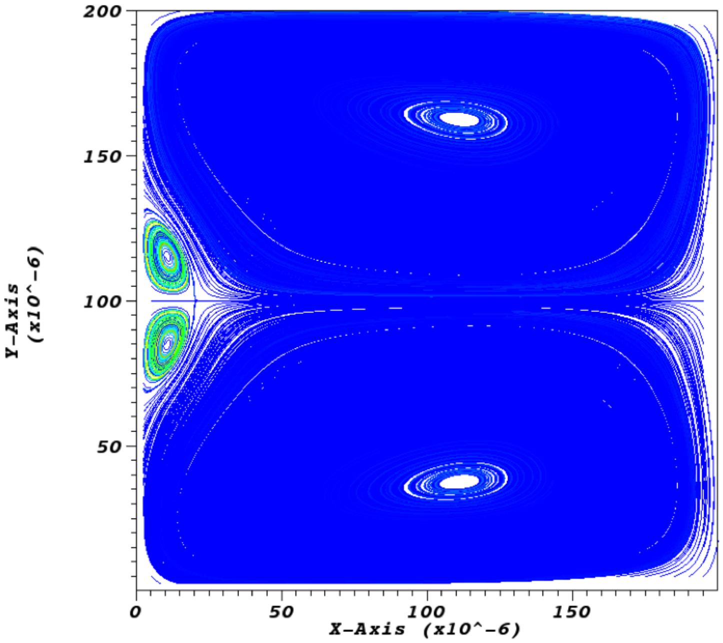

Figure 5.7: Streamline plot of velocity magnitude at the channel outlet for RPM = 4200, $Re_\omega = 17.56$ with $\alpha = 1.0$

with a hydraulic diameter of 100 µm, even rotating at 3,000 RPM it will produce a rotational Reynolds number of 3.14 which is still low for generating enough Coriolis force to affect the primary flow in the axial direction. On the other hand, if the channel has a hydraulic diameter of 400 µm, the same rotating speed of 3,000 RPM can produce a rotational Reynolds number of 50.26, which is 16 times higher. This is also intuitive as Re_ω scales with the square of the hydraulic diameter.

In addition to the above geometries, six more geometries with aspect ratios α = 0.11, 0.25, 0.5, 2.0, 4.0, and 9.9 have been considered in this study keeping the hydraulic diameter constant (see Table 5.1). In these channels, the velocity profiles exhibit a similar kind of behavior as stated above.

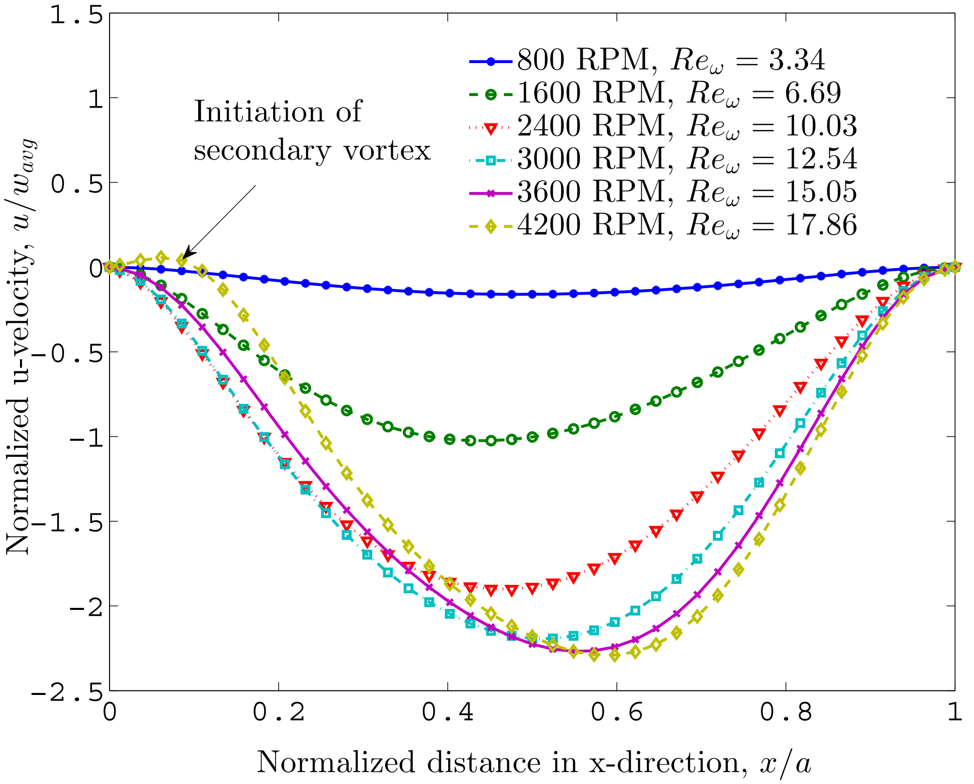

Figure 5.8: Secondary velocity (u-velocity) profile along x-axis at y-mid-plane (y=b/2) of channel outlet for $\alpha = 1.0$

5.5.2 Critical Rotational Reynolds Number

Using the approximate analytical solutions of a purely centrifugal flow described in [86], we can determine for what values of rotational Reynolds number Re_ω the analytical expressions are applicable. To do this, we took the root mean square (RMS) deviation of normalized axial velocity of rotating microchannel flow simulation from that of approximate analytical solution for the same dimension at each rotating frequency. As the Coriolis force increases with the increase of rotating frequency, the deviation of a velocity profile from its symmetric nature will be more prominent. The RMS deviations from purely centrifugal flow velocity profiles against rotational speeds and rotational Reynolds numbers have been plotted in Figure 5.9 for channel aspect ratios of $\alpha = 0.11$, 0.25, 0.5, 1.0, 2.0, 4.0, and 9.09. In general, the deviation is small for low rotational speeds and low rotational Reynolds numbers. But, it increases depending upon the aspect ratio of the channel as the rotational frequency is increased. For higher aspect ratio ($\alpha > 1.0$) the deviation is lower. The reason behind this is that for high aspect ratio channel, the cross-sectional area is large and thus for a certain rotating frequency the amount of fluid entering the microchannel is higher compared to the low aspect ratio channel resulting in a decrease of average velocity hence a lower Reynolds number. Since the Coriolis force is not affected by rotating frequency alone but a combination of Reynolds number and rotating speed, the secondary flow effect on axial (w) velocity profiles for higher aspect ratio is lower. As a result, the RMS deviation from analytical result increases for $\alpha = 9.09 - 1.0$. However, as the channel aspect ratio is decreased from 1.0, the RMS deviation decreases and the decrease is far more prominent than wide high aspect ratio channels. For $\alpha = 0.5$, the RMS deviation is almost similar to the RMS deviation curve for $\alpha = 4.0$. For $\alpha = 0.25$ and 0.11, the RMS deviation is much lower than $\alpha = 9.09$.

Thus, for a fixed hydraulic diameter, the effect of rotation is maximum for a square microchannel ($\alpha = 1.0$). At high and small aspect ratios, one of the dimensions of the rectangular channel will be very small. This increases the viscous diffusion effects, which in turn suppress the secondary flow due to rotation. For $\alpha > 1.0$, the viscous diffusion effect is dominant in y-direction, which is perpendicular to the direction of the Coriolis force, and for $\alpha < 1.0$, the viscous diffusion effect is dominant in the x-direction, which acts along the direction of the Coriolis force. That is why, the RMS deviation is much smaller for $\alpha < 1.0$ than the corresponding RMS deviation in microchannels with $\alpha > 1.0$.

If we consider a 10% tolerance in RMS deviation, we can define a critical rotational Reynolds number ($Re_{\omega,cr}$) above which the predictions of the analytical expressions will be inaccurate. For $\alpha = 0.25$, 0.5, 1.0, 2.0, 4.0, and 9.09, the cut-off values of Re_ω, cr are 14.0, 5.5, 3.8, 4.7, 6.5, and 10.0, respectively. For $\alpha = 0.11$, the effect of Coriolis force is so small, that the RMS deviation is only about 3% even for a high rotational Reynolds number, $Re_\omega = 17.2$. The geometry with aspect ratio 9.09 is similar to the geometry used in the experimental work of Chakraborty et al. [9]. Using a 1,000 µm × 100 µm microchannel, they observed that the Coriolis force-based mixing region between two fluids starts at $\beta = 1.0$ or $Re_\omega = 8.0$, but the effective mixing process (determined by the mixing length) occurs beyond $\beta > 1.35$ or $Re_\omega > 10.8$. However, no explanation was given for why the mixing length increased between $1.0 < \beta < 1.35$. The mixing length was defined as the axial length of the channel required to decrease the standard deviation of the pixel intensity across the channel by 90% of the value at the inlet [9]. The increase of the mixing length for $1.0 < \beta < 1.35$ can be explained with the RMS deviation curve of the present simulation for $\alpha = 9.09$. When the rotational speed is low (between 400 and 2,000 RPM), the RMS deviation is small (within 6%) and any mixing in this region will

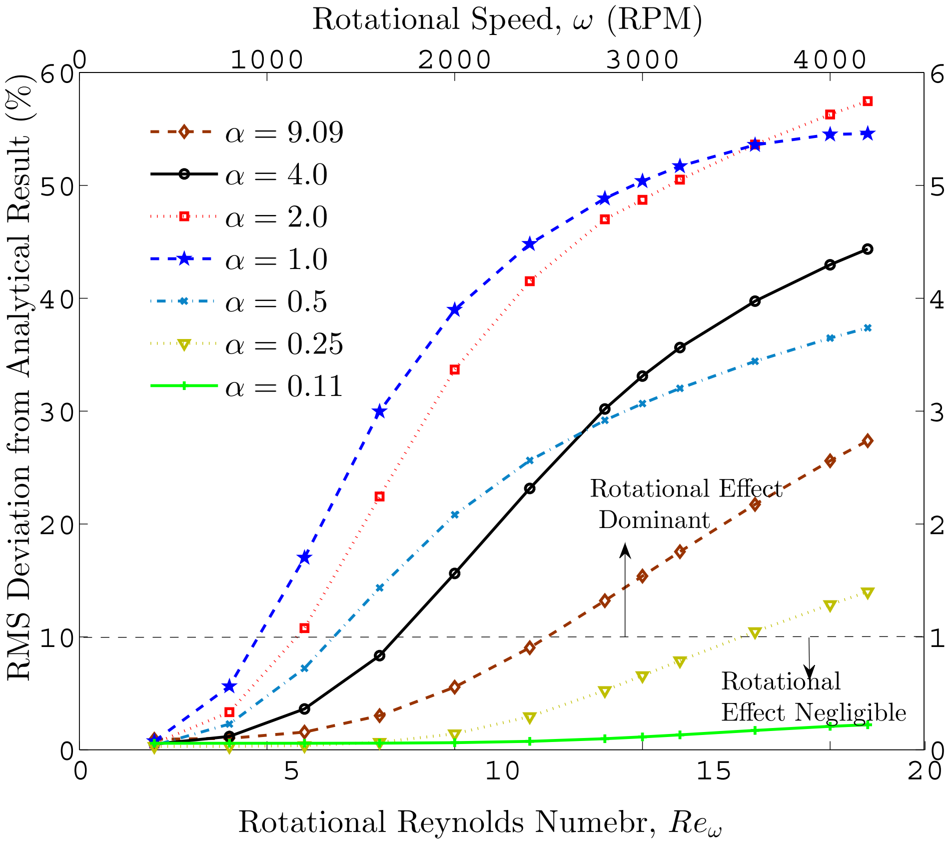

Figure 5.9: RMS deviation of outlet axial velocity profiles of rotating microchannel from the predicted analytical result

be diffusion dominated (named as diffusion-based mixing in Chakraborty et al. [9]). Above 2,000 RPM, although rotational frequency is high, the RMS deviation is still small ($< 10\%$) and the flow will be regulated by the centrifugal force which will dominate over the diffusion process since its direction is along the primary flow direction. Consequently, a reduction in mixing process will occur in this region ($8.0 < Re_\omega < 10; 2,000 < RPM < 2,500; 1.0 < \beta < 1.35$) until the Coriolis force becomes strong enough to dominate over the centrifugal force. Above $Re_\omega > 10$, the RMS deviation is greater than 10% and it increases rapidly with the increase of rotational speed. The effective Coriolis force-based mixing is observed in this region.

Another implication of Figure 5.9 is that, the transverse flow effect by Coriolis force is more prominent for relatively lower aspect ratio channels ($\alpha = 1.0$ and 4.0). This observation may seem contradictory from the results of Ducree et al. [11], where they have shown that mixing is enhanced by using wide high aspect ratio channels. However, in studying the effect of aspect ratio, they increased the width of the channel keeping the height fixed resulting in an increase of cross sectional area. Thus, the hydraulic diameter for wide high aspect ratio channel was increased which in turn increased the rotational Reynolds number and consequently favorable mixing behavior was observed. For example, when the channel width a = 250 µm and height b = 100 µm ($\alpha = 2.5$), the hydraulic diameter D_h is approximately 143 µm, resulting in a rotational Reynolds number $Re_\omega = 1.0$ for a rotational speed $\omega = 50$ rad/s. On the other hand, when the channel width is increased to 500 µm keeping all other parameters unchanged ($\alpha = 5.0$), the hydraulic diameter $D_h = 167$ µm and the rotational Reynolds number Re_ω= 1.4. Thus, even the aspect ratio has been increased in this case, the rotational Reynolds number increases, which in turn increase the effect of Coriolis force and hence effects the mixing favorably.

5.5.3 Critical Aspect Ratio and Experimental Validation

From the results of the Subsection 5.5.2, it is possible to plot the variation of the critical Reynolds number with the aspect ratio, which is shown in Figure 5.10. From this figure, we can clearly observe that the lowest critical rotational Reynolds number occurs for the aspect ratio $\alpha = 1.0$ i.e for a microchannel with a square cross-section. Below $\alpha = 1.0$, there is a rapid increase in critical Reynolds number with aspect ratios indicating a rapid reduction of the secondary flow effect. Above $\alpha = 1.0$, the critical rotational Reynolds number also increases, but this time the rate of increase in $Re_{\omega,cr}$ with the aspect ratio is much more gradual than the previous case. From this observation, sub-critical and super-critical modes of operations for rotating microchannel flow can be defined based on the lowest or critical value of the aspect ratio $\alpha_{cr} = 1.0$. In the sub-critical mode ($\alpha < \alpha_{cr}$), a small reduction in aspect ratio will lead to a large increase in viscous force which will suppress the Coriolis force resulting in a decrease in mixing phenomena between fluids. In the super-critical mode ($\alpha > \alpha_{cr}$), a small increase in aspect ratio will decrease the effect of Coriolis force, but this time the effect of viscous force is not as dominant as it was in the sub-critical mode for a corresponding aspect ratio. Thus, optimal effect of secondary flow e.g. optimal mixing between two fluids will be experienced near α_{cr}. However, it should be noted that, the mixing process in micorchannels will also be affected by other factors such as retention time and the width of the channel. Nevertheless, the above findings can be very useful in designing microchannel for enhancing mixing operations in centrifugal microfluidics.

The scale-up on mixing in rotating microchannels under sub-critical and super-critical modes has also been reported and experimentally validated by Leung and Ren

[90]. By studying the mixing quality[1] of two fluids in a T-microchannel for various aspect ratios, they identified a similar critical aspect ratio where optimal mixing was observed (shown in Figure 5.11). From the numerical simulations, they determined that the critical aspect ratio is approximately 0.40 i.e $\alpha_{cr} \approx 0.40$. However, from their experimental data, the optimal mixing was observed for a width-to-height ratio of unity i.e. $\alpha_{cr} = 1.0$, which is exactly what we predicted and reported in [86].

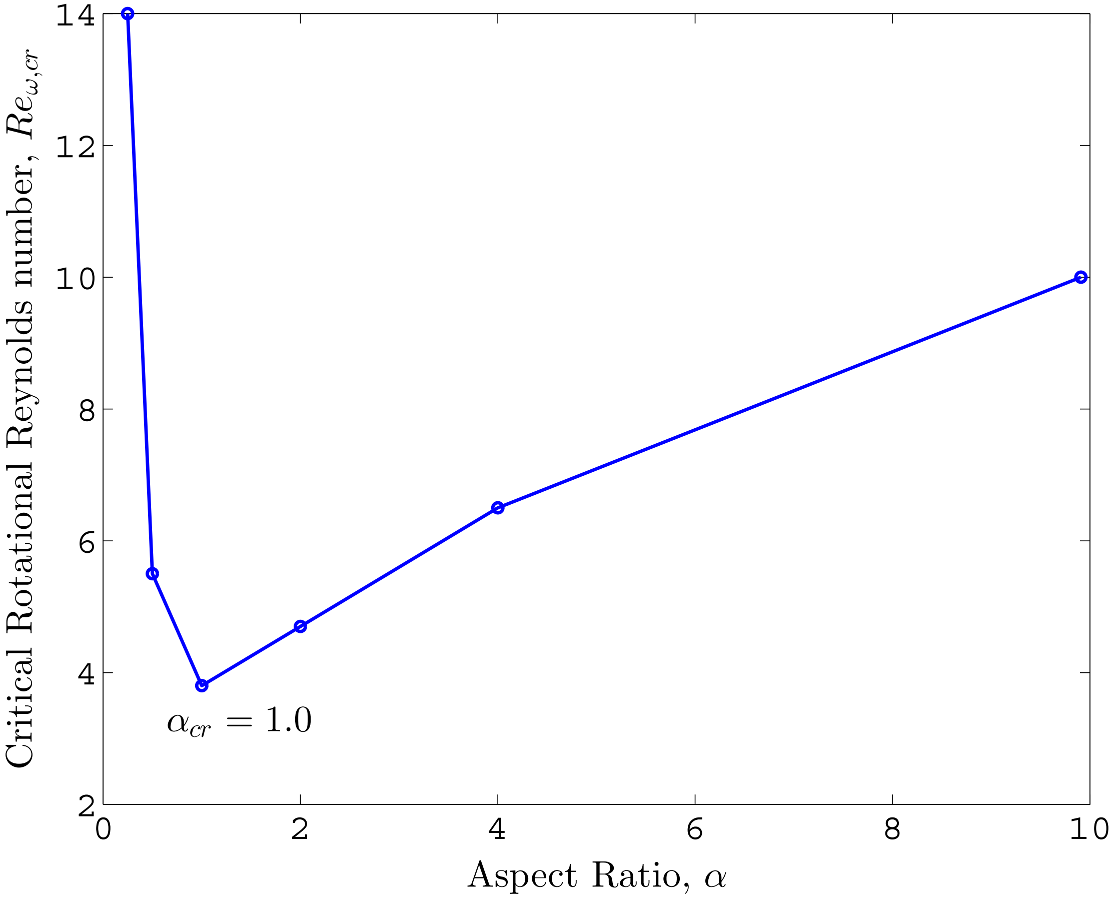

Figure 5.10: Variation of critical rotational Reynolds number with aspect ratios

---

[1] A zero value of mixing quality indicates no mixing and a value of unity indicates a perfect mixing

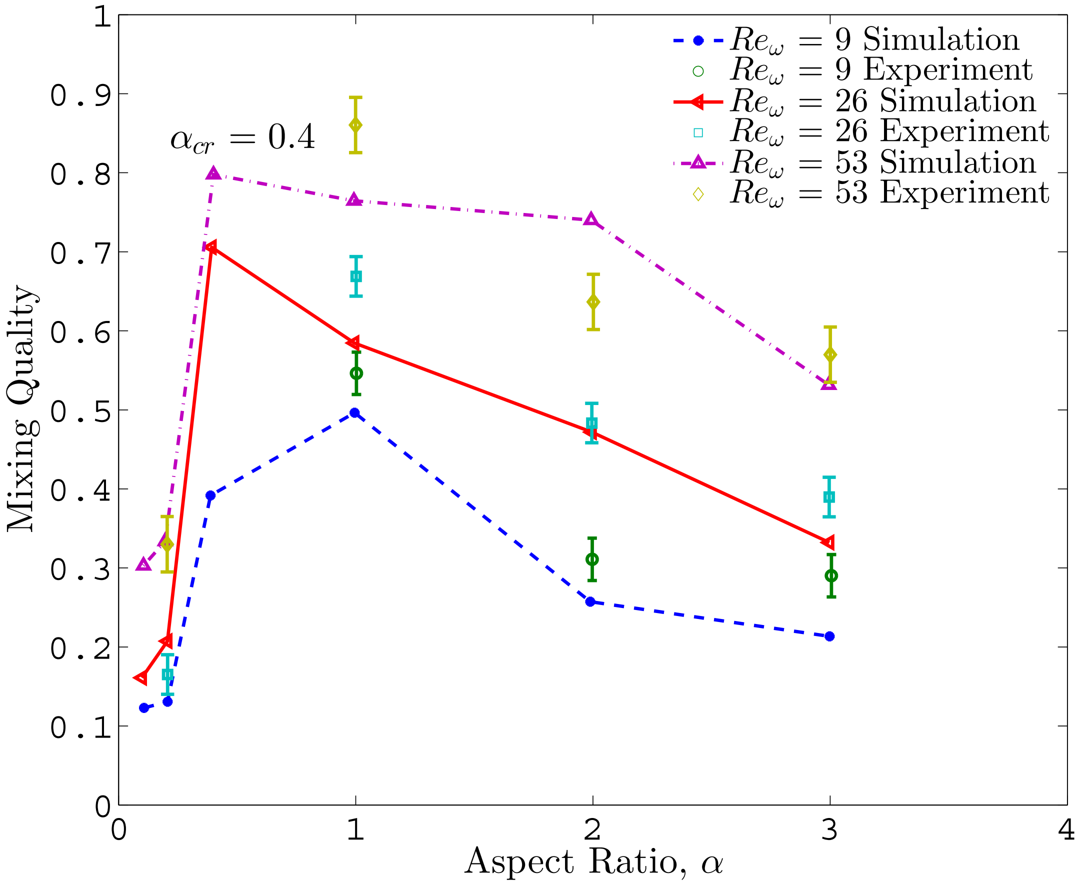

Figure 5.11: Variation of mixing quality with aspect ratio. The data are taken from Leung and Ren [90]

5.6 Conclusions

A numerical investigation was performed for a steady flow inside a rectangular microchannel rotating around the y-axis assuming no slip boundary conditions. The rotational mode was orthogonal i.e. the rotation axis (y) was perpendicular to the main flow direction (z). Steady state incompressible Navier-Stokes equations were solved computationally by using a pressure based finite volume method. The main findings of this investigation can be summarized as follows:

(i) In a radially rotating microchannel flow, the effect of Coriolis force or secondary flow is primarily determined by the value of rotational Reynolds number Re_ω. Even with a high rotational speed, the flow can deviate little from the symmetric parabolic profile of a non-rotating channel flow due to the small size of the microchannel, which results in a low rotational Reynolds number. Thus, for a fixed rotational speed, the strategy to increase the effect of secondary flow (e.g. in mixing process) is to increase the cross sectional area or the hydraulic diameter of the microchannel.

(ii) For a clockwise rotation around y-axis, the axial velocity profile (w) along x-axis shows asymmetric behavior with a maximum value near the left wall. Consequently the maximum of Coriolis force ($2\omega w$) also shifts to the left wall. A pair of vortices appears as a result of this Coriolis force induced secondary flow. At higher values of Re and Re_ω, a secondary pair of vortices can appear.

(iii) The RMS deviation of the velocity profile for a rotating microchannel flow from that of a purely centrifugal flow increases with the increase in rotational Reynolds number, Re_ω. The approximate analytical solution for velocity distribution of a purely centrifugal flow is valid only when the RMS deviation is below 10%. It was observed that, for $\alpha = 0.25$, 0.5, 1.0, 2.0, 4.0 and 9.09, the RMS deviation is within 10% when Re_ω is less than 14.0, 5.5, 3.8, 4.7, 6.5 and 10.0, respectively. For very high or low aspect ratio microchannels, the viscous diffusion effect is strong enough to suppress the secondary flow effect. However, the diffusion effect is more prominent for low aspect ratio channels ($\alpha < 1.0$) than high aspect ratio channels ($\alpha > 1.0$).

(iv) By plotting the critical rotational Reynolds number ($Re_{\omega,cr}$) for different aspect ratios, a critical value of aspect ratio (α_{cr}) can be defined and sub-critical and super-critical modes of operations for rotating microchannel flow can be identified. From our numerical experiments, we have found the critical aspect ratio to be 1.0 i.e. $\alpha_{cr} = 1.0$.

6. LIQUID SLIP AND HEAT TRANSFER*

6.1 Introduction

In this chapter, we will study the liquid slip phenomena inside a microchannel subjected to a uniform rotation. The present work has been already reported by the author in [91]. The objectives of this chapter are:

(i) To obtain a numerical solution to the momentum equations of a liquid flow through an array of rotating rectangular microchannels subjected to the slip boundary condition at the walls.

(ii) To numerically solve the energy equation with a thermally repeated boundary condition in the cross-flow direction and study the heat transfer characteristics.

(iii) To obtain an approximate analytical solution for a fully developed purely centrifugal flow with the slip boundary condition at the walls.

(iv) To explore the combined effect of rotation and slip flow on fluid flow and heat transfer.

6.2 Model Problem and Analysis

6.2.1 Geometry and Independent Parameters

The model problem considered in this chapter is the same as the previous chapter. Table 6.1 shows the independent parameters used for the simulations performed in this study. Microchannels of five different aspect ratios with a hydraulic diameter of

---

*Part of this chapter is reprinted with permission from P. Roy, N. K. Anand, and D. Banerjee. Liquid slip and heat transfer in rotating rectangular microchannels. *International Journal of Heat and Mass Transfer*, 62:184-199,2013. Copyright 2013 by Elsevier.

200 µm were considered. For each aspect ratio, the rotational frequency was varied from 0 RPM (i.e. no rotation) to 3,200 RPM in a step of 400 RPM. For each of these cases (1-5), the slip length was also varied from 0 0 µm (i.e. no slip boundary condition) to 10 µm. The remaining case (6) was considered for benchmarking the code against the experimental results of liquid slip in a non-rotating microchannel [27].

Table 6.1: Geometrical and rotational parameters

Case	Aspect Ratio α	Channel Width a (μm)	Channel Height b (μm)	Hydraulic Diameter $D_h(\mu m)$	Rotational Speed (RPM)	Slip Length $\lambda(\mu m)$
1	1.0	200	200	200	0-3,200	0-10
2	2.0	300	150	200	0-3,200	0-10
3	4.0	500	125	200	0-3,200	0-10
4	10.0	1,100	110	200	0-3,200	0-10
5	20.0	2,100	105	200	0-3,200	0-10
6	10.0	300	30	54.54	0	0-1

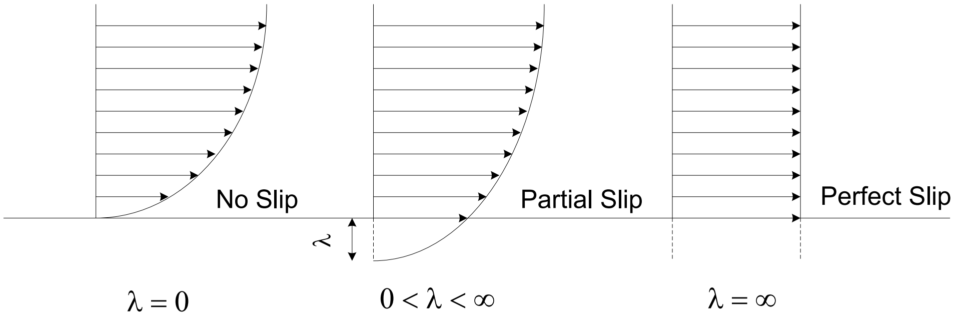

Figure 6.1: Significance of slip length λ (adapted from Lauga et al. [15])

6.2.2 Boundary Conditions

A uniform fluid velocity with prescribed temperature was applied at the inlet. As the microchannel length to hydraulic diameter ratio was very high, the flow at the channel outlet was treated with a locally parabolic boundary condition i.e. $\partial w/\partial z\Big|_{z=L} = 0$. The microchannel walls were considered hydrophobic or superhydrophobic and slip boundary conditions were used at the microchannel walls. The slip boundary condition was first proposed by Navier [92] in 1823 , where he stated that the tangential fluid velocity at a solid surface is linearly proportional to the rate of strain (also known as shear rate) i.e. the velocity gradient at the surface:

$$w_{slip} = w_{x_i=0} = \lambda \frac{\partial w}{\partial x_i}\Big|_{x_i=0}, i = 1, 2 \tag{6.1}$$

Here, the proportionality constant, λ, has a unit of a length and is commonly known as the slip length or slip coefficient. This slip length (λ) can be defined as the distance inside the wall, at which the extrapolated fluid velocity would equal to the wall's velocity [93]. Figure 6.1 illustrates the significance of slip length (λ). For $\lambda = 0$, the standard no slip boundary condition can be obtained. Partial slip occurs for $0 < \lambda < \infty$ and a perfect slip condition corresponds to $\lambda = \infty$. For further interpretation of slip length (λ), interested readers are referred to [16].

Due to the presence of hydrophobic/superhydrophobic surface, the temperature of the fluid particle adjacent to the wall is different from the temperature of the wall. This 'temperature jump' is determined by a thermally equivalent interfacial thermal resistance known as Kapitza resistance, R_k [16, 94], and [95]. In analogy with slip velocity (Equation 6.1), the temperature jump can be expressed as:

$$T_f - T_{wall} = l_k \frac{\partial T}{\partial x_i}\Big|_{x_i=0}, i = 1, 2 \tag{6.2}$$

Here, T_{wall} is the prescribed wall temperature and T_f is the temperature of the fluid particle adjacent to the wall. l_k is called the interfacial thermal resistance length or Kapitza length [95]. Similar to the slip length (λ), the Kapitza length (l_k) can be interpreted as the distance inside the solid to which the temperature profile must be extrapolated to reach the wall temperature. For a hydrophilic surface (with a contact angle of less than 90 degree), the Kapitza length (l_k) is indeed very small [94]. But, for a hydrophobic or superhydrophobic surface, the Kapitza length (l_k) can be comparable to the slip length [15]. If we compare the temperature jump in a solid-liquid interface to that in a gas microflow [21], the following relationship between the slip length (λ) and the Kapitza length (l_k) can be deduced:

$$l_k \approx \frac{\lambda}{Pr} \tag{6.3}$$

where Pr is the Prandtl number. From the above relationship, it can be observed that, for water ($Pr \approx 7$), even if the slip length λ is as high as $10\,\mu\mathrm{m}$, the Kapitza length l_k will have a value of approximately 1.4 μm. Thus, the Kapitza length or temperature jump is very small for most of the practical applications, especially for liquids with a high Prandtl number.

In the present simulation, a temperature jump boundary condition was used for the top and bottom walls and the Kapitza length l_k was approximated using Equation 6.3. The bottom and the top walls were maintained at constant temperature. A thermally repeated boundary condition was applied at the left and the right walls. This means that the temperatures at both the left and the right walls are equal and the heat flux leaving the left wall is equal to the heat flux entering the right wall [78]. Mathematically, the thermally repeated boundary condition can be expressed as follows:

$$T_{x=0} = T_{x=a}, -k_{eff}\frac{\partial T}{\partial x}\Big|_{x=0^-} = -k_{eff}\frac{\partial T}{\partial x}\Big|_{x=a^+} \tag{6.4}$$

Here, k_{eff} is the effective thermal conductivity which accounts for the conductivity of the water and the conductivity due to the Kapitza resistance of a thermally equivalent interface.

6.2.3 An Approximate Analytical Solution

Let us recall the governing equation (Eq. 5.5) for purely centrifugal flow mentioned in subsection 5.2.2. If we non-dimensionalize the x and y-coordinate with the hydraulic diameter (D_h) and the velocity w with $D_h^2/\mu\frac{\partial p^*}{\partial z}$, Equation 5.5 becomes:

$$\frac{\partial^2 W}{\partial X^2} + \frac{\partial^2 W}{\partial Y^2} = 1 \tag{6.5}$$

where $X = x/D_h$, $Y = y/D_h$ and $w/(D_h^2/\mu\frac{\partial p^*}{\partial z})$. The corresponding boundary conditions are:

$$W_{X=0} = \frac{\lambda}{D_h}\frac{\partial W}{\partial X}\Big|_{X=0} \tag{6.6a}$$

$$\left.\frac{\partial W}{\partial X}\right|_{X=a^+} = 0 \tag{6.6b}$$

$$W_{Y=0} = \frac{\lambda}{D_h}\left.\frac{\partial W}{\partial Y}\right|_{Y=0} \tag{6.6c}$$

$$\left.\frac{\partial W}{\partial Y}\right|_{Y=b^+} = 0 \tag{6.6d}$$

where $a^+ = \frac{a}{2D_h}$ and $b^+ = \frac{b}{2D_h}$. The equation (6.5) with the above boundary conditions is in the same form as proposed by Ebert and Sparrow [96] for slip flow in rectangular ducts. The only difference is that their equations were derived for rarefied gas flows and hence Knudsen number (Kn) was used in place of non-dimensional slip length (λ/D_h). Following the procedure of Ebert and Sparrow [96], the analytical solution for fully developed velocity profile in a rotating rectangular microchannel with negligible Coriolis force becomes:

$$W(X,Y) = \frac{a^+b^+}{4A}\sum_{k=1}^{\infty}\frac{cos(\varphi_k(Y-\frac{b^+}{2}))}{\varphi_k^3}\left(\frac{sin(\varphi_k b^+)}{b^+ + (\frac{\lambda}{D_h})sin^2(\varphi_k b^+)}\right) \times \left(1 - \frac{cosh(\varphi_k(X-\frac{a^+}{2}))}{cosh(\varphi_k a^+) + (\frac{\lambda}{D_h})\varphi_k sinh(\varphi_k a^+)}\right) \tag{6.7}$$

where

$$A = \sum_{i=1}^{\infty}\varphi_i^{-5}\left(\frac{sin^2(\varphi_i b^+)}{b^+ + (\frac{\lambda}{D_h})sin^2(\varphi_i b^+)}\right) \times \left(\varphi_i a^+ - \frac{tanh(\varphi_i a^+)}{1 + (\frac{\lambda}{D_h})\varphi_i sinh(\varphi_i a^+)}\right) \tag{6.8}$$

and the eigenvalues φ_k are evaluated solving the following transcendental equation:

$$cot(\varphi_k b^+) = \frac{\lambda}{D_h}\varphi_k \tag{6.9}$$

When there is no rotation, i.e. $\omega = 0$, the modified pressure p^* is equal to the pressure p. Thus, for a non-rotating microchannel, the above equation corresponds to the exact analytical solution of a fully developed laminar flow of liquid in a rectangular duct with slip boundary conditions at the wall.

6.3 Numerical Solution Method

The numerical solution method is the same as mentioned in Section 5.3. As the implementation of slip boundary condition requires special attention, it is described in the following subsection.

6.3.1 Treatment of the Velocity Slip and Temperature Jump Boundary Conditions

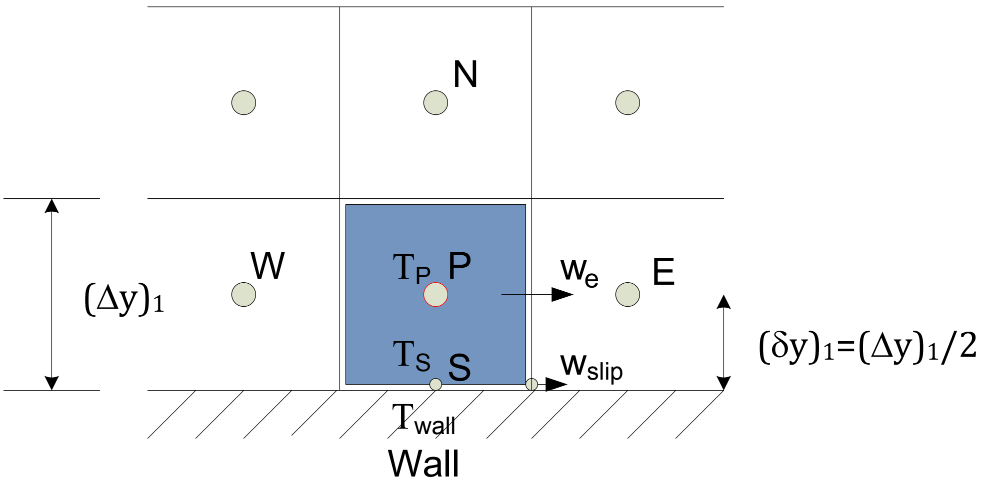

Figure 6.2: A two-dimensional control volume adjacent to the solid boundary

The implementation of the velocity slip and temperature jump boundary conditions in the present study is similar to the technique described by Hettiarachchi et al. [97] for gas microflows with the Knudsen number (Kn) replaced by the slip length (λ). Figure 6.2 shows two dimensional control volumes adjacent to the solid boundary in yz plane. The node under consideration is P and the neighboring west, east, south and north nodes are denoted by W, E, S and N respectively. The size of each control volume in y-direction is Δy and the distance between each node in y-direction i.e. the diffusion length is δy. For a boundary control volume the diffusion length is half of the length of the control volume i.e. $(\delta y)_1 = (\Delta y)_1/2$. The scalar variables such as temperature (T) and pressure (p) are calculated at the cell center whereas the velocities are calculated in control volume faces. If we discretize the velocity gradient in Equation 6.1 with a first order Taylor's series expansion, then we get the following expression,

$$w_{slip} = \lambda \frac{w_e - w_{slip}}{(\delta y)_1} \tag{6.10}$$

where w_e is the fluid velocity at the center of the east face of the control volume. After rearranging, the following relationship among the slip velocity (w_{slip}) and the east face velocity (w_e) can be obtained:

$$w_{slip} = \left(\frac{\lambda/(\delta y)_1}{1 + \lambda/(\delta y)_1} \right) w_e \tag{6.11}$$

Thus, in each iteration, the slip velocity at the wall changes with the velocity of the fluid at the adjacent node in a coupled manner. The temperature jump in Equation 6.2 can be treated in a similar fashion. A first order approximation of the normal temperature gradient results in the following relationship among the temperature values at nodes P, S and wall:

$$T_S - T_{wall} = l_k \left(\frac{T_P - T_S}{(\delta y)_1} \right) \tag{6.12}$$

Rearranging the above equation, T_S can be expressed as a function of the wall temperature T_{wall} and T_P, values of which are known after each iteration.

$$T_S = \frac{\frac{l_k}{(\delta y)_1} T_P + T_{wall}}{\left(1 + \frac{l_k}{(\delta y)_1}\right)} \tag{6.13}$$

Thus, the temperature of the fluid node adjacent to the boundary can be calculated using the above relationship. An alternative approach is to incorporate the temperature values in the coefficients of the discretized energy equation for boundary control volume as described in [97].

6.4 Grid Independence and Code Validation

Grid independence tests were performed to ensure that the numerical solution is reproducible. Due to the asymmetric pattern of fluid flow in a rotating channel, the whole domain was used for simulation. Table 6.2 presents the grid independence study of a laminar flow in a microchannel ($\alpha = 2.0$) rotating at 800 RPM with a slip length $\lambda = 1\,\mu\text{m}$. From Table 6.2, it can be observed that the percent differences among the results ($\frac{w_{max}}{w_{in}}, fRe, Nu_{avg}$) for $54 \times 27 \times 120$, $60 \times 30 \times 120$ and $60 \times 30 \times 130$ control volumes are very small. Considering the computational efficiency, the grid size $54 \times 27 \times 120$ was declared as grid independent and this grid size was used for all other subsequent simulations for $\alpha = 2.0$. For other aspect ratios, the number of control volumes in x and y directions were scaled accordingly.

The numerical code was tested against benchmark problems and the results were reproduced within certain accuracy. Table 6.3 demonstrates the results of a fully developed steady laminar flow through rectangular ducts with walls maintained at uniform temperature. The grid independent results e.g. the ratio of the centerline velocity to the inlet velocity ($\frac{w_{max}}{w_{in}}$), the product of the friction factor and Reynolds number (fRe) i.e. the Poiseuille number (Po) and the average Nusselt number (Nu_{avg}) for different aspect ratios were compared with the exact analytical results of Shah and London [98]. The fully developed velocity profiles for different aspect ratios are presented in Figure 6.3. It can be observed from Table 6.3 and Figure 6.3 that the present simulation results are in good agreement with the exact solutions given by Shah and London [98]. In order to verify the slip flow boundary condition, a simulation for water flowing through a $300\,\mu m \times 30\,\mu m$ microchannel was conducted with a slip length $\lambda = 1\,\mu m$. The test parameters are identical to the experiment performed by Tretheway and Meinhart [27], except that the microchannel length used in the simulation was 2 cm whereas in the actual experiment the length was 8 cm. Since the Reynolds number is very low ($\sim 0.34\,\mu m$) and the hydraulic diameter is very small ($\sim 54.54\,\mu m$) in this case, the hydrodynamic entrance length is also very small and a microchannel length of 2 cm is sufficient to compute the fully developed velocity profiles. The apparent slip length $\lambda = 1\,\mu m$ was determined experimentally which was about 10% of the free stream velocity [27]. Figure 6.4a shows the comparison of the velocity profiles in the vicinity of hydrophobic walls. Although the present simulation results slightly underpredict the experimental results, they are in excellent agreement with the analytical solution given in Equation 6.7 for the non-rotating case ($\omega = 0$). A simulation of water flow inside a microchannel with a hydrophilic surface was also performed using the same geometry and compared with the experimental results of [27] (Figure 6.4b). The experimentally measured slip length $\lambda = 0$ i.e. no slip boundary condition was used for the simulation. In this case, the simulation results slightly overpredict the experimentally measured velocity profile, but match almost exactly with the analytical solution of Shah and London [98]. The reported velocity error in the experimental measurement was within 2% and the uncertainty of the wall location i.e. slip length was approximately $0.45\,\mu m$ [27], and [99]. Considering the experimental uncertainty, it can be concluded that the developed code is working properly and producing realistic results. Further validation of steady laminar forced convection in a rotating square duct can be found in [36].

Table 6.2: Grid independence study for a laminar flow in a microchannel rotating at 800 RPM with a slip length $\lambda = 1.0\,\mu\text{m}$ and aspect ratio $\alpha = 2.0$

Grid Size (CV)	$\frac{w_{max}}{w_{in}}$	% Diff	fRe	% Diff	Nu_{avg} (bottom wall)	% Diff
20 × 10 × 20	1.906	-	14.449	-	6.067	-
24 × 12 × 40	1.921	0.781	14.586	0.939	5.962	1.761
30 × 15 × 60	1.940	0.979	14.706	0.816	5.863	1.689
40 × 20 × 80	1.942	0.103	14.806	0.675	5.797	1.138
50 × 25 × 100	1.949	0.359	14.854	0.323	5.786	0.190
54 × 27 × 120	1.949	0.010	14.877	0.155	5.759	0.469
60 × 30 × 120	1.949	0.005	14.880	0.020	5.795	0.621
60 × 30 × 130	1.949	0.000	14.880	0.001	5.797	0.034

Table 6.3: Comparison of normalized maximum velocities, friction factors, and Nusselt numbers for fully developed laminar flow in rectangular channels with Shah and London [98]

Aspect Ratio, α	1.0	2.0	4.0	10.0	20.0
$\frac{w_{max}}{w_{in}}$, Present Simulation	2.092	1.986	1.764	1.592	1.539
$\frac{w_{max}}{w_{in}}$, Exact Solution [98]	2.096	1.992	1.774	1.601	1.552
fRe, Present Simulation	14.17	15.46	18.11	20.93	22.21
fRe, Exact Solution [98]	14.23	15.55	18.23	21.17	22.48
$C_f Re$, Present Simulation	58.11	63.13	73.20	84.24	89.34
$C_f Re$, Exact Solution [98]	56.91	62.19	72.93	84.68	89.92
Nu_{avg}, Present Simulation	3.01	3.48	4.62	6.09	6.78
Nu_{avg}, Exact Solution [98]	2.98	3.39	4.44	5.91	6.65

6.5 Results and Discussions

The key parameters that affect the velocity and temperature variables in this study are the centrifugal force and the Coriolis force and the discontinuity of the variables at the solid boundary i.e. the velocity slip and the temperature jump. The effect of rotation was investigated by varying the rotational frequency ω ($0\,\text{RPM} - 3{,}200\,\text{RPM}$). The effect of liquid slip was studied by varying the slip length λ ($0\,\mu\text{m} - 10\,\mu\text{m}$).

6.5.1 Velocity Profiles

Figure 6.5 shows the surface plot of the velocity magnitude at the channel outlet for a rotating frequency $\omega = 2{,}800\,\text{RPM}$ and channel aspect ratio $\alpha = 2.0$. With the slip boundary condition, clear slip is visible at the channel walls, the extent of

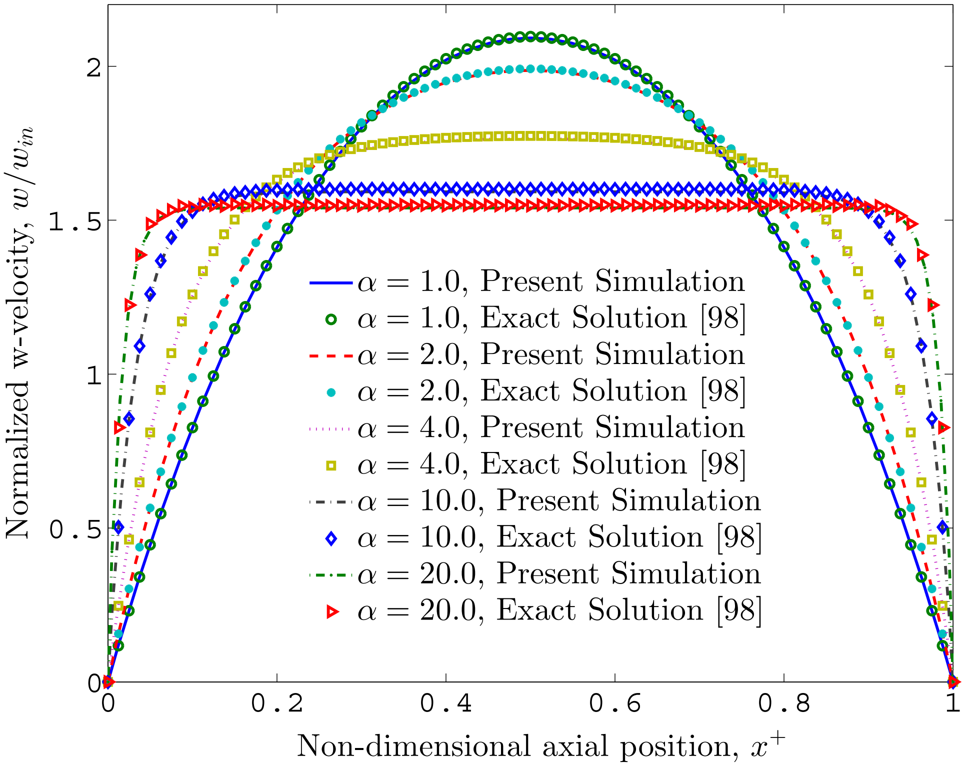

Figure 6.3: Velocity profiles of fully developed laminar channel flow for different aspect ratios with no slip boundary condition. The simulation results are compared with the analytical solution of Shah and London [98]

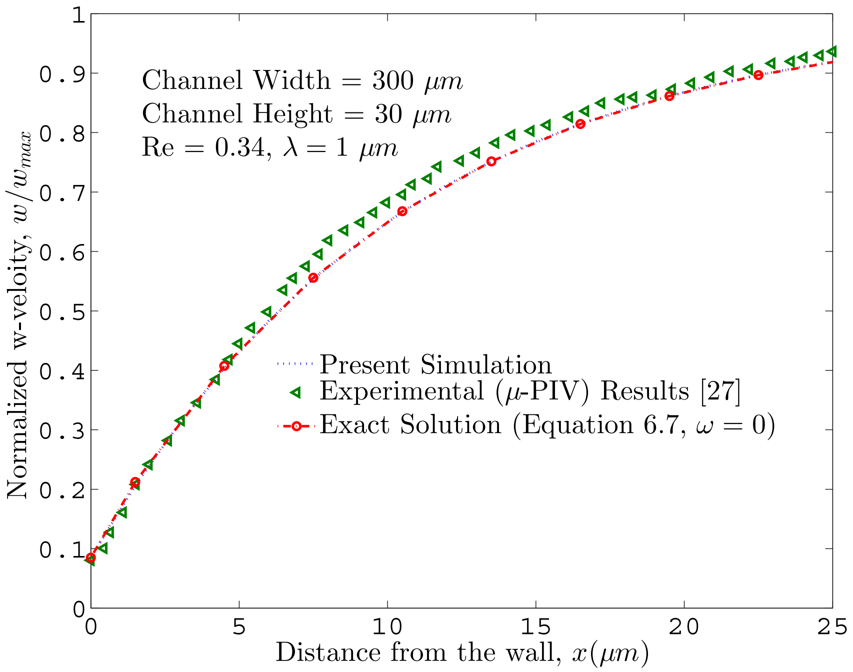

(a) hydrophobic surface

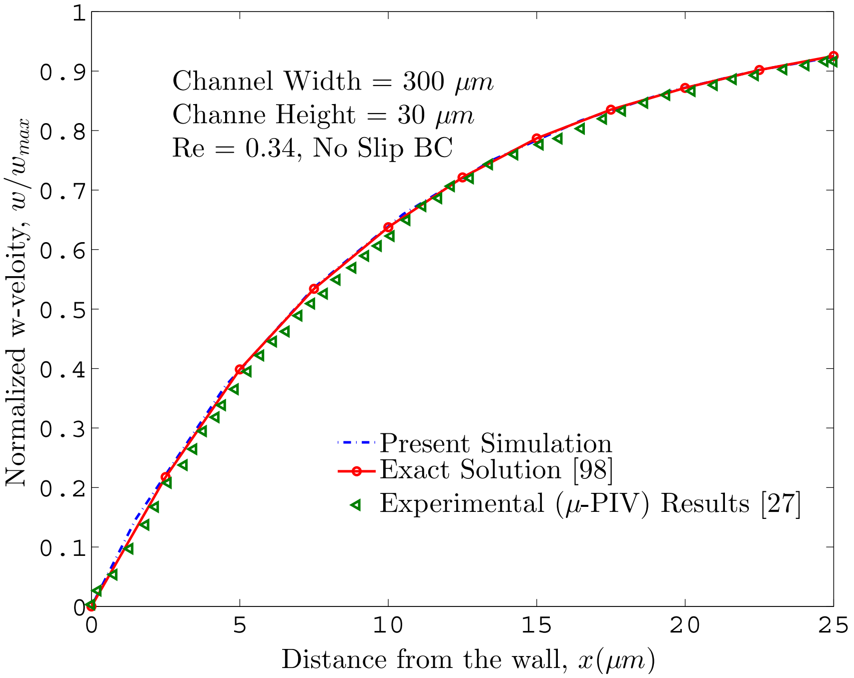

(b) hydrophilic surface

Figure 6.4: Comparison of velocity profiles with the experimental results of Tretheway and Meinhart [27]

which depends on the value of the slip length, λ. For a particular cross-section of the microchannel, the slip velocity varies in a parabolic manner along the periphery with a minimum value at the corner region and a maximum value near the center of the wall region. A similar observation was reported by Hettiarachchi et al. [97] and Renksizbulut et al. [100] in their studies of rarefied gas slip flow in non-rotating rectangular microchannels. However, due to the rotational effect, the slip velocity along the x-axis is asymmetric as opposed to the symmetric slip velocity for a non-rotating channel. Figure 6.6a shows the comparison of normalized w-velocity profiles at y-midplane ($y = b/2$) of channel outlet for different slip length and for $\omega = 2400$ RPM. Because of the Coriolis force, the velocity profiles in the rotating microchannel are skewed to the left. As a result, the velocity gradient at the left wall is greater than the velocity gradient at the right wall. Since the slip velocity is directly proportional to the normal velocity gradient at the wall, the slip velocity at the left wall becomes higher than the slip velocity at the right wall, which can be clearly observed from Figure 6.6a. As the slip length increases, the slip velocity also increases, but the magnitude of the maximum velocity decreases and the location of the maximum velocity shifts to the right. Thus, the velocity profile becomes more uniform or flattened when fluid slip occurs as compared to the velocity profile with no slip boundary condition. The trend becomes more prominent for higher values of slip length. This is due to the overall mass conservation inside the channel. The normalized w-velocity profiles along y at x-midplane ($x = a/2$) for $\omega = 2{,}400\,\mathrm{RPM}$ is shown in Figure 6.6b. By inspecting the figure, it can be seen that the velocity profiles are symmetric with respect to the mid-line $y = b/2$, because the Coriolis force acts only in the x-direction. For the same reason, the slip velocities at the bottom ($y = 0$) and top walls ($y = b$) are identical.

Figure 6.7a presents the outlet u-velocity profiles along x at y-midplane ($y =$

$b/2$) and Figure 6.7b presents the outlet v-velocity profiles along y at x-midplane ($x = a/2$). The velocities are normalized by using the inlet velocity, w_{in}. As the Coriolis force acts along x-direction, strong secondary flow effect can be observed from Figure 6.7a. The effect of secondary flow is less prominent in y-direction as can be seen from Figure 6.7b. For example, at a rotating frequency of 2,400 RPM with no-slip boundary condition, the maximum value of u-velocity is about 10% of the inlet velocity whereas the maximum value of v-velocity is about 1% of the inlet velocity. As the slip length is increased, the secondary flow effect decreases and both the u-velocity and v-velocity decrease in magnitude. The reason is following. With the increase in slip length, the w-velocity gets more flattened and the maximum of w-velocity decreases as it was observed from Figure 6.6a. Since the Coriolis force, f_c is directly proportional to the w-velocity, an increase in the slip length results in a decrease in the maximum value of the Coriolis force which in turn decreases the secondary flow effects.

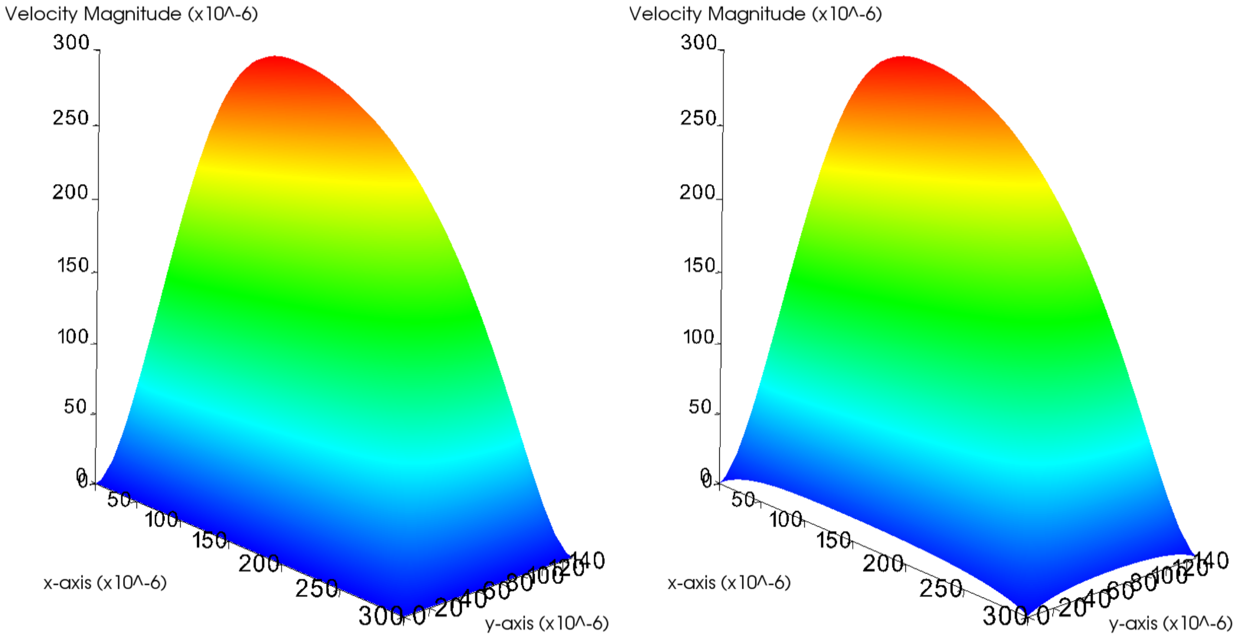

(a) No slip, $\lambda = 0\,\mu\text{m}$

(b) $\lambda = 2\,\mu\text{m}$

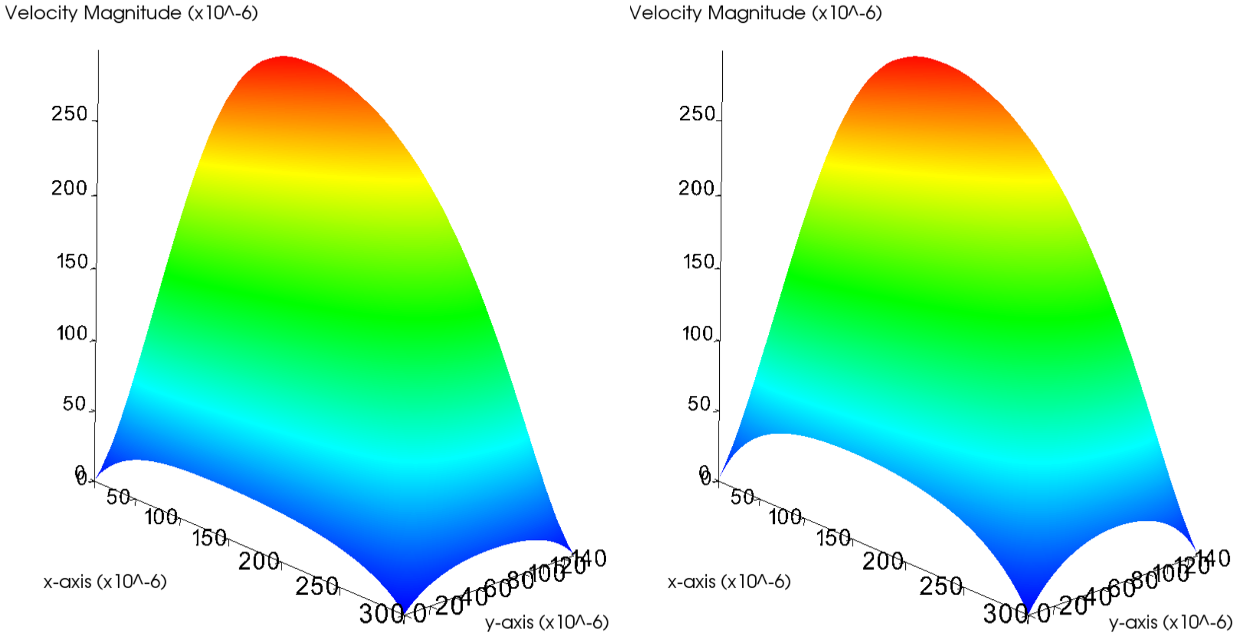

(c) $\lambda = 5\,\mu\text{m}$

(d) $\lambda = 10\,\mu\text{m}$

Figure 6.5: Velocity magnitude for different slip length λ ($\alpha = 2.0, \omega = 2,800$ RPM)

6.5.2 Slip Velocity

The effect of rotation on the slip velocity in a square microchannel is shown in Figure 6.8. When there is no rotation i.e. $\omega = 0$, for a fixed slip length, the slip velocities at all four walls of a square microchannel is the same due to the symmetric parabolic profile of a non-rotating channel flow. As the rotational speed is increased, the slip velocity at the left wall increases whereas the slip velocity at the right wall decreases for a fixed slip length. This is because, with the increase in rotational speed, the Coriolis force becomes stronger and hence the secondary flow effect becomes more dominant. The slip velocities at the top and bottom wall have the same values, because there is no rotational force acting in the y-direction and the w-velocity profile is symmetric along the y-axis. With the increase in rotational speed, the slip velocities at the top and bottom walls increase slightly. For a fixed rotational speed, the magnitude of the slip velocity increases with the increase in slip length.

6.5.3 Friction Factor

At a given cross-section of the microchannel, the friction factor f is calculated by taking the average along the periphery. The friction relation (fRe), also known as the Poiseuille number, is computed for different rotational speeds with varying slip length. First, we will examine the effect of rotation on the friction factor. Lei and Hsu [14] carried out a numerical simulation on flow through rotating straight pipes and showed that, for $Re_\omega > 1$, the ratio of friction factor for rotating pipe to the friction factor for non-rotating pipe asymptotically scales with $Re_\omega^{0.5}$. In the present study, similar behavior of the ratio, $(fRe)_{\lambda,Re_\omega}/(fRe)_{\lambda,Re_\omega=0}$ has been observed. Here, $(fRe)_{\lambda,Re_\omega=0}$ denotes the friction relation for a non-rotating microchannel with a specified slip length λ. Figure 6.9a presents the friction relation ratio scaled with

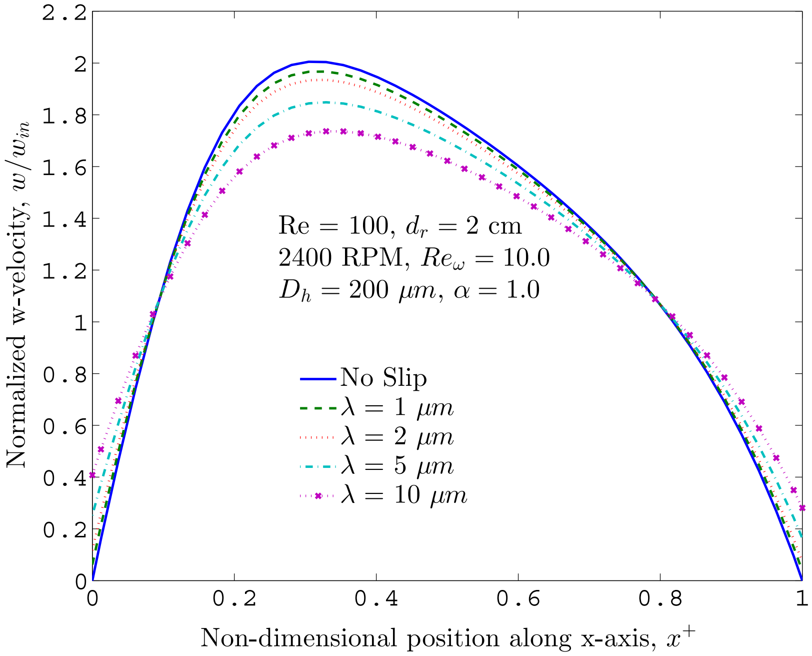

(a) w-velocity profiles along x

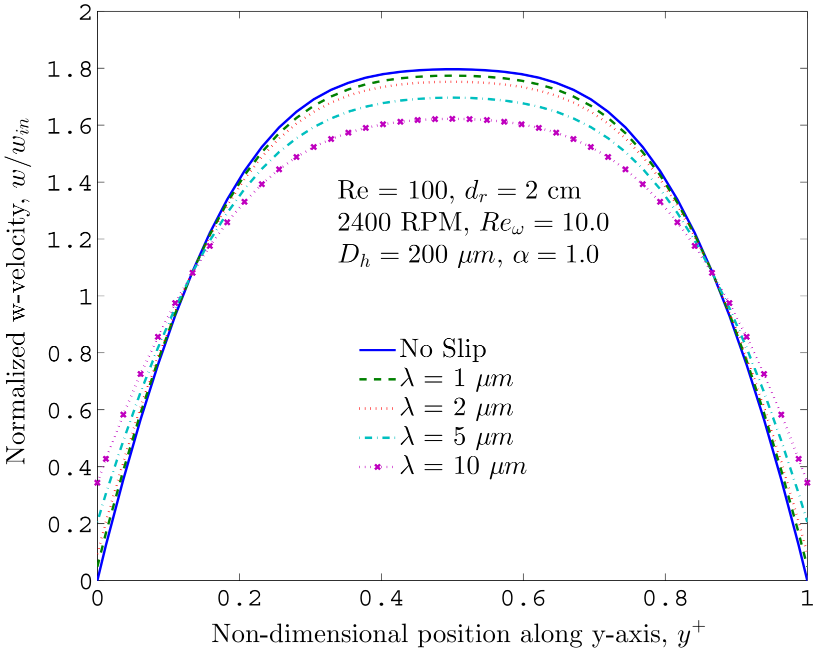

(b) w-velocity profiles along y

Figure 6.6: Comparison of w-velocity profiles at the channel exit for different slip lengths

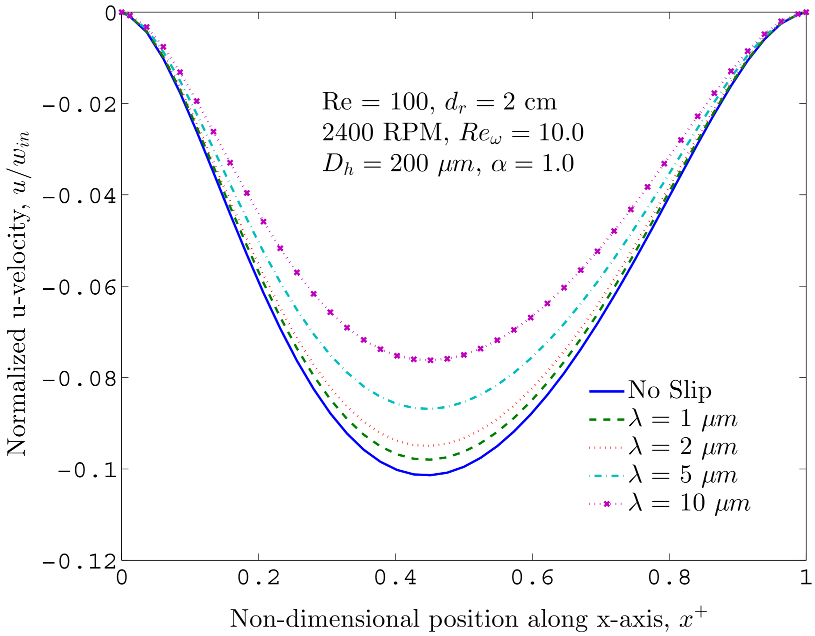

(a) u-velocity profiles along x

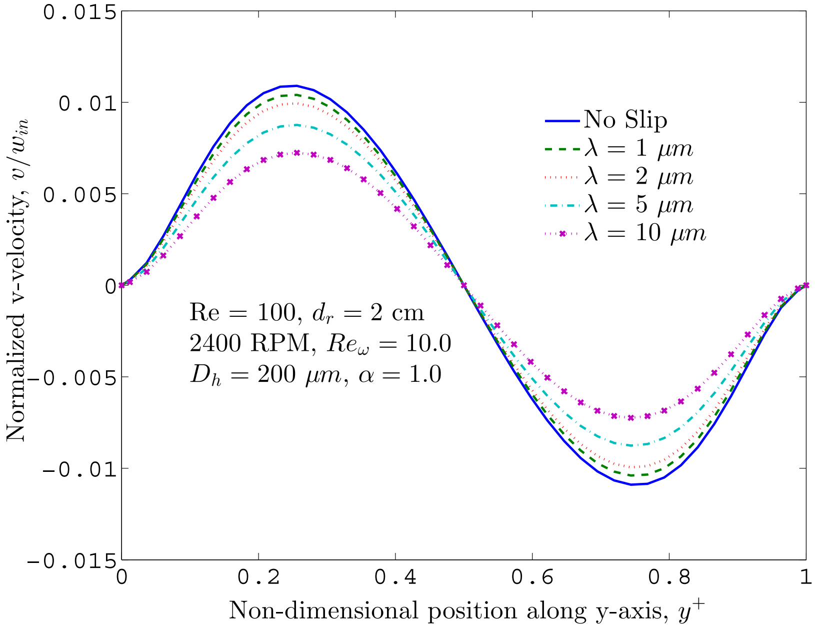

(b) v-velocity profiles along y

Figure 6.7: Comparison of secondary velocity profiles at the channel exit for different slip lengths

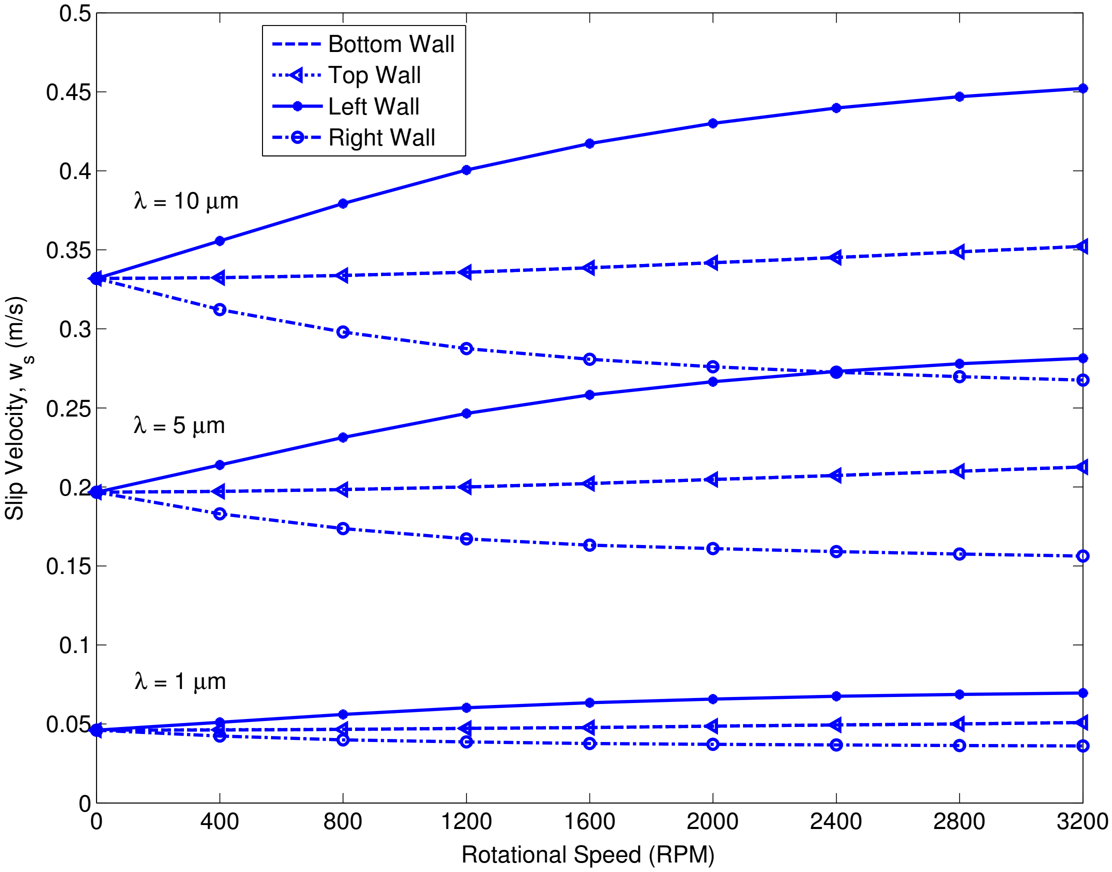

Figure 6.8: Variation of slip velocity with rotating frequency for $\alpha = 1.0$

$Re_\omega^{0.5}$ for a rotating square microchannel ($\alpha = 1.0$). The results agree well with the following correlations of friction factors for a rotating pipe flow given by Lei and Hsu (Equation 6.14) [14] and Ito and Nanbu (Equation 6.15) [101]:

$$Re_\omega^{-0.5}\frac{(fRe)_{\lambda=0,Re_\omega}}{(fRe)_{\lambda=0,Re_\omega=0}} \quad = \quad 0.9655Re_\omega^{-0.4368}, \quad for \quad 1 \quad \leq \quad Re_\omega \quad \leq \quad 12 \quad (6.14)$$

$$\frac{(fRe)_{\lambda=0,Re_\omega}}{(fRe)_{\lambda=0,Re_\omega=0}} = 0.0883(Re_\omega Re)^{1/4}\left[1 + 11.2(Re_\omega Re)^{-0.325}\right]$$
$$for \quad Re_\omega/Re < 0.5, 2.2\times10^2 < Re_\omega Re < 10^7 \quad (6.15)$$

From the Figure 6.9a, it can be seen that, for a fixed aspect ratio, the scaled friction factor is a function of both rotational Reynolds number and slip length. By using a multiple regression method, the following correlation for the scaled friction relation can be determined for $\alpha = 1.0$ with a coefficient of determination, $R^2 = 0.998$:

$$Re_\omega^{-0.5}\frac{(fRe)_{\lambda,Re_\omega}}{(fRe)_{\lambda,Re_\omega=0}} \quad = \quad \frac{0.9741Re_\omega^{-0.4374}}{\left[1+\left(\frac{\lambda}{D_h}\right)\right]^{0.779}}, \quad for \quad 1 \quad \leq \quad Re_\omega \quad \leq \quad 13.34 \quad (6.16)$$

Figure 6.9b shows the surface plot of the proposed correlation (Equation 6.16) along with the numerical results. Inspecting the plot, it can be concluded that the proposed correlation matches well with the numerical data. For no slip boundary condition, i.e. $\lambda = 0$, Equation 6.16 becomes almost identical to the correlation given by Lei and Hsu (Equation 6.14) [14].

Figure 6.10a shows the variation of $(fRe)_{\lambda=0,Re_\omega}/(fRe)_{\lambda,Re_\omega}$ with the nondimensional slip length (λ/D_h) as a function of rotational speed and aspect ratio. Here, $fRe_{\lambda=0,Re_\omega}$ is the friction relation for the no-slip boundary condition at a given rotational Reynolds number Re_ω. It can be noticed that, with a slip length of $10\mu m$, the friction factor can be reduced down to $28.5-36\%$ depending on the aspect ratio. It can also be observed that, for a fixed rotational speed and aspect ratio, the term $(fRe)_{\lambda=0,Re_\omega}/(fRe)_{\lambda,Re_\omega}$ varies linearly with the non-dimensional slip length (λ/D_h). Thus, for a given aspect ratio and rotational speed (or rotational Reynolds number), the ratio can be expressed as a linear function of λ/D_h in the following form:

$$\frac{(fRe)_{\lambda=0,Re_\omega}}{(fRe)_{\lambda,Re_\omega}} = 1 + C\left(\frac{\lambda}{D_h}\right) \tag{6.17}$$

Equation 6.17 is identical to the relationship between fRe and Kn given by Ebert and Sparrow [96] in their study of rarefied gas flow in rectangular ducts with slip boundary conditions. From Figure 6.10a, it can be observed that, the ratio of the friction relations is strongly dependent on the aspect ratio. For low aspect ratios ($\alpha = 1, 2$), the friction relation varies slightly with the rotational speed. As the aspect ratio increases ($\alpha = 4, 10, 20$), this variation in friction relation diminishes. Thus, for higher aspect ratio microchannel, the slope of the curve i.e. C is very weakly dependent on the rotational Reynolds number Re_ω.

From the numerical results of the present study, it is possible to calculate C using Equation 6.17 for different values of slip length and rotational speed. Figure 6.10b presents the variation of C as a function of aspect ratio for different rotational speeds. For a fixed rotational speed, a best fit curve can be generated to get the relationship between C and α. The correlation for these curves for a particular rotational speed can be expressed by the following formula:

$$C = p_1 + p_2\left(\frac{1}{\alpha}\right) + p_3\left(\frac{1}{\alpha^2}\right) + p_4\left(\frac{1}{\alpha^3}\right) \tag{6.18}$$

The coefficients of the above formula are tabulated in Table 6.4. Using equations 6.16, 6.17, and Table 6.4, the friction factor for all the cases considered in the present study can be calculated.

Table 6.4: Correlation coefficients for $C = p_1 + p_2\left(\frac{1}{\alpha}\right) + p_3\left(\frac{1}{\alpha^2}\right) + p_4\left(\frac{1}{\alpha^3}\right)$

Rotational speed, ω (RPM)	Rotational Reynolds number, Re_ω	p_1	p_2	p_3	p_4	Coefficient of determination, R^2
0	0.00	11.802	-9.722	7.847	-2.082	0.999
400	1.67	11.797	-9.632	7.461	-1.729	0.999
800	3.34	11.819	-9.500	7.029	-1.115	0.999
$1,200$	5.00	11.845	-10.152	9.543	-2.935	0.999
$1,600$	6.67	11.832	-9.751	8.933	-2.514	0.999
$2,000$	8.34	11.946	-10.937	12.850	-5.252	0.997
$2,400$	10.00	11.864	-10.445	12.853	-5.489	0.999
$2,800$	11.67	11.921	-10.910	14.623	-6.601	0.999
$3,200$	13.34	11.933	-10.149	12.490	-5.068	0.999

6.5.4 Nusselt Number

The Nusselt number (Nu) considered in this section refers to the average Nusselt number of the top and bottom wall based on the hydraulic diameter (D_h) of the microchannel. Figure 6.11 shows the variation of Nusselt number along the channel for different rotational speeds and a slip length $\lambda = 1\,\mu\text{m}$. At the channel entrance,

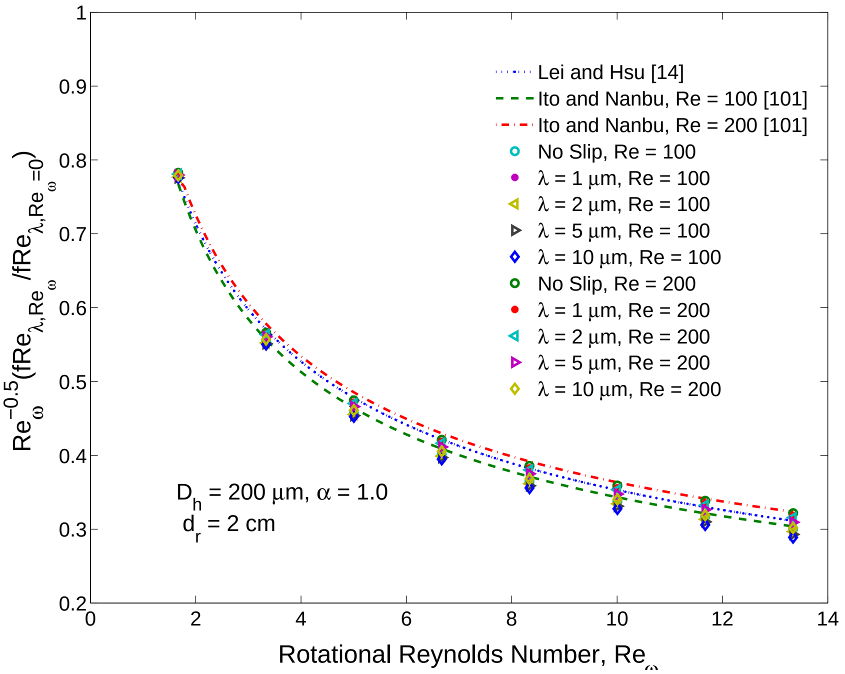

(a) Comparison with the existing correlations

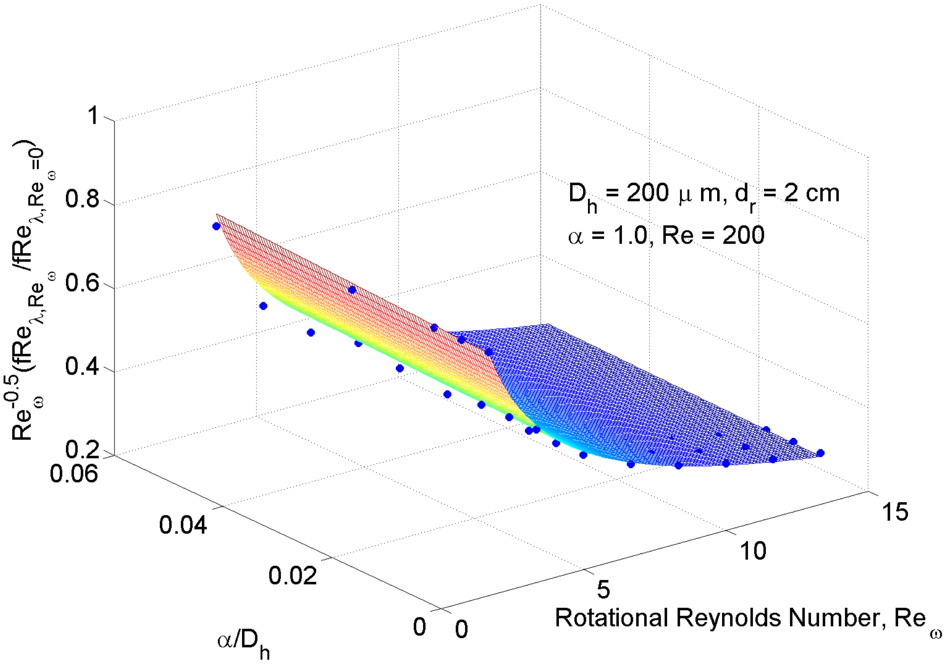

(b) Comparison of proposed correlation for fRe with the present numerical data

Figure 6.9: Variation of friction factor fRe with rotational Reynolds number Re_ω for $\alpha = 1.0$

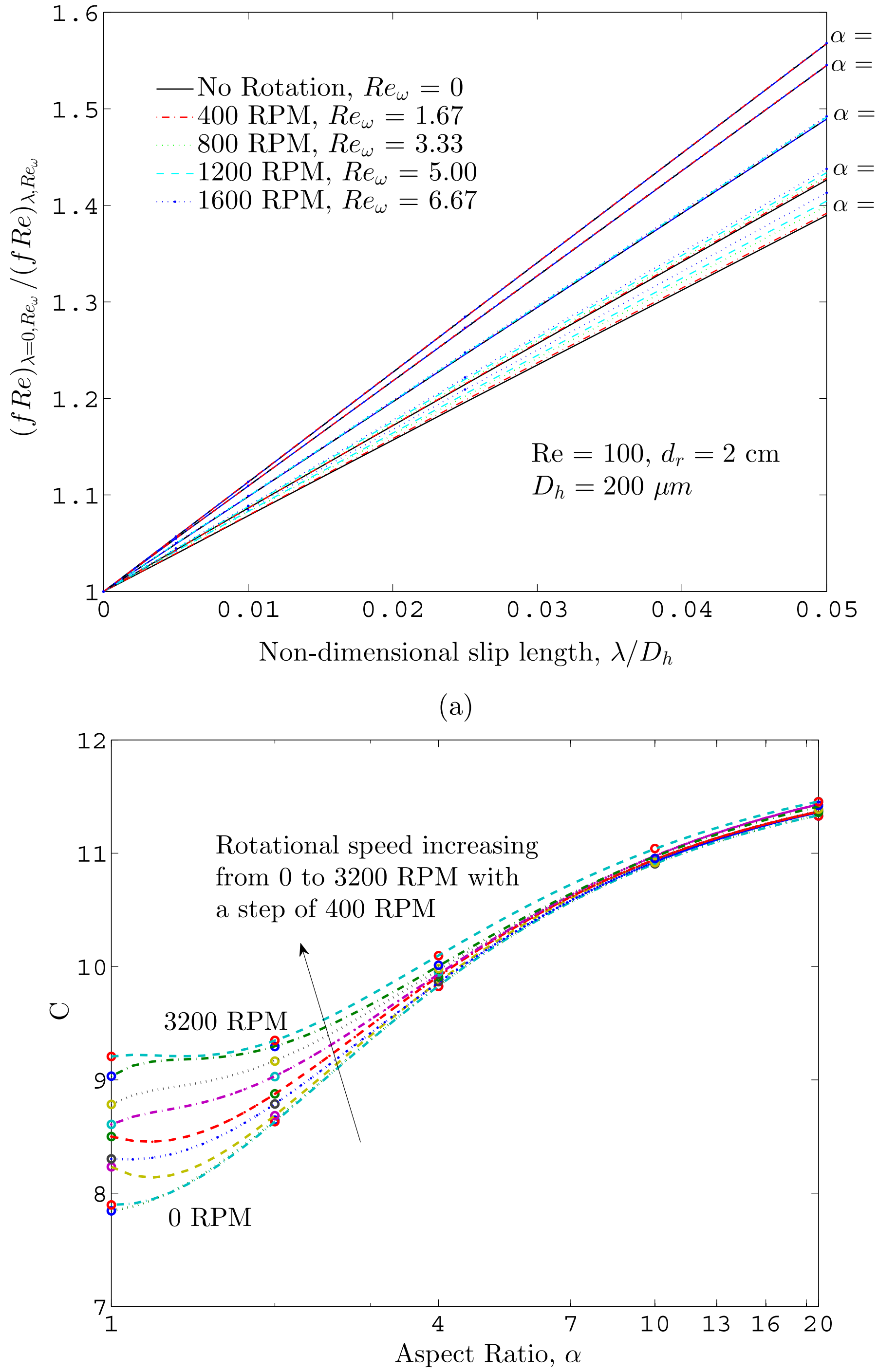

(a)

(b)

Figure 6.10: Poiseuille number fRe as a function of non-dimensional slip length λ/D_h, rotational Reynolds number Re_ω and aspect ratio α: (a) Variation of $(fRe)_{\lambda=0,Re_\omega}/(fRe)_{\lambda,Re_\omega}$ and (b) Correlations for C with α

the Nusselt number is high as large temperature gradient exists in the entry region. Close to the entry region, the flow is developing and the secondary flow is very small. As the flow develops, the secondary flow becomes stronger and an effective convective mixing occurs inside the channel due to the rotation. For this reason, the Nusselt number first attains a minimum value close to the entry region and as the flow progresses, it increases again to reach a fixed value near the channel exit. For a given cross-section, the Nusselt number increases with the increase in rotational speed due to the enhanced mixing originating from the secondary flow effects.

Figure 6.12 depicts the variation of Nusselt number along the channel as a function of slip length for different aspect ratios. The rotational speed considered in this case is 2,400 RPM ($Re_\omega = 10.0$). Again, it was observed that, for aspect ratios $\alpha = 1$ and 2, the Nusselt number increases after reaching a minimum value in the entry region due to the increase in temperature gradient near the channel walls. The mixed mean temperature of the liquid increases in this region and as the flow progresses, the difference between the wall temperature and liquid temperature diminishes. As a result, the Nusselt number reaches a maximum value and then decreases again. It was also observed that, for lower aspect ratios ($\alpha = 1 - 4$), as the slip length increases, the value of Nusselt number near the entrance region increases whereas it decreases near the exit region. This is because, within the entry region, the effect of rotation is small and thus, the slip velocity increases the convection process in the fluid particles adjacent to the walls. But, as the flow develops, the effect of rotation becomes stronger, and the flow is dominated by the secondary flow effects. In this region, increasing the slip length decreases the Coriolis effect, thereby decreasing the enhanced advection process resulting in a decreased value of Nusselt number. As the aspect ratio is increased ($\alpha = 10 - 20$), the effect of rotation decreases resulting in a decrease of secondary flow effects. As a result, the effect of the slip length gets stronger and increasing the slip length increases the Nusselt number even near the exit of the channel. Although for all the values of aspect ratio α, the rotational Reynolds number $Re_\omega = 10.0$ is fixed, the effect of rotation decreases with the increase in aspect ratio α. It indicates that, for channels of higher aspect ratios ($\alpha \geq 4$), the microchannel height b is a more suitable characteristic length than the hydraulic diameter D_h.

Figure 6.13a - 6.13e shows the variation of Nusselt number at the channel exit (Nu_{exit}) with varying rotational speed (ω) for $\alpha = 1 - 20$. For $\alpha = 1.0$ i.e. for a square microchannel, the fully developed Nusselt number of a non-rotating channel flow increases with the increase in slip length. When the rotation is introduced, this trend is reversed after approximately 300 RPM. Thus, for a secondary flow dominated region, the slip length has a diminishing effect on the Nusselt number. For $\alpha = 2.0$, the magnitude of Nusselt number at the channel exit is higher than that for $\alpha = 1.0$. In this case, the slippage of liquid enhances the Nusselt number at the channel exit, for up to 700 RPM. After that, it decreases the Nusselt number. For $\alpha = 4.0$, a similar effect can be observed around 1,450 RPM. For $\alpha = 10.0$ and $\alpha = 20.0$, the Nusselt number at the channel exit increases with the increase in slip length for the whole range of rotational speed (0 RPM $-$ 3,200 RPM).

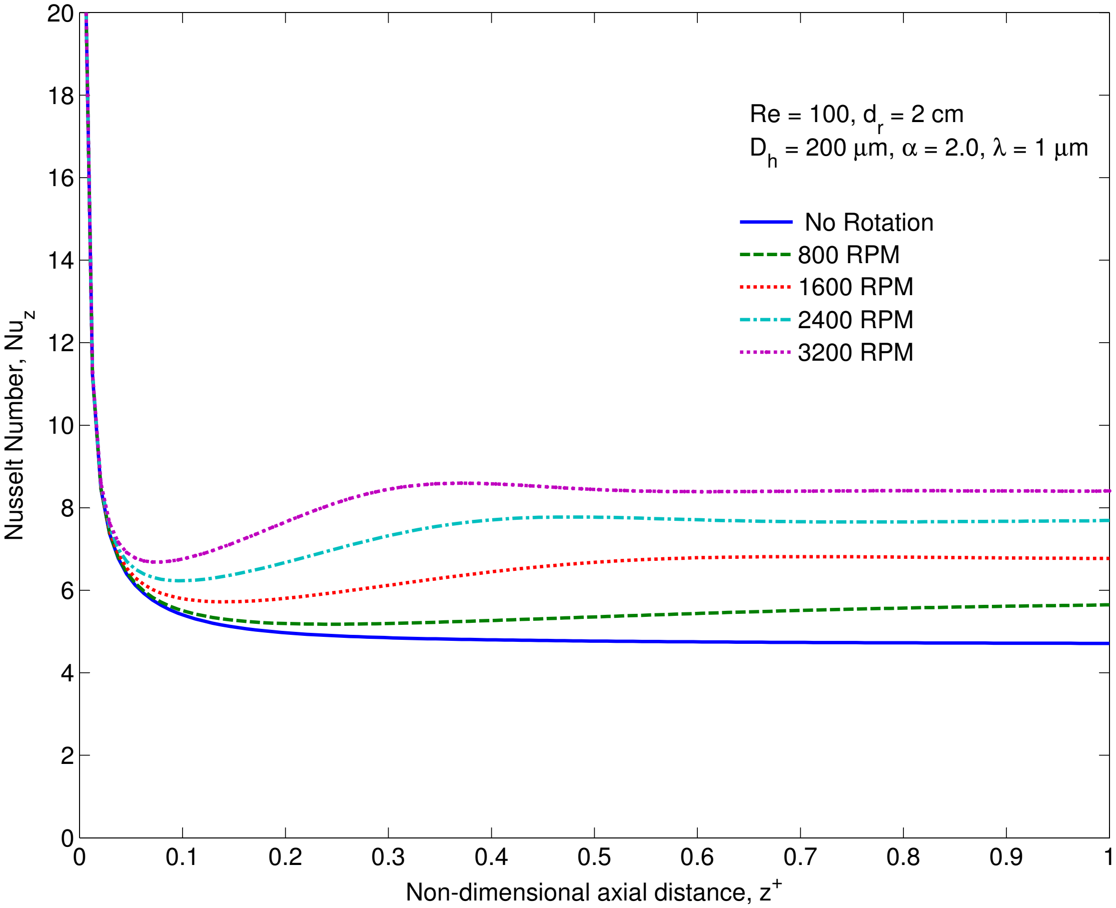

Figure 6.11: Variation of Nusselt number Nu along the channel for different rotational speeds ($\alpha = 2.0$)

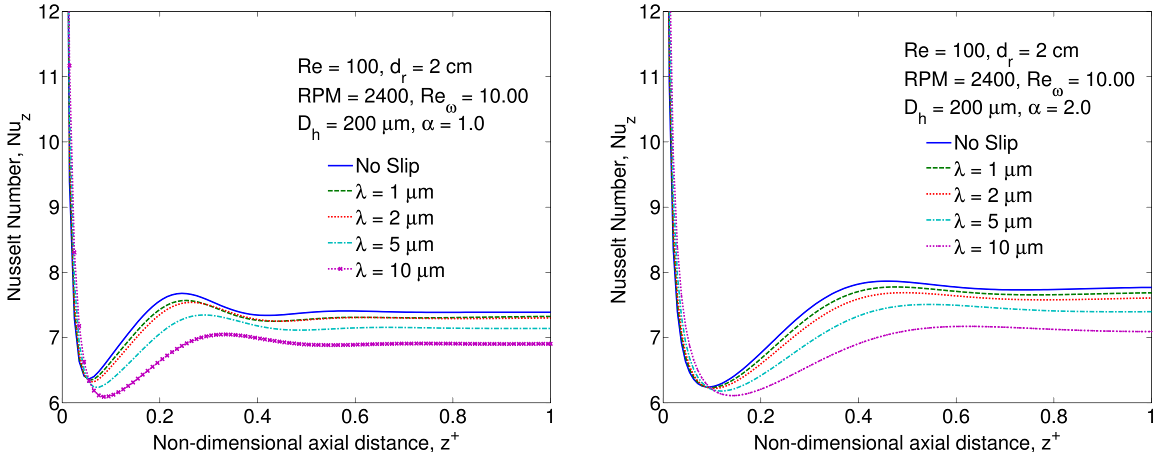

(a) $\alpha = 1.0$ (b) $\alpha = 2.0$

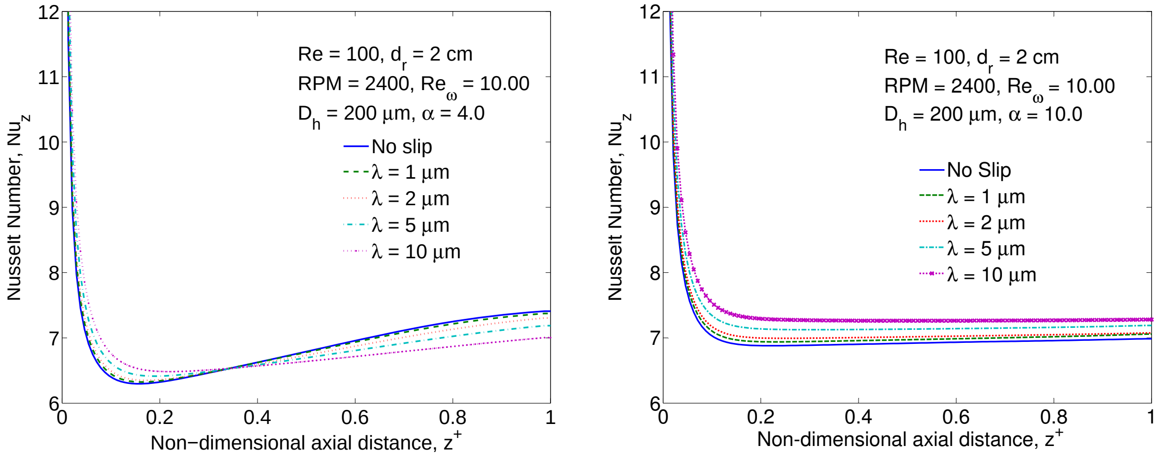

(c) $\alpha = 4.0$ (d) $\alpha = 10.0$

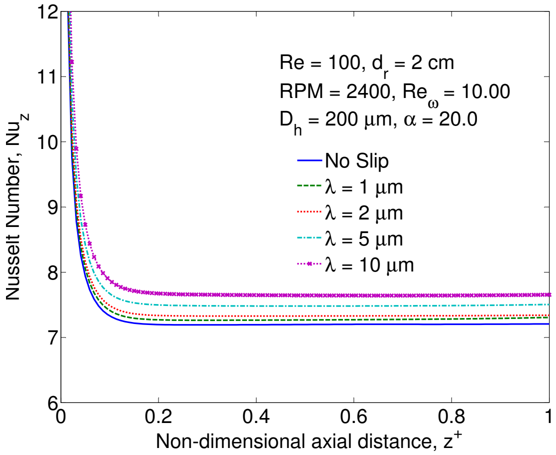

(e) $\alpha = 20.0$

Figure 6.12: Variation of Nusselt number along the channel for different slip lengths

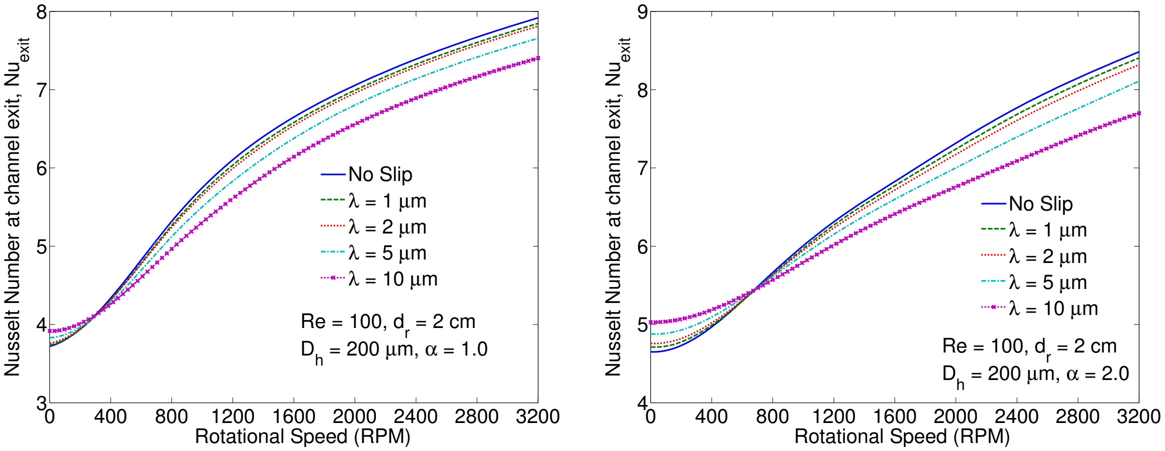

(a) $\alpha = 1.0$ (b) $\alpha = 2.0$

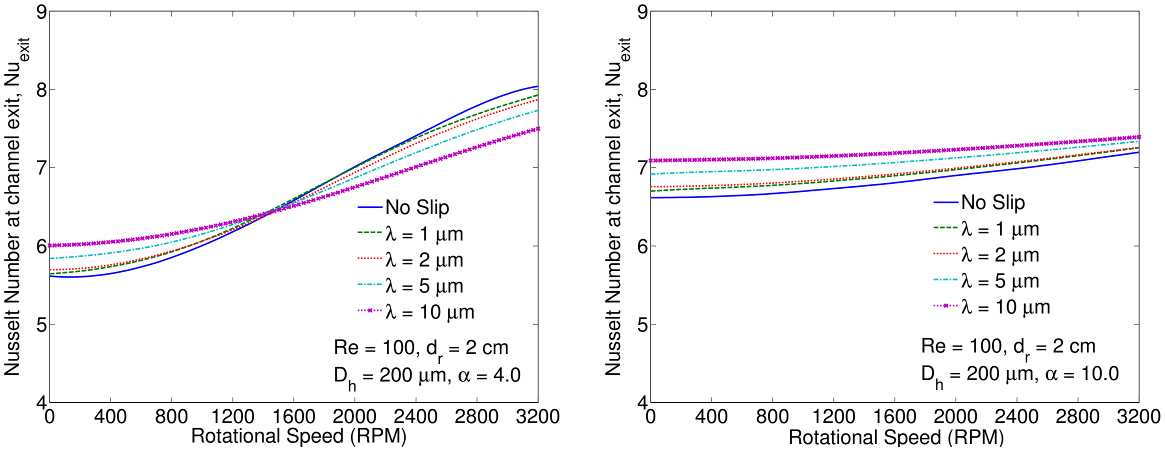

(c) $\alpha = 4.0$ (d) $\alpha = 10.0$

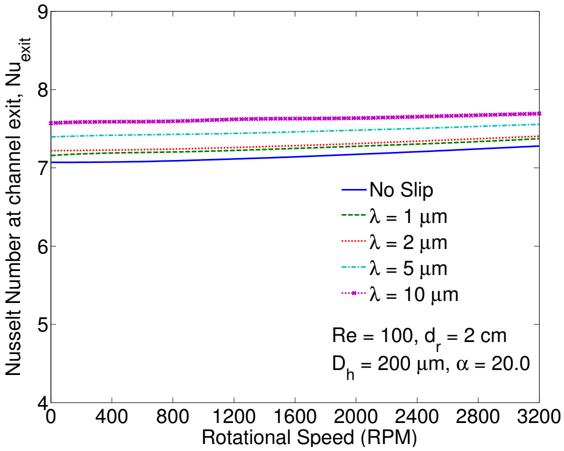

(e) $\alpha = 20.0$

Figure 6.13: Nusselt number at the channel exit as a function of rotational speed

6.6 Conclusions

A numerical investigation has been performed for flow and heat transfer of a Newtonian liquid inside rotating rectangular microchannels with slip boundary conditions. The steady, incompressible Navier-Stokes and energy equations were solved computationally by using a pressure based finite volume method. A thermally repeated boundary condition was applied to replicate the periodic arrangement of the radial microchannels. The findings of this study can be summarized as follows:

(i) For an orthogonally rotating microchannel, the slip velocity at the left wall is higher than that at the right wall, because of the induced Coriolis force in x-direction. However, the slip velocities at the bottom and top walls are identical, since there is no forcing term in the y-direction.

(ii) For a fixed rotational speed, as the slip length increases, the slip velocity increases, but the peak of the w-velocity decreases, which results in a more uniform w-velocity profile. This is due to the momentum balance inside the microchannel.

(iii) In the fully developed flow region of a low aspect ratio microchannel, the increase in slip length decreases the effect of the Coriolis force, thereby reducing the magnitude of u and v-velocities. In other words, the secondary flow diminishes as the slip length is increased.

(iv) Scaled friction relations were plotted against the rotational Reynolds number for different slip lengths and Reynolds numbers. Their values are in good agreement with the existing correlations with the no slip boundary condition. Based on the numerical data of the present study, a new correlation for calculating the friction factor as a function of rotational Reynolds number (Re_ω)

and non-dimensional slip length (λ/D_h) for a rotating square microchannel ($\alpha = 1.0$) has been proposed.

(v) For a given slip length and rotational speed, the friction relation (fRe) normalized to its no slip boundary condition counterpart varies linearly with the slip length. The slope of this line was expressed as a function of aspect ratio (α) and correlation coefficients were computed for the range of rotational speed considered in this study. A reduction of about $28.5 - 36\%$ in hydrodynamic resistance was observed using a slip length of 10 µm for $\alpha = 1.0 - 20.0$.

(vi) The rotational effect enhances the convective mixing in the liquid, thereby enhancing the Nusselt number. For low aspect ratio microchannel ($\alpha = 1 - 4$), the Nusselt number increases with the increase in slip length in the entry region. However, near the exit, the Nusselt number decreases with the slip length. As the aspect ratio is increased ($\alpha > 4$), the effect of rotation decreases, and the effect of slip length along the channel becomes more similar to the entry region.

7. SIMULATION OF TWO-PHASE FLOW: LEVEL SET METHOD

7.1 Introduction

Gas-liquid two-phase flow is a common occurrence in microchannels. In order to simulate the two-phase flow, an accurate representation of the interface between the two fluid region is necessary. There are a number of methods to accomplish this task and they can be divided into two groups based on the type of grids used: *(a) moving grid methods* and *(b) fixed grid methods* [102]. In moving grid methods, the interface is treated as a free surface boundary and the grid is reconstructed at each time step with the motion of the free surface. This way the interface location can be computed accurately without any smearing and the sharpness of the interface can be maintained [103]. However, when the interface goes under strong topological deformation during merging and fragmentation, maintaining the mesh quality to resolve the complex geometrical features is difficult. In addition, the stretching and distortion of the mesh results in a reduction of the accuracy of the overall solution. In fixed (Eulerian) grid methods, the evolution of the interface is computed in a fixed grid by defining an indicator function in the computational domain. The interface location can be identified using the values of the indicator function. Thus, the topological deformation can be handled easily in fixed grid methods and grid related problems encountered in moving grid methods can be avoided. However, the sharpness of the interface can not be maintained due to the smearing, which poses difficulties in computing the surface tension force accurately.

The two-phase flow simulation algorithms can also be divided into three categories depending on the numerical scheme used for computing the interface : *(a) Interface fitting methods, (b) Interface tracking methods* and *(c) Interface captur-*

ing methods. Interface fitting methods fall under the group of moving grid methods whereas interface tracking methods and interface capturing methods fall under the group of fixed grid methods. For a brief description of these methods the interested readers are referred to [104] and [105]. The level set method, first introduced by Osher and Sethian [38], is a type of interface capturing method. In this method, the interface between the two fluids is computed as an isocontour of a level set function. The first successful application of level set method to two phase flow problems was reported by Sussman et al. [106]. In this chapter we will describe the level set formulation and the numerical discretization technique. A number of example problems will be solved to show the effectiveness of the level set method in two-phase flow simulations.

7.2 Level Set Method

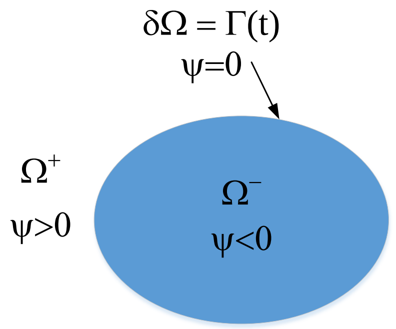

Figure 7.1: Level set function ψ defining the regions and boundary

A level function $\psi(\mathbf{x}, t)$ defining the two fluid regions and the interface is shown in Figure 7.1. The interface $\Gamma(t)$ is embedded in $\mathcal{R}^{ndim}$ defined by the zero isocontour of the level set function, where *ndim* is the dimension of the space. In this particular case shown in Figure 7.1, $ndim = 2$. The two fluid regions are separated by the implicit level set function as follows:

$$\psi(\mathbf{x}, t) > 0 \;\; for \;\; \mathbf{x} \in \Omega^+ \tag{7.1a}$$

$$\psi(\mathbf{x}, t) = 0 \;\; for \;\; \mathbf{x} \in \delta\Omega \tag{7.1b}$$

$$\psi(\mathbf{x}, t) < 0 \;\; for \;\; \mathbf{x} \in \Omega^- \tag{7.1c}$$

In particular, the level set function is expressed as a *signed distance function*, which is a special kind of implicit function. For a signed distance function $\psi(\mathbf{x})$, $|\psi(\mathbf{x})|$ implies the shortest distance from $\mathbf{x}$ to the interface location $\psi(\mathbf{x}) = 0$. In addition to having different signs at the opposite sides of the interface as described in Equation 7.1, it possesses the property that $|\nabla\psi| = 1$.

The fluid properties, such as density and viscosity can be computed from the value of the level set function:

$$\rho(\psi) = \rho_g + (\rho_l - \rho_g)H(\psi) \tag{7.2a}$$

$$\mu(\psi) = \mu_g + (\mu_l - \mu_g)H(\psi) \tag{7.2b}$$

where the subscripts '*l*' and '*g*' denote liquid and gas, respectively. The Heaviside function $H(\psi)$ is defined as follows:

$$H(\psi) = \begin{cases} 1 & \text{if } \psi < 0 \\ \frac{1}{2} & \text{if } \psi = 0 \\ 0 & \text{if } \psi > 0 \end{cases} \tag{7.3}$$

The derivatives of $\rho(\psi)$ with respect to t and x_i are:

$$\frac{\partial \rho}{\partial t} = (\rho_l - \rho_g)\frac{\partial H(\psi)}{\partial t} = (\rho_l - \rho_g)\frac{\partial H(\psi)}{\partial \psi}\frac{\partial \psi}{\partial t} = (\rho_l - \rho_g)\delta(\psi)\frac{\partial \psi}{\partial t} \tag{7.4}$$

$$\frac{\partial \rho}{\partial x_i} = (\rho_l - \rho_g)\frac{\partial H(\psi)}{\partial x_i} = (\rho_l - \rho_g)\frac{\partial H(\psi)}{\partial \psi}\frac{\partial \psi}{\partial x_i} = (\rho_l - \rho_g)\delta(\psi)\frac{\partial \psi}{\partial x_i} \tag{7.5}$$

where, the Dirac delta function $\delta(\psi)$ is defined as the derivative of the Heaviside function. Once the above relations are plugged into the continuity equation, we arrive at two equations: one is the divergence free velocity condition and the other is the evolution equation for the level set function $\psi(\mathbf{x}, t)$:

$$\frac{\partial \psi}{\partial t} + u_i \frac{\partial \psi}{\partial x_i} = 0 \tag{7.6}$$

The surface tension force is approximated using the continuum surface force (CSF) model introduced by Brackbill et al. [107]. In this model, the surface tension is assumed to be a volume or body force and the surface tension σ can be included in the momentum equations by using a Dirac delta function $\delta(\psi)$:

$$\rho\frac{\partial u_j}{\partial t} + \rho u_i \frac{\partial u_j}{\partial x_i} = -\frac{\partial p}{\partial x_j} + \mu\frac{\partial^2 u_j}{\partial x_i \partial x_i} + \rho S_j + f_{\sigma j}\delta(\psi) + F_{body} \tag{7.7}$$

Here, force due to surface tension is,

$$f_{\sigma j} = \sigma \kappa n_j \tag{7.8}$$

and the curvature of the interface is,

$$\kappa = -\nabla.\mathbf{n} = -\nabla.\frac{\nabla \psi}{|\nabla \psi|} \tag{7.9}$$

where **n** is the normal vector to the interface.

7.3 Numerical Discretization

The level set equation (Eq. 7.6) is numerically solved by using a higher order upwind scheme.

$$\left(\frac{\partial\psi}{\partial t}\right)_{i,j} + \left(u^+\psi_x^- + u^-\psi_x^+ + v^+\psi_y^- + v^-\psi_y^+\right) = 0 \tag{7.10}$$

$$u^+ = \max(u_{i,j}, 0),\ u^- = \min(u_{i,j}, 0) \tag{7.11}$$

$$v^+ = \max(v_{i,j}, 0),\ v^- = \min(v_{i,j}, 0) \tag{7.12}$$

Here, ψ_x^- is the backward difference operator for approximating ψ_x, ψ_y^+ is the forward difference operator for approximating ψ_y, and so on. A first order accurate upwind scheme can be used to compute the difference operators although the accuracy may not be sufficient to correctly resolve the interfacial features. The first order upwind scheme can be improved by using an essentially non-oscillatory (ENO) scheme introduced by Harten et al. [108]. The basic idea of the ENO scheme is to compute the numerical flux functions based on the local smoothness of the solution [109]. The ENO scheme can be further improved by using a combination of weighted ENO stencils. The weighted essentially non-oscillatory (WENO) scheme, proposed by Liu et al. [110], is as follows:

$$\psi_x^- = \varpi_1\psi_x^1 + \varpi_2\psi_x^2 + \varpi_3\psi_x^3 \tag{7.13}$$

Three possible 3rd order ENO stencils are:

$$\psi_x^1 = \frac{\gamma_1}{3} - \frac{7\gamma_2}{6} + \frac{11\gamma_3}{6} \tag{7.14a}$$

$$\psi_x^2 = -\frac{\gamma_2}{6} + \frac{5\gamma_3}{6} + \frac{\gamma_4}{3} \tag{7.14b}$$

$$\psi_x^3 = \frac{\gamma_3}{3} + \frac{5\gamma_4}{6} - \frac{\gamma_5}{6} \tag{7.14c}$$

Here,

$$\gamma_1 = \frac{\psi_{i-2,j} - \psi_{i-3,j}}{\Delta x} \tag{7.15a}$$

$$\gamma_2 = \frac{\psi_{i-1,j} - \psi_{i-2,j}}{\Delta x} \tag{7.15b}$$

$$\gamma_3 = \frac{\psi_{i,j} - \psi_{i-1,j}}{\Delta x} \tag{7.15c}$$

$$\gamma_4 = \frac{\psi_{i+1,j} - \psi_{i,j}}{\Delta x} \tag{7.15d}$$

$$\gamma_5 = \frac{\psi_{i+2,j} - \psi_{i+1,j}}{\Delta x} \tag{7.15e}$$

For ψ_x^+,

$$\gamma_1 = \frac{\psi_{i+3,j} - \psi_{i+2,j}}{\Delta x} \tag{7.16a}$$

$$\gamma_2 = \frac{\psi_{i+2,j} - \psi_{i+1,j}}{\Delta x} \tag{7.16b}$$

$$\gamma_3 = \frac{\psi_{i+1,j} - \psi_{i,j}}{\Delta x} \tag{7.16c}$$

$$\gamma_4 = \frac{\psi_{i,j} - \psi_{i-1,j}}{\Delta x} \tag{7.16d}$$

$$\gamma_5 = \frac{\psi_{i-1,j} - \psi_{i-2,j}}{\Delta x} \tag{7.16e}$$

The smoothness estimates are calculated as follows:

$$s_1 = \frac{13}{12}(\gamma_1 - 2\gamma_2 + \gamma_3)^2 + \frac{1}{4}(\gamma_1 - 4\gamma_2 + 3\gamma_3)^2 \tag{7.17a}$$
$$s_2 = \frac{13}{12}(\gamma_2 - 2\gamma_3 + \gamma_4)^2 + \frac{1}{4}(\gamma_2 - \gamma_4)^2 \tag{7.17b}$$
$$s_3 = \frac{13}{12}(\gamma_3 - 2\gamma_4 + \gamma_5)^2 + \frac{1}{4}(3\gamma_3 - 4\gamma_4 + \gamma_5)^2 \tag{7.17c}$$

The weights are given by:

$$\xi_1 = \frac{1}{10}\frac{1}{(\epsilon + s_1)^2}, \quad \varpi_1 = \frac{\xi_1}{\xi_1 + \xi_2 + \xi_3} \tag{7.18a}$$
$$\xi_2 = \frac{6}{10}\frac{1}{(\epsilon + s_2)^2}, \quad \varpi_2 = \frac{\xi_2}{\xi_1 + \xi_2 + \xi_3} \tag{7.18b}$$
$$\xi_3 = \frac{3}{10}\frac{1}{(\epsilon + s_3)^2}, \quad \varpi_3 = \frac{\xi_3}{\xi_1 + \xi_2 + \xi_3} \tag{7.18c}$$

with

$$\epsilon = 10^{-6}\max\{\gamma_1^2, \gamma_2^2, \gamma_3^2, \gamma_4^2, \gamma_5^2\} + 10^{-99} \tag{7.19}$$

Here, 10^{-99} term is added to avoid a division by zero while computing ξ_k.

In order to integrate the unsteady term in the level set equation, a total variation diminishing (TVD) Runge-Kutta method has been used [111]. The third order accurate TVD Runge-Kutta method is a combination of Euler explicit steps at different time intervals. It can be expressed as follows:

$$\psi^{(1)} = \psi^{(n)} - \Delta t.\mathbf{V}^{(n)}.\nabla\psi^{(n)} \tag{7.20a}$$
$$\psi^{(2)} = \frac{3}{4}\psi^{(n)} + \frac{1}{4}\psi^{(1)} - \frac{1}{4}\Delta t.\mathbf{V}^{(1)}.\nabla\psi^{(1)} \tag{7.20b}$$
$$\psi^{(n+1)} = \frac{1}{3}\psi^{(n)} + \frac{2}{3}\psi^{(2)} - \frac{2}{3}\Delta t.\mathbf{V}^{(2)}.\nabla\psi^{(2)} \tag{7.20c}$$

Ideally, the interface between the two fluids has a zero thickness and in practice, it can not be computed exactly using any standard numerical approximation. Therefore, the fluid properties are smoothed using a smeared-out Heaviside function, $H_\varepsilon(\psi)$:

$$H_\varepsilon(\psi) = \begin{cases} 1 & \text{if } \psi < -\varepsilon \\ \frac{1}{2}[1 + \frac{\psi}{\varepsilon} + \frac{1}{\pi} sin(\pi\psi/\varepsilon)] & \text{if } |\psi| \le \varepsilon \\ 0 & \text{if } \psi > \varepsilon \end{cases} \tag{7.21}$$

The smoothed or modified delta function $\delta_\varepsilon(\psi)$ is given by:

$$\delta_\varepsilon(\psi) = \frac{dH_\varepsilon(\psi)}{d\psi} = \begin{cases} \frac{1}{2\varepsilon}[1 + cos(\pi\psi/\varepsilon)] & \text{if } |\psi| \le \varepsilon \\ 0 & \text{if } otherwise \end{cases} \tag{7.22}$$

The smeared-out approximations of the Heaviside and delta functions improve the stability of the numerical scheme. Here, ε is a parameter that determines the extent or bandwidth of the numerical smearing. Typically, the value of the ε is taken equal to $0.5\Delta x - 1.5\Delta x$.

7.3.1 Reinitialization Method

Although initially $\psi(x,t)$ is defined as a signed distance function, it does not necessarily remain so during the advection process. In order to maintain the level set function as a signed distance function, reinitialization of $\psi(x,t)$ is performed by the following equation [106]:

$$\frac{\partial\psi}{\partial t} + sign(\psi_0)(|\nabla\psi| - 1) = 0 \tag{7.23}$$

Here,

$$sign(\psi_0) = \frac{\psi_0}{\sqrt{\psi_0^2 + (\Delta x)^2}} \tag{7.24}$$

and ψ_0 is the initial value of the level set function.

The reinitialization equation is also discretized using a higher order upwind scheme.

$$\left(\frac{\partial \psi}{\partial t}\right)_{i,j} + \big(\max(sign(\psi_0), 0)\nabla^+_{ij} + \min(sign(\psi_0), 0)\nabla^-_{ij}\big) = sign(\psi_0) \tag{7.25}$$

where,

$$\nabla^+_{ij} = [\max(\psi^-_x, 0)^2 + \min(\psi^+_x, 0)^2 + \max(\psi^-_y, 0)^2 + \min(\psi^+_y, 0)^2]^{1/2} \tag{7.26a}$$

$$\nabla^-_{ij} = [\min(\psi^-_x, 0)^2 + \max(\psi^+_x, 0)^2 + \min(\psi^-_y, 0)^2 + \max(\psi^+_y, 0)^2]^{1/2} \tag{7.26b}$$

7.3.2 Error Measurement

There are typically two ways to evaluate the error in the interface calculation with the level set method: (i) error in the level set function, and (ii) error in the volume enclosed by the interface (or area enclosed by the interface for two-dimensional problem). The error in ψ indicates how much the interface location derived from the solution of the level set equation differs from the actual location of the interface. Sussman and Fatemi [112] proposed the following formula to measure the error in the level set function:

$$E_\psi = \frac{1}{\mathcal{L}} \sum_{i,j} |H_\varepsilon(\psi_{exact}) - H_\varepsilon(\psi)| \Delta x \Delta y \tag{7.27}$$

Here, $\mathcal{L}$ is the perimeter enclosed by the interface of the exact level set function, ψ_{exact}. The volume error at any time can be defined as,

$$\mathcal{V}'(t) = \frac{\mathcal{V}(t)}{\mathcal{V}_0} \tag{7.28}$$

The volume of fluid can be estimated by the following formula:

$$\mathcal{V}(t) = \int_{\Omega} H_{\varepsilon}(\psi) d\mathcal{V} = \sum_{j=1}^{n} \sum_{i=1}^{m} (H_{\varepsilon}(\psi))_{i,j} \Delta x \Delta y \tag{7.29}$$

7.4 Test Cases

7.4.1 Motion with Prescribed Velocity

The accuracy and effectiveness of the level set code was first tested by solving the discretized level set equation with a prescribed velocity field, thus obviating the need for solving momentum equations. In these test cases, the initial zero isocontour of level set function undergoes complex topology changes due to the prescribed velocity field. One such test case is shown in Figure 7.2, where a circular interface is advected in a time-reversed non-uniform vorticity field. The steady flow test was first introduced by Bell et al. [113] and later extended to a time reversed problem by Leveque [114]. The velocity field is given by:

$$u(x, y, t) = -sin^2(\pi x) sin(2\pi y) cos(\pi t/\mathcal{T}) \tag{7.30a}$$

$$v(x, y, t) = sin^2(\pi y) sin(2\pi x) cos(\pi t/\mathcal{T}) \tag{7.30b}$$

The computational domain is a unit square and the circular interface with a radius of 0.15 is initially located at (0.5, 0.75). The swirling flow rotates around the center of the domain and satisfies u = v = 0 at the boundaries. Due to the strong vortical nature of the velocity field, the interface is stretched into long filament and eventually takes a spiral shape. Because of the time function $cos(\pi t/\mathcal{T})$, the flow slows down and reverses the direction at $t = \mathcal{T}/2$ such that the initial interface should be recovered at time $\mathcal{T}$ (refer to Figure 7.2). The extent of recovery would indicate the accuracy of the discretization schemes. Figure 7.2 presents the test for a grid size of 320×320. The distortion of the circular interface into a spiral shape can be observed in Figure 7.2b. Since a very fine grid is used in this case, the circular interface is almost fully recovered at time $\mathcal{T}$, as shown in Figure 7.2c. The area loss for different grid sizes are tabulated in Table 7.1. For a relatively coarser grid size of 160 × 160, the area loss is as high as 9.82 %. As the grid size is increased to 320 × 320, the area loss is minimized to less than 1 %. It implies that, for strong vortical flows, a very fine grid should be used to minimize the area or volume error in level set method. It also justifies the use of higher order upwind schemes (such as WENO-5) to discretize the level set equation.

Table 7.1: Area loss for circular interface placed in a time reversed single vortex field

Case	Grid Size	Area Loss (%)
1	160 × 160	9.82
2	320 × 320	0.376

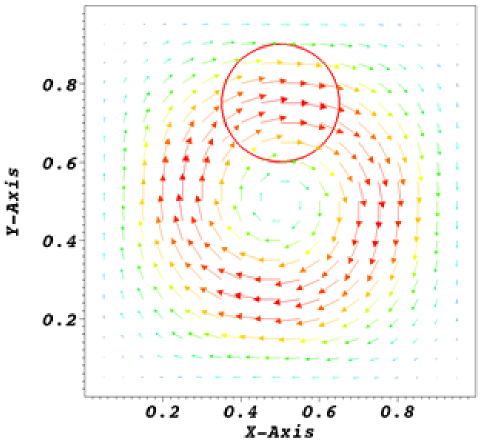

(a) $t = 0$

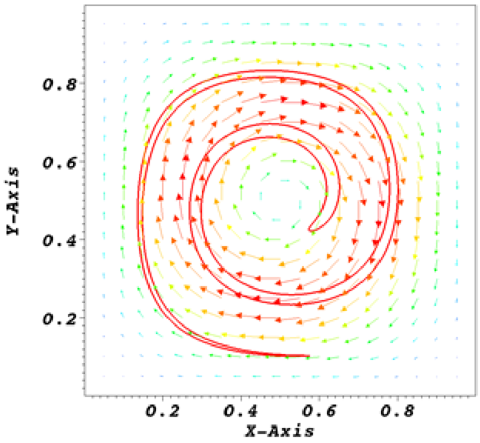

(b) $t = \mathcal{T}/2$

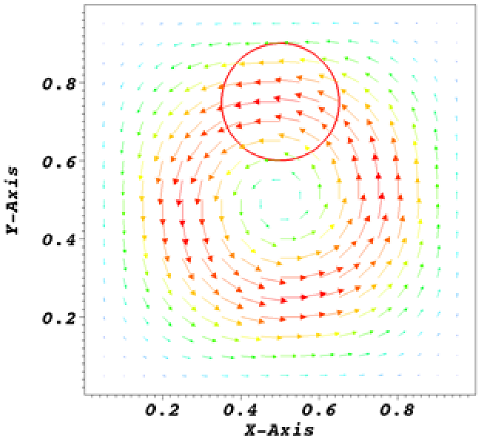

(c) $t = \mathcal{T}$

Figure 7.2: Circular interface in time reversed single vortex field.
Grid size = 320 × 320

7.4.2 Collapse of a Water Column

In this test case, a two-dimensional water column surrounded by air is kept in a $5\,\mathrm{m} \times 2\,\mathrm{m}$ domain. The water column dimension is $1\,\mathrm{m} \times 1\,\mathrm{m}$. The computational domain was divided with a grid size of 256×64 CVs. The properties of the fluids are presented in Table 7.2. The surface tension water (σ) is assumed to be 0.0728 Nm^{-1}. The simulation starts with a zero velocity inside both fluid regions. Although the wall is stationary i.e. it has a zero velocity, the interface in contact with the walls moves with a finite velocity. This poses a problem in specifying the velocity boundary conditions at the walls, which is commonly known as a moving contact line problem [115]. In this case, the problem was overcome by assuming a slip boundary condition on the free surface contact wall, which allows tangential slip along the wall surface while maintaining the non-permeability condition perpendicular to the wall surface. Mathematically, this condition can be represented by [116]:

$$\mathbf{V}.\mathbf{n} = 0 \tag{7.31}$$

$$\nabla\mathbf{V}.\mathbf{n} = 0 \tag{7.32}$$

With the start of the simulation, the water column breaks down due to the gravity and the water level height at the left wall decreases with time. Meanwhile, the water front gradually approaches the right wall. After hitting the right wall, the water splashes back and merges with itself forming cusps. Snapshots of water-air interface position at different times are shown in Figure 7.3. The variation non-dimensional front position and height as a function of time are plotted in Figure 7.4. The simulation results were compared with the experimental results of Martin and Moyce [117]. From Figure 7.4a, a slightly faster spread rate can be observed in the present simulation results as compared to the experimental results. This can be attributed to the contact angle (in this case $\theta_c = 90^o$) boundary condition of level set function. However, the water height position with time shows an excellent agreement with the experimental results, as can be observed from Figure 7.4b. It should be noted that, a conservative form of the momentum equations were used in the finite volume solver. A non-conservative form of the momentum equations can introduce errors in momentum transfer across the interface resulting in a non-physical spread rate of water in this case. This was demonstrated by Raessi and Pitsch [118] in their work on modeling interfacial flows with large density ratios using level set technique.

In addition, a 3D dam breaking simulation was conducted. The domain size is $0.4\,\mathrm{m} \times 0.1\,\mathrm{m} \times 0.1\,\mathrm{m}$. The water column size is $0.1\,\mathrm{m} \times 0.1\,\mathrm{m} \times 0.05\,\mathrm{m}$. The grid size is $240 \times 60 \times 60$ CVs. Figure 7.5 shows how the three-dimensional water column breaks under gravity and the water front propagates with time inside a closed container. Initially two-dimensional (2D) flow is observed when the front advances towards the right wall. After hitting the wall, the front splashes back and quickly forms three-dimensional (3D) breaking wave patterns. Similar observations were reported for a 3D dam breaking simulation by Yu [105].

Table 7.2: Properties of fluids for two phase flow problems

Fluid	Density ($kg\,m^{-3}$)	Dynamic Viscosity (Pa-s)	Thermal Conductivity ($Wm^{-1}K^{-1}$)	Specific Heat ($Jkg^{-1}K^{-1}$)	Prandtl Number
Water	997.0	8.71×10^{-4}	0.563	4179.0	6.46
Air	1.20	1.83×10^{-5}	0.0258	1005.0	0.712

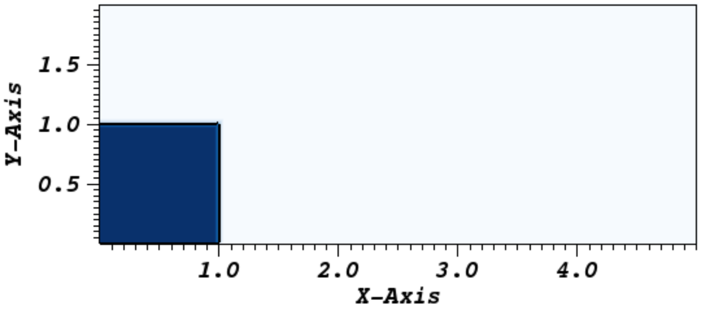

(a) t = 0.00 sec

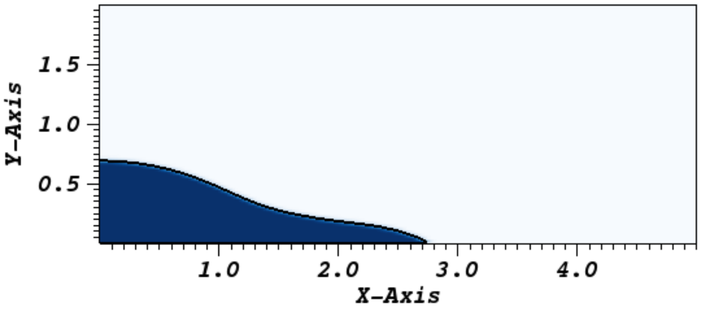

(b) t = 0.50 sec

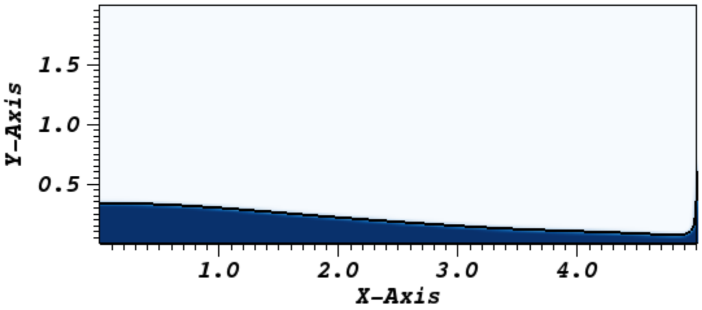

(c) t = 1.00 sec

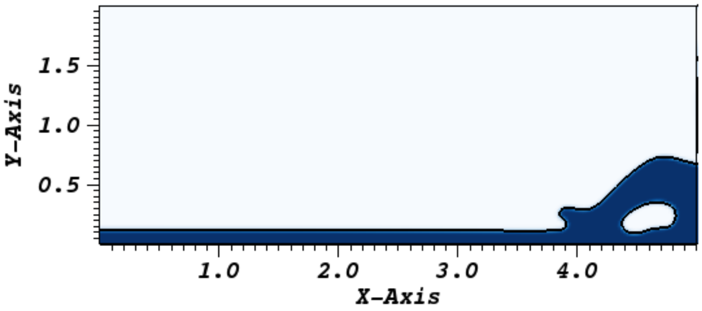

(d) t = 2.12 sec

Figure 7.3: 2D water column breaking under gravity, Grid size = 256 × 64 CVs

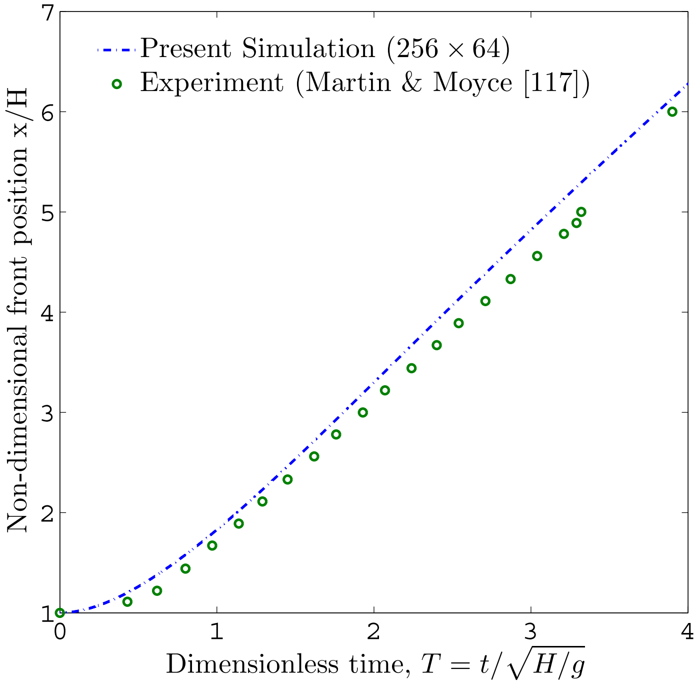

(a) Water front position with time

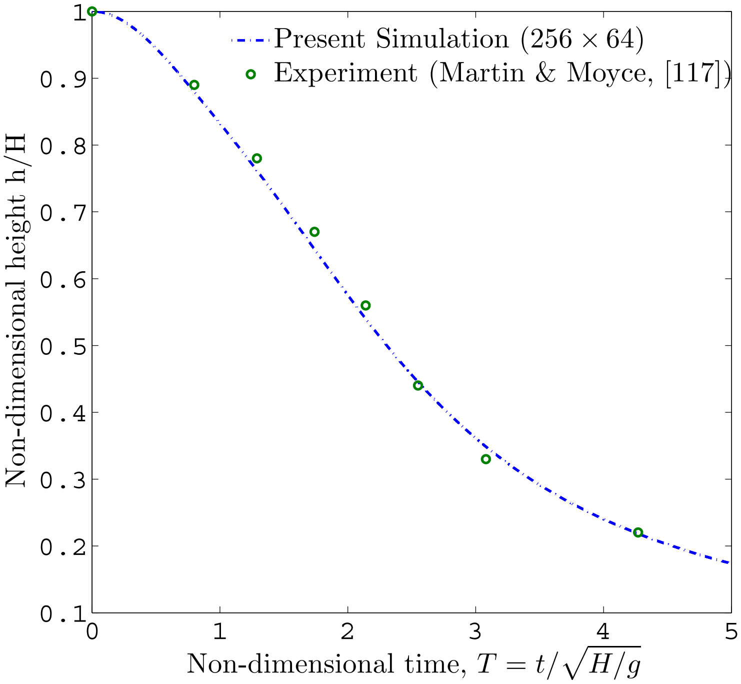

(b) Water height with time

Figure 7.4: Water front position and height as a function of time

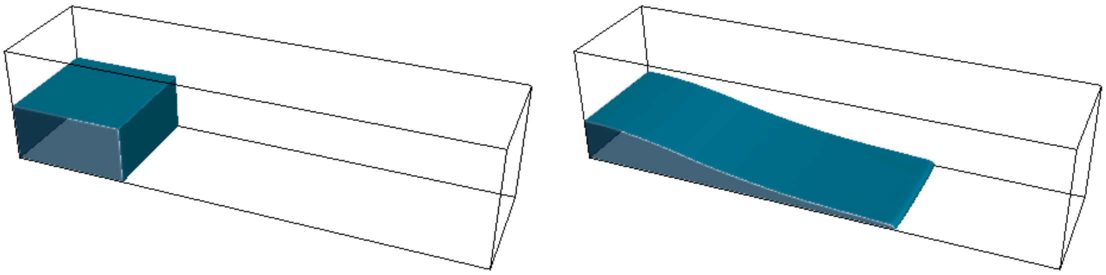

(a) t = 0.0 sec

(b) t = 0.2 sec

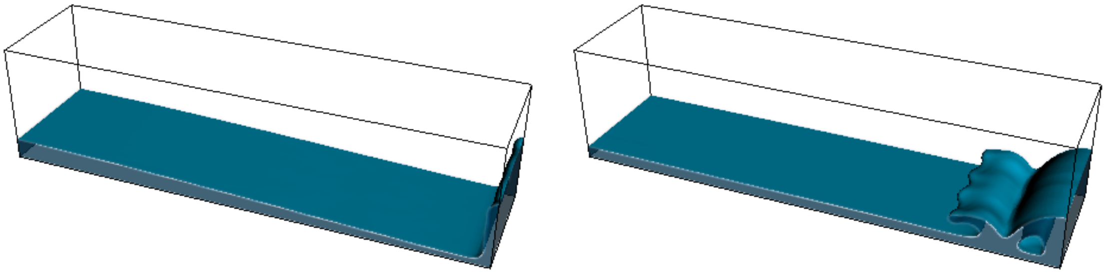

(c) t = 0.4 sec

(d) t = 0.6 sec

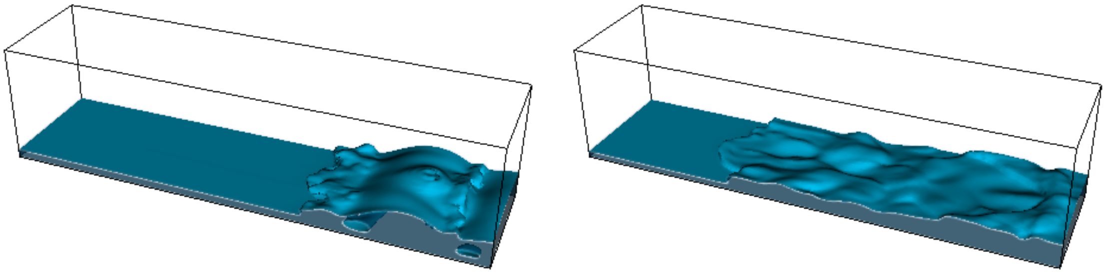

(e) t = 0.8 sec

(f) t = 1.0 sec

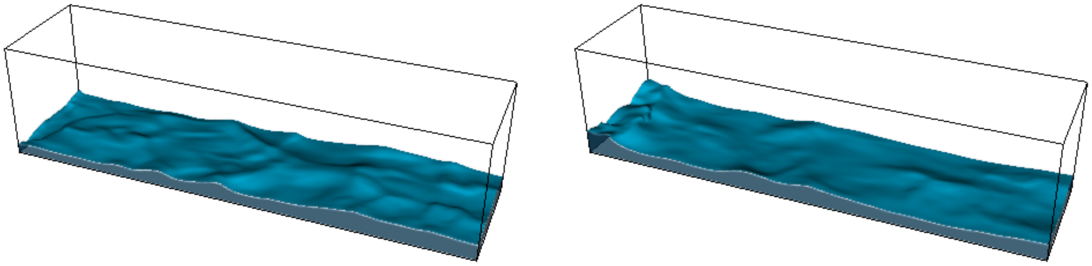

(g) t = 1.2 sec

(h) t = 1.4 sec

Figure 7.5: 3D water column collapsing under gravity, Domain size = 40 cm × 10 cm × 10 cm, Column size = 10 cm × 10 cm × 5 cm, Grid size = $240 \times 60 \times 60$ CVs

7.4.3 Droplet Splashing on Water Pool

In this problem a static circular water droplet is allowed to fall under gravity into a water pool. Numerical solution of this problem with a the level set method was first reported by Sussman et al. [106]. The present geometry is similar to the simulation conducted by Li et al. [119]. The domain size is 3 cm × 5 cm. The droplet radius is 3 mm, the water surface height is at 6*radius, and the droplet center is located at (1.5, 9*radius) position. A contact angle boundary condition has been used for the level set function at the solid walls. The properties of the air and water are the same as the collapsing of 2D water column problem, given in Table 7.2. The surface tension of water is 0.0728 Nm^{-1}. Figure 7.6 shows how the droplet falls under gravity and splashed into the water body. The merging of the droplet with the water surface is implicitly captured by the level set method without imposing explicit boundary conditions at the interface.

A 3D simulation of a water droplet splashing on a water body is shown in figure 7.7. The domain size is 3 cm × 3 cm × 4 cm and the grid size is 90 × 90 × 120 CVs. The droplet diameter is same as the 2D test case i.e. 6 mm. A reduction in droplet volume can be observed as the droplet falls under gravity and touches the water surface. This is due to the calculation of body force and surface tension force terms at the CV nodes. In order to avoid this problem, the external forces should be first calculated at the CV faces. Then, the cell-center or node values of the forces should be obtained by taking the area or volume weighted average of the face values. This is commonly known as the balanced force algorithm [120, 121]. A dramatic improvement in the volume or mass conservation enclosed by the interface was observed using the balanced force algorithm (not shown here).

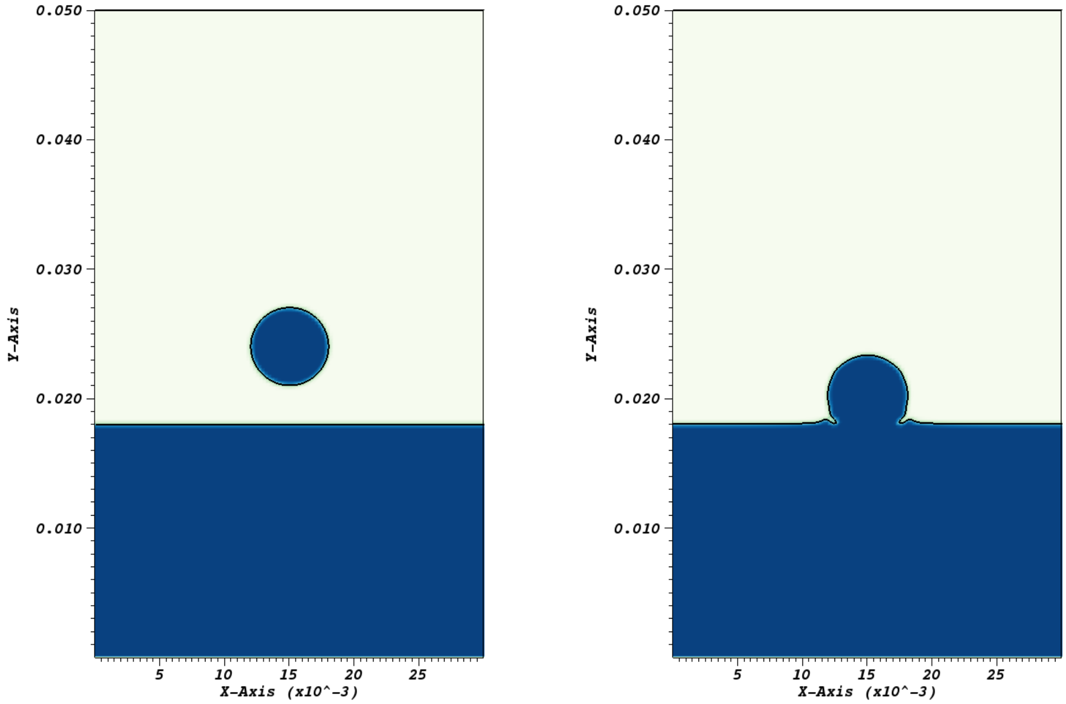

(a) time = 0.0 sec

(b) time = 0.0275 sec

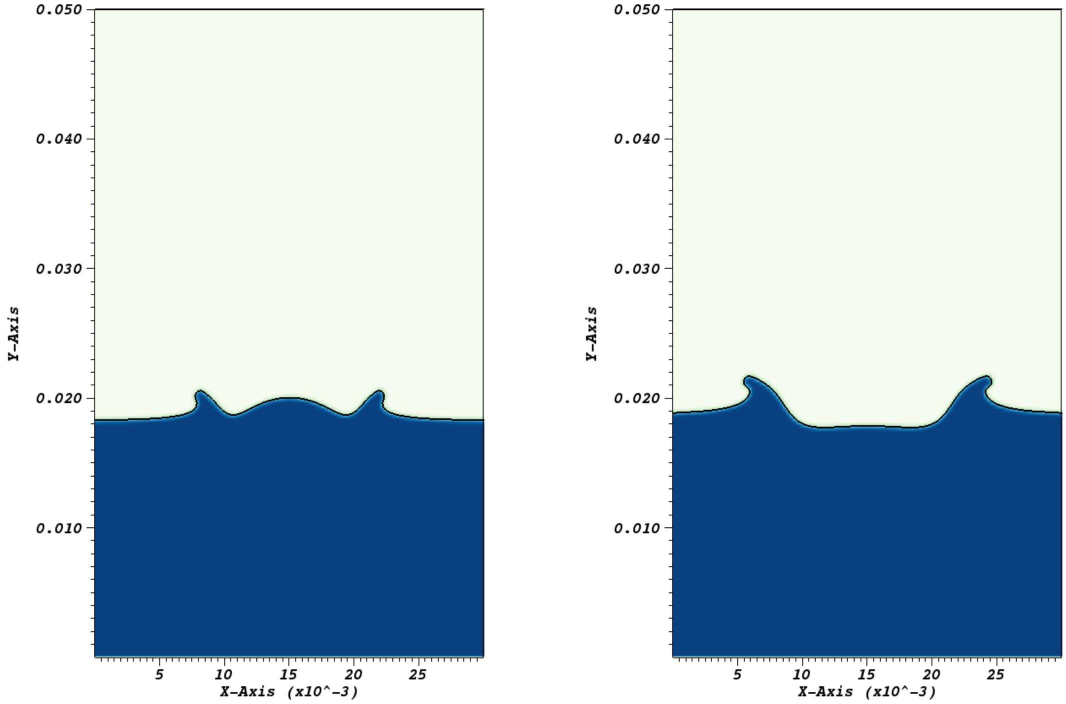

(c) time = 0.04 sec

(d) time = 0.05 sec

Figure 7.6: 2D water droplet splashing on water, Grid size = 120 × 200 CVs

(a) time = 0.0 sec

(b) time = 0.025 sec

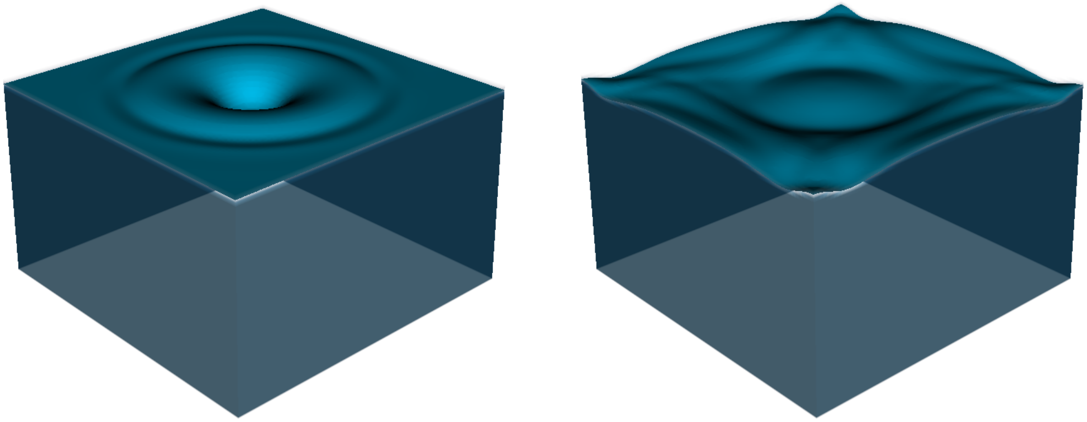

(c) time = 0.05 sec

(d) time = 0.075 sec

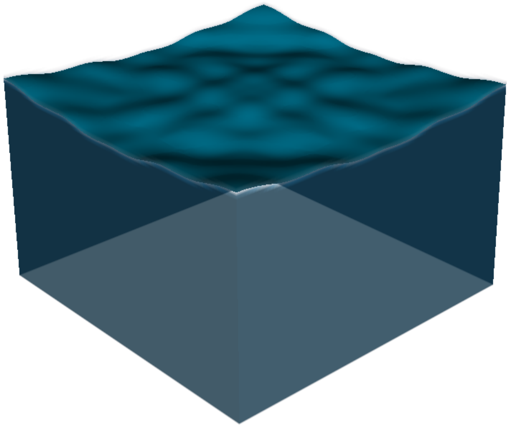

(e) time = 0.10 sec

Figure 7.7: 3D water droplet splashing on water, Grid size = 90 × 90 × 120 CVs

7.4.4 Liquid Meniscus in a Vertical Capillary Channel

The meniscus of a liquid column in a vertical capillary channel takes a definite form due to opposing effects of the surface tension and the gravitational forces. In this simulation, initially a water column is kept in a static state with the water surface in a horizontal position as shown in Figure 7.8a. The test specifications are the same as mentioned in Garrioch and Baliga [122]. The width of the channel is 1.25 mm and the height of the channel is 3.75 mm. No-slip and impermeability boundary conditions are applied at the wall boundaries. Contact angle boundary conditions were applied at the side walls, which can be represented as follows:

$$\mathbf{n}.\mathbf{n}_{wall} = \cos\theta_c \tag{7.33}$$

where $\mathbf{n}$ is the outward normal to the interface, $\mathbf{n}_{wall}$ is the outward normal to the solid wall, and θ_c is the contact angle. In this case, the contact angle (θ_c) between the water and the solid wall was assumed to be 10 degrees. The simulation starts with a quiescent water meniscus. As the time progresses, the meniscus shape deforms due to the surface tension effects and eventually attains a near half-circular shape at t = 0.05 sec.

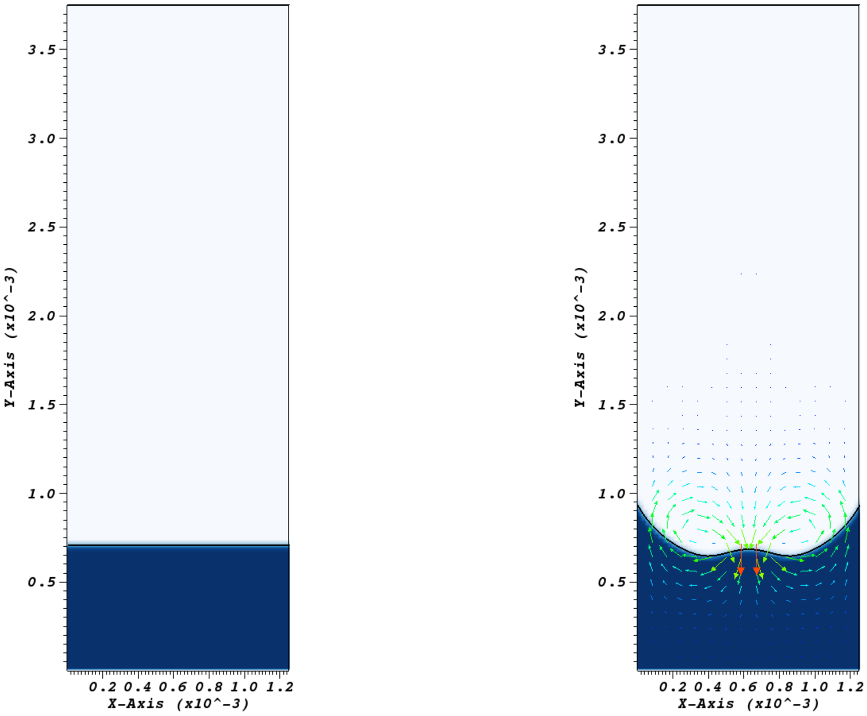

(a) t = 0.000 sec (b) t = 0.0.005 sec

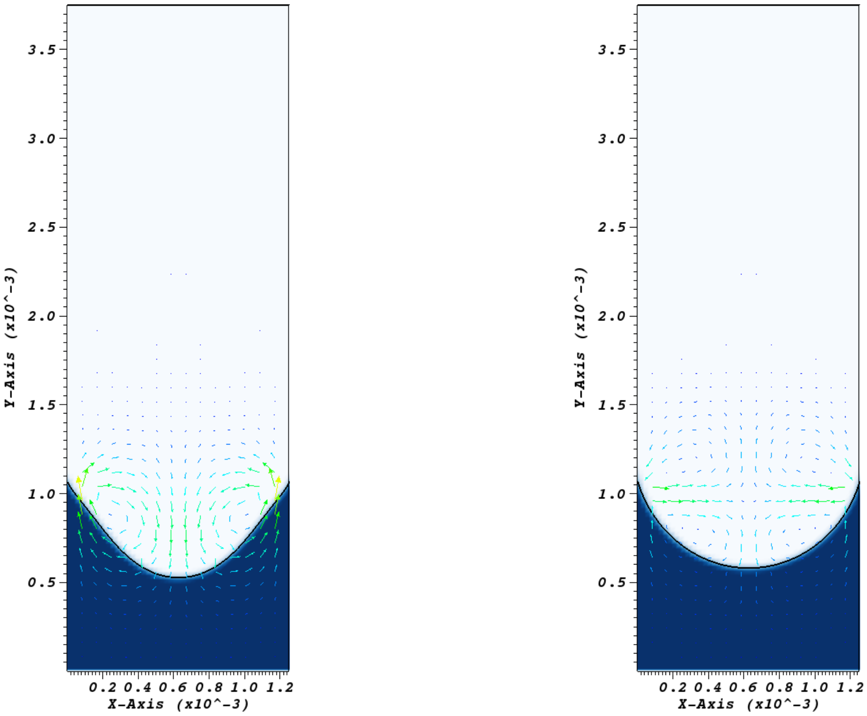

(c) t = 0.010 sec (d) t = 0.050 sec

Figure 7.8: Meniscus shape changing in a vertical capillary channel, Channel width = 1.25 mm, Channel height = 3.75 mm

7.4.5 Rayleigh-Taylor Instability

When a heavy fluid is placed over a light fluid, the light fluid penetrates the heavy fluid and an instability occurs at the interface due to the density differences. This phenomena is commonly known as Rayleigh-Taylor instability [123]. In this subsection, the evolution of Rayleigh-Taylor instability will be presented using the level set method. Similar tests were performed by a number of researchers. Among them, Bell and Marcus [124], and Puckett et al. [125] used the VOF method, Popinet and Zaleski [126] used the front tracking method, and Gomez et al. [127] used the level set method to simulate the Rayleigh-Taylor instability. In this test case, the density of the heavy fluid is 1.225 kgm^{-3}, and the density of the light fluid is 0.1694 kgm^{-3}. The dynamic viscosity is the same for both fluids (3.13×10^{-3} Pa-s). The surface tension was assumed to be $\sigma = 0.1337$ Nm^{-1}. The computational domain is 1 m wide and 4 m high. Initially a small perturbation is introduced at the interface in a cosine function form with an amplitude of 5 cm: $y(x) = -0.05cos(\pi x/\zeta)$, where ζ is the width of the computational domain. Free slip boundary conditions were imposed at all the sides. A grid size of 64 × 256 CVs was used for this simulation. Figure 7.9 presents the evolution of the interface at different instants. The thin filaments of the interface characterizing the Rayleigh-Taylor instability can be captured with the present level set method.

7.4.6 Spreading of Droplet on Hydrophilic and Hydrophobic Surfaces

The spreading of a liquid droplet on a solid surface forms an interesting test case, since the nature of the spreading will depend on the contact angle between the droplet and the solid surface. For a hydrophilic surface, where the contact angle is less than 90 degrees, the droplet will spread uniformly on the solid surface forming a void space in the middle. Such a test case of a water droplet spreading on a hydrophilic

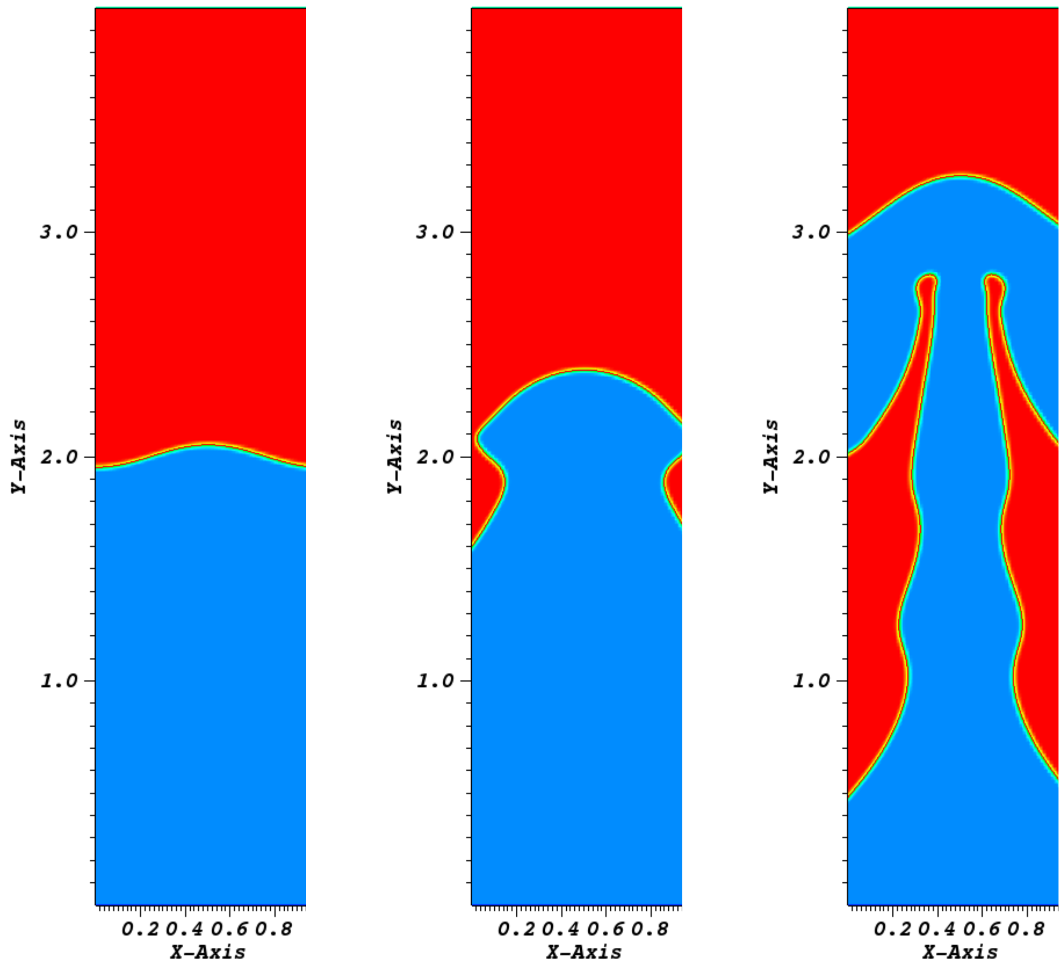

(a) t = 0.00 sec (b) t = 0.50 sec (c) t = 1.00 sec

Figure 7.9: Rayleigh Taylor instability, Grid size = 100 × 400 CVs

surface is shown in Figure 7.10. The contact angle between the water droplet and the solid surface was assumed to be 60 degrees. On the other hand, for a hydrophobic surface, where the contact angle is higher than 90 degrees, the droplet will try to retain its shape and for superhydrophobic surface it will produce a lotus leaf effect. A water droplet spreading and retaining its shape on a superhydrophobic surface is shown in Figure 7.11. The contact angle used in this case was 160 degrees. Thus, the level set method can also be applied efficiently to investigate the microchannel flow phenomena where contact angle plays an important role.

7.5 Conclusions

A level set method introduced by Osher and Sethian [38] was described to capture the interface in two phase flow simulations. In order to validate the level set method, a number of test cases were presented, both with and without prescribed velocities. These test cases are - circular interface in a time reversed single vortex field, collapse of a water column, droplet splashing on a water pool, liquid meniscus in a capillary microchannel, Rayleigh-Taylor instability and spreading of liquid droplet in hydrophilic and hydrophobic surfaces. The application of the free slip boundary condition and contact angle boundary condition for different cases were also presented. From these test cases, the applicability of the level set method for complex two phase flow phenomena with surface tension and large body forces has been demonstrated. The effectiveness of the level set method in simulating two-dimensional and three-dimensional test cases implies that it can be easily extended to investigate the two phase flow features in microchannels subjected to rotational forces.

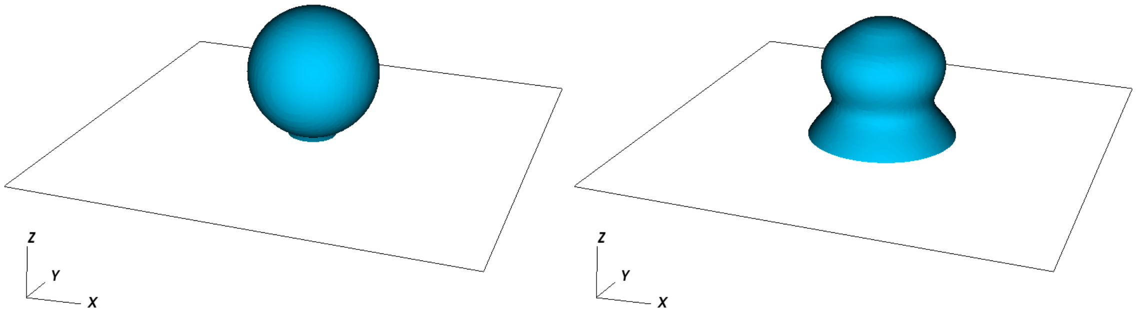

(a) t = 0.00 sec (b) t = 0.02 sec

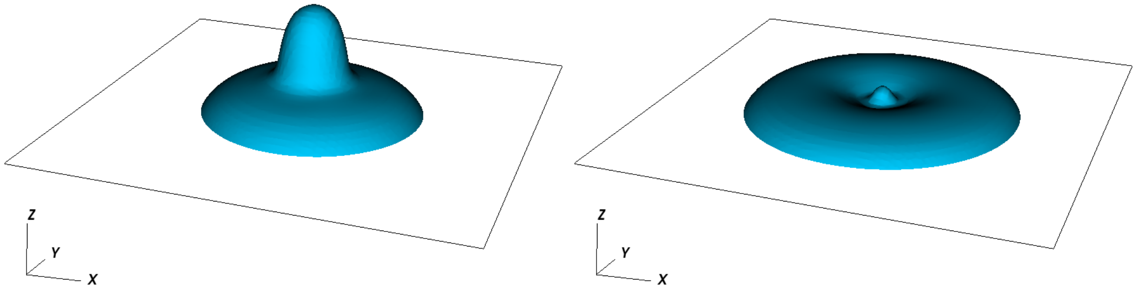

(c) t = 0.04 sec (d) t = 0.06 sec

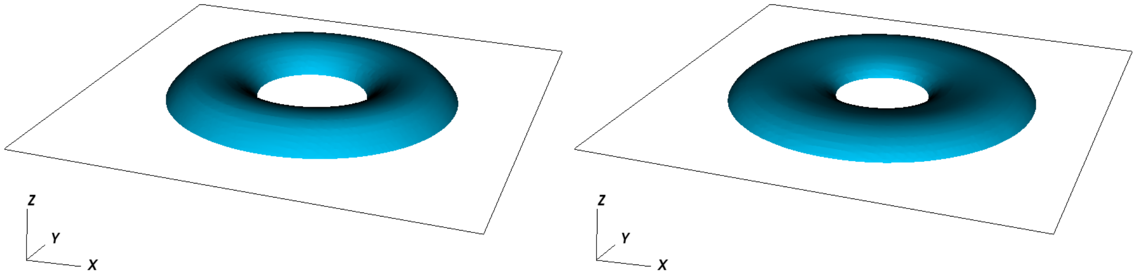

(e) t = 0.08 sec (f) t = 0.10 sec

Figure 7.10: Spreading of water droplet on hydrophilic surface, Domain size = 2 cm × 2 cm × 1 cm, Droplet diameter = 6 mm, Grid size = 96 × 96 × 48 CVs

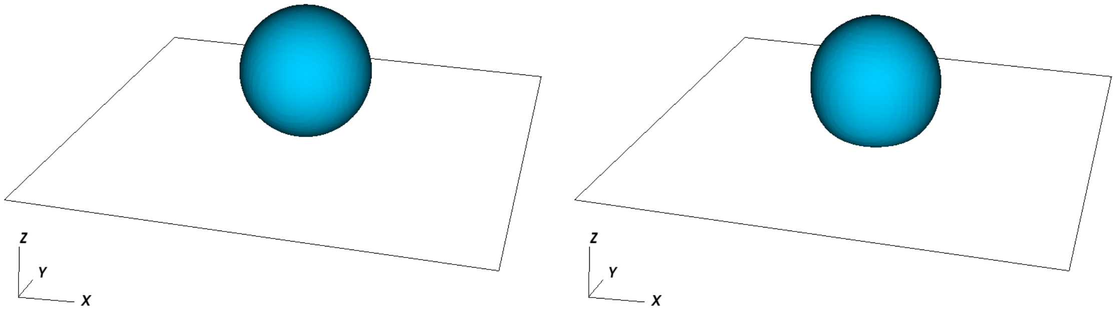

(a) t = 0.00 sec (b) t = 0.02 sec

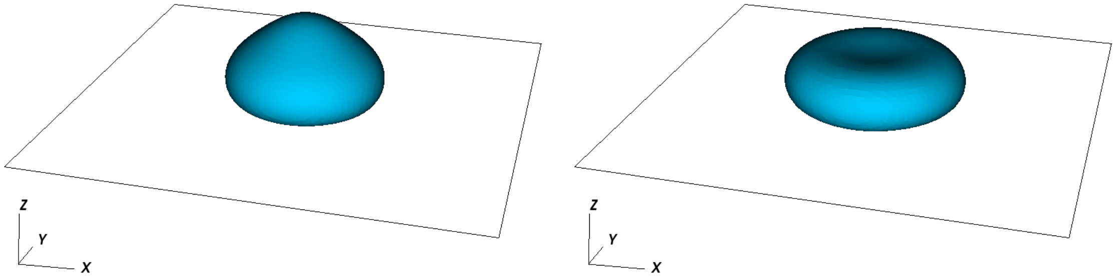

(c) t = 0.04 sec (d) t = 0.06 sec

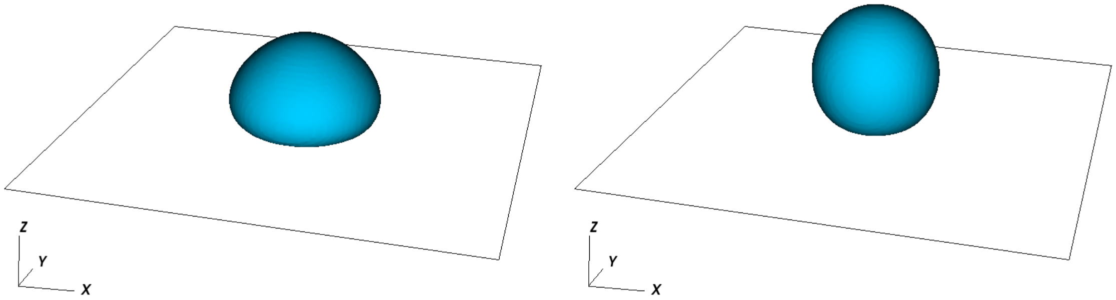

(e) t = 0.08 sec (f) t = 0.10 sec

Figure 7.11: Spreading of water droplet on hydrophobic surface, Domain size = 2 cm × 2 cm × 1 cm, Droplet diameter = 6 mm, Grid size = 96 × 96 × 48 CVs

8. SUMMARY

Pressure-based finite volume solvers using both staggered and collocated grid approaches were developed to solve two-dimensional and three-dimensional, steady and unsteady, incompressible Navier-Stokes equations. The programming language used for this purpose was FORTRAN 90. The collocated grid solver was parallelized using a Message Passing Interface (MPI) library and good parallel scalability was demonstrated up to 64 processors for a two-dimensional lid driven cavity flow with a grid size of 512 × 512 CVs. In order to accelerate the convergence rate of the finite volume solver, a non-linear multigrid technique was developed. Parallel implementation of the proposed multigrid algorithm was presented and the effects of parallelization on multigrid properties were analyzed. Superior convergence rate for parallel multigrid solver as compared to parallel single grid solver was demonstrated and multigrid speedup as high as 1370 times was attained for a 2D lid driven cavity flow using a grid size of 1024 × 1024.

Next, the effects of rotational speed and aspect ratio on a steady, three-dimensional, rotating microchannel flow were analyzed. By studying the RMS deviation of the velocity profiles of rotating flows from that of a purely centrifugal flow, a critical rotational Reynolds number was defined, above which the secondary flow effects become dominant. In addition, a critical aspect ratio was identified for which the optimal secondary flow effect was observed. The sub-critical and super-critical operating modes of rotating microchannel flows were discussed.

In the next step, the effect of liquid slip on the rotating microchannel flow was investigated. An analytical solution for a purely centrifugal flow with slip boundary condition was presented and its accuracy was validated for a non-rotating microchannel flow case by comparing it with the available experimental results. New correlations for friction factors or Poiseuille number (fRe) were derived incorporating the effects of rotation and liquid slip for different aspect ratios. The affects of liquid slip and rotation on the heat transfer characteristics of the fluid were also presented.

A level set method coupled with the finite volume solver was described to capture the interface during two-phase flow simulations. The implementation of boundary conditions for velocity and level set function was narrated. A number of test cases were performed to demonstrate its effectiveness and limitations of the level set method.

REFERENCES

[1] R. D. Johnson, I. H. A. Badr, G. Barrett, S. Lai, Y. Lu, M. J. Madou, and L. G. Bachas. Development of a fully integrated analysis system for ions based on ion-selective optodes and centrifugal microfluidics. *Analytical Chemistry*, 73(16):3940–3946, 2001.

[2] T. Brenner, T. Glatzel, R. Zengerle, and J. Ducrée. Frequency dependent transversal flow control in centrifugal microfluidics. *Lab Chip*, 5(2):146–150, 2005.

[3] M. Madou, J. Zoval, G. Jia, H. Kido, J. Kim, and N. Kim. Lab on a cd. *Annu. Rev. Biomed. Eng.*, 8:601–628, 2006.

[4] J. Ducrée, S. Haeberle, S. Lutz, S. Pausch, F. von Stetten, and R. Zengerle. The centrifugal microfluidic Bio-Disk platform. *Journal of Micromechanics and Microengineering*, 17:S103–S115, 2007.

[5] R. Zengerle, P. Koltay, and J. Ducrée. Microfluidics: an enabling technology for the life sciences. In *Micro-Nanomechatronics and Human Science, 2004 and The Fourth Symposium Micro-Nanomechatronics for Information-Based Society, 2004. Proceedings of the 2004 International Symposium on micro-nano mechatronics and human science*, pages 1–6. IEEE, 2004.

[6] J. Siegrist, M. Amasia, N. Singh, D. Banerjee, and M. Madou. Numerical modeling and experimental validation of uniform microchamber filling in centrifugal microfluidics. *Lab Chip*, 10(7):876–886, 2010.

[7] D. Mark, S. Haeberle, G. Roth, F. Stetten, and R. Zengerle. Microfluidic lab-on-a-chip platforms: requirements, characteristics and applications. *Mi-*

crofluidics Based Microsystems, pages 305–376, 2010.

[8] J. Zeng, D. Banerjee, M. Deshpande, J. R. Gilbert, D. C. Duffy, and G. J. Kellogg. Design analyses of capillary burst valves in centrifugal microfluidics. In *Proceedings of the Micro Total Analysis Systems Symposium (μTAS 2000)*, pages 14–18, 2000.

[9] D. Chakraborty, M. Madou, and S. Chakraborty. Anomalous mixing behaviour in rotationally actuated microfluidic devices. *Lab Chip*, 11(17):2823–2826, 2011.

[10] D. C. Duffy, H. L. Gillis, J. Lin, N. F. Sheppard Jr, and G. J. Kellogg. Microfabricated centrifugal microfluidic systems: characterization and multiple enzymatic assays. *Analytical Chemistry*, 71(20):4669–4678, 1999.

[11] J. Ducrée, S. Haeberle, T. Brenner, T. Glatzel, and R. Zengerle. Patterning of flow and mixing in rotating radial microchannels. *Microfluidics and Nanofluidics*, 2(2):97–105, 2006.

[12] J. Ducrée, T. Brenner, S. Haeberle, T. Glatzel, and R. Zengerle. Multilamination of flows in planar networks of rotating microchannels. *Microfluidics and Nanofluidics*, 2(1):78–84, 2006.

[13] P. Roy, N. K. Anand, and D. Banerjee. A review of flow and heat transfer in rotating microchannels. *Procedia Engineering*, 56:7–17, 2013.

[14] U. Lei and C. H. Hsu. Flow through rotating straight pipes. *Physics of Fluids A: Fluid Dynamics*, 2:63, 1990.

[15] E. Lauga, M. P. Brenner, and H. A. Stone. Microfluidics: The no-slip boundary condition. *Handbook of Experimental Fluid Dynamics (Chapter 19)*, 2007.

[16] L. Bocquet and J. L. Barrat. Flow boundary conditions from nano-to micro-scales. *Soft Matter*, 3(6):685–693, 2007.

[17] B. J. Kirby. *Micro-and Nanoscale Fluid Mechanics: Transport in Microfluidic Devices*. Cambridge University Press, New York, 2010.

[18] M. Gad-el Hak. The fluid mechanics of microdevices – The Freeman scholar lecture. *Transactions – ASME Journal of Fluids Engineering*, 121:5–33, 1999.

[19] M. Gad-el Hak. *The MEMS Handbook*. CRC Mechanical Engineering Series, New York, 2002.

[20] A. Bontemps. Measurements of single-phase pressure drop and heat transfer coefficient in micro and minichannels. *Microscale Heat Transfer Fundamentals and Applications*, pages 25–48, 2005.

[21] G. Karniadakis, A. Beşkök, and N. R. Aluru. *Microflows and Nanoflows: Fundamentals and Simulation*, volume 29. Springer-Verlag, New York, 2005.

[22] S. V. Garimella and C. B. Sobhan. Transport in microchannels – a critical review. *Annual Review of Heat Transfer*, 13:1–50, 2003.

[23] M. E. Steinke and S. G. Kandlikar. Single-phase liquid friction factors in microchannels. *International Journal of Thermal Sciences*, 45(11):1073–1083, 2006.

[24] J. Drelich, E. Chibowski, D. D. Meng, and K. Terpilowski. Hydrophilic and superhydrophilic surfaces and materials. *Soft Matter*, 7(21):9804–9828, 2011.

[25] C. Cottin-Bizonne, S. Jurine, J. Baudry, J. Crassous, F. Restagno, and E. Charlaix. Nanorheology: an investigation of the boundary condition at hydrophobic and hydrophilic interfaces. *The European Physical Journal E: Soft Matter and Biological Physics*, 9(1):47–53, 2002.

[26] E. Bonaccurso, M. Kappl, and H. J. Butt. Hydrodynamic force measurements: boundary slip of water on hydrophilic surfaces and electrokinetic effects. *Physical Review Letters*, 88(7):76103, 2002.

[27] D. C. Tretheway and C. D. Meinhart. Apparent fluid slip at hydrophobic microchannel walls. *Physics of Fluids*, 14:L9, 2002.

[28] R. Pit, H. Hervet, and L. Leger. Direct experimental evidence of slip in hexadecane: solid interfaces. *Physical Review Letters*, 85(5):980–983, 2000.

[29] K. Watanabe, Yanuar, and H. Mizunuma. Slip of newtonian fluids at slid boundary. *JSME International Journal. Series B, Fluids and Thermal Engineering*, 41(3):525–529, 1998.

[30] C. Neto, D. R. Evans, E. Bonaccurso, H. J. Butt, and V. S. J. Craig. Boundary slip in newtonian liquids: a review of experimental studies. *Reports on Progress in Physics*, 68:2859, 2005.

[31] J. P. Rothstein. Slip on superhydrophobic surfaces. *Annual Review of Fluid Mechanics*, 42:89–109, 2010.

[32] Y. P. Cheng, C. J. Teo, and B. C. Khoo. Microchannel flows with superhydrophobic surfaces: Effects of Reynolds number and pattern width to channel height ratio. *Physics of Fluids*, 21:122004, 2009.

[33] K. Watanabe, Y. Udagawa, and H. Udagawa. Drag reduction of newtonian fluid in a circular pipe with a highly water-repellent wall. *Journal of Fluid Mechanics*, 381(1):225–238, 1999.

[34] K. Watanabe, T. Takayama, S. Ogata, and S. Isozaki. Flow between two coaxial rotating cylinders with a highly water-repellent wall. *AIChE journal*, 49(8):1956–1963, 2003.

[35] C. H. Choi and C. J. Kim. Large slip of aqueous liquid flow over a nano-engineered superhydrophobic surface. *Physical Review Letters*, 96(6):066001, 2006.

[36] P. Roy, N. K. Anand, and D. Banerjee. Numerical investigation of slip flow and heat transfer in rotating rectangular microchannels. In *ASME 2012 Heat Transfer Summer Conference*, pages 1087–1094. American Society of Mechanical Engineers, 2012.

[37] S. V. Patankar. *Numerical Heat Transfer and Fluid Flow.* Hemisphere Publishing Corp., Washington DC, 1980.

[38] S. Osher and J. A. Sethian. Fronts propagating with curvature-dependent speed: algorithms based on Hamilton-Jacobi formulations. *Journal of Computational Physics*, 79(1):12–49, 1988.

[39] F. H. Harlow and J. E. Welch. Numerical calculation of time-dependent viscous incompressible flow of fluid with free surface. *Physics of Fluids*, 8(12):2182, 1965.

[40] S. V. Patankar and D. B. Spalding. A calculation procedure for heat, mass and momentum transfer in three-dimensional parabolic flows. *International Journal of Heat and Mass Transfer*, 15(10):1787–1806, 1972.

[41] C. M. Rhie and W. L. Chow. Numerical study of the turbulent flow past an airfoil with trailing edge separation. *AIAA journal*, 21(11):1525–1532, 1983.

[42] J. H. Ferziger and M. Perić. *Computational Methods for Fluid Dynamics*, volume 3. Springer, Berlin, 2002.

[43] M. Ijaz and N. K. Anand. Co-located variables approach using implicit runge-kutta methods for unsteady incompressible flow simulation. *Numerical Heat*

Transfer, Part B: Fundamentals, 54(4):291–313, 2008.

[44] N. Kim, N. K. Anand, and D. L. Rhode. A study on convergence criteria for a simple-based finite-volume algorithm. *Numerical Heat Transfer, Part B: Fundamentals*, 34(4):401–417, 1998.

[45] J. G. B. Saldaña, V. Sarin, and N. K. Anand. Parallelization of a simple-based algorithm to simulate mixed convective flow over a backward-facing step. *Numerical Heat Transfer, Part B: Fundamentals*, 56(2):105–118, 2009.

[46] D. A. Donzis, P. K. Yeung, and D. Pekurovsky. Turbulence simulations on O(10^4) processors. *Proc. TeraGrid*, 2008.

[47] Shriram Jagannathan and Diego A Donzis. Massively parallel direct numerical simulations of forced compressible turbulence: a hybrid MPI/OpenMP approach. In *Proceedings of the 1st Conference of the Extreme Science and Engineering Discovery Environment: Bridging from the eXtreme to the campus and beyond*, page 23. ACM, 2012.

[48] G. Hager and G. Wellein. *Introduction to high performance computing for scientists and engineers*. CRC Press, Florida, 2010.

[49] P. S. Pacheco. *Parallel programming with MPI*. Morgan Kaufmann, Massachusetts, 1997.

[50] P. Balaji, W. Bland, W. Gropp, R. Latham, H. Lu, A. J. Pena, K. Raffenetti, R. Thakur, and J. Zhang. MPICH User's Guide. 2014.

[51] M. Ijaz. *Implicit Runge-Kutta methods to simulate unsteady incompressible flows*. PhD thesis, Texas A&M University, 2007.

[52] A. Brandt. Multi-level adaptive solutions to boundary-value problems. *Mathematics of Computation*, 31(138):333–390, 1977.

[53] M. Hortmann, M. Perić, and G. Scheuerer. Finite volume multigrid prediction of laminar natural convection: Bench-mark solutions. *International Journal for Numerical Methods in Fluids*, 11(2):189–207, 1990.

[54] F. S. Lien and M. A. Leschziner. Multigrid acceleration for recirculating laminar and turbulent flows computed with a non-orthogonal, collocated finite-volume scheme. *Computer Methods in Applied Mechanics and Engineering*, 118(3):351–371, 1994.

[55] D. S. Kumar, K. S. Kumar, and M. K. Das. A fine grid solution for a lid-driven cavity flow using multigrid method. *Engineering Applications of Computational Fluid Mechanics*, 3(3):336–354, 2009.

[56] W. Shyy and C. S. Sun. Development of a pressure-correction/staggered-grid based multigrid solver for incompressible recirculating flows. *Computers & Fluids*, 22(1):51–76, 1993.

[57] S. Thakur, J. Wright, W. Shyy, J. Liu, H. Ouyang, and T. Vu. Development of pressure-based composite multigrid methods for complex fluid flows. *Progress in Aerospace Sciences*, 32(4):313–375, 1996.

[58] K. M. Smith, W. K. Cope, and S. P. Vanka. A multigrid procedure for three-dimensional flows on non-orthogonal collocated grids. *International Journal for Numerical Methods in Fluids*, 17(10):887–904, 1993.

[59] J. Yan and F. Thiele. Performance and accuracy of a modified full multigrid algorithm for fluid flow and heat transfer. *Numerical Heat Transfer, Part B: Fundamentals*, 34(3):323–338, 1998.

[60] S. P. Vanka. Block-implicit multigrid solution of Navier-Stokes equations in primitive variables. *Journal of Computational Physics*, 65(1):138–158, 1986.

[61] S. P. Vanka. A calculation procedure for three-dimensional steady recirculating flows using multigrid methods. *Computer Methods in Applied Mechanics and Engineering*, 55(3):321–338, 1986.

[62] D. S. Joshi and S. P. Vanka. Multigrid calculation procedure for internal flows in complex geometries. *Numerical Heat Transfer, Part B: Fundamentals*, 20(1):61–80, 1991.

[63] P. S. Sathyamurthy and S. V. Patankar. Block-correction-based multigrid method for fluid flow problems. *Numerical Heat Transfer, Part B: Fundamentals*, 25(4):375–394, 1994.

[64] J. E Jones and S. F. McCormick. Parallel multigrid methods. In *Parallel Numerical Algorithms*, pages 203–224. Springer, Berlin, 1997.

[65] F. Durst and M. Schäfer. A parallel block-structured multigrid method for the prediction of incompressible flows. *International Journal for Numerical Methods in Fluids*, 22(6):549–565, 1996.

[66] P. Wang and R. D. Ferraro. Parallel multigrid finite volume computation of three-dimensional thermal convection. *Computers & Mathematics with Applications*, 37(9):49–60, 1999.

[67] E. Chow, R. D. Falgout, J. J. Hu, R. S. Tuminaro, and U. M. Yang. A survey of parallelization techniques for multigrid solvers. *Parallel Processing for Scientific Computing*, 20:179–201, 2006.

[68] P. Roy, N. K. Anand, and D. Donzis. A parallel multigrid finite volume solver in collocated grid for incompressible Navier-Stokes equations. *Numerical Heat Transfer, Part B: Fundamentals*, in press.

[69] W. Hackbusch. *Multi-grid Methods and Applications.* Springer-Verlag, Berlin, 1985.

[70] W. L. Briggs, V. E. Henson, and S. F. McCormick. *A Multigrid Tutorial.* SIAM, Philadelphia, 2000.

[71] P. Wesseling. *An Introduction to Multigrid Methods.* John Wiley & Sons, Chichester, 1992.

[72] U. Trottenberg, C. W. Oosterlee, and A. Schuller. *Multigrid.* Academic Press, London, 2000.

[73] A. Brandt and O. E. Livne. *Multigrid Techniques: 1984 Guide with Applications to Fluid Dynamics.* SIAM, 2011.

[74] P. N. Shankar and M. D. Deshpande. Fluid mechanics in the driven cavity. *Annual Review of Fluid Mechanics*, 32(1):93–136, 2000.

[75] U. K. N. G. Ghia, K. N. Ghia, and C. T. Shin. High-Re solutions for incompressible flow using the Navier-Stokes equations and a multigrid method. *Journal of Computational Physics*, 48(3):387–411, 1982.

[76] E. Erturk, T. C. Corke, and C. Gökçöl. Numerical solutions of 2-d steady incompressible driven cavity flow at high Reynolds numbers. *International Journal for Numerical Methods in Fluids*, 48(7):747–774, 2005.

[77] S. Muzaferija. *Adaptive finite volume method for flow prediction using unstructured meshes and multigrid approach.* PhD thesis, University of London UK, 1994.

[78] J. D. Mlcak, N. K. Anand, and M. J. Rightley. Three-dimensional laminar flow and heat transfer in a parallel array of microchannels etched on a substrate. *International Journal of Heat and Mass Transfer*, 51(21-22):5182–5191, 2008.

[79] W. D. Morris. *Heat Transfer and Fluid Flow in Rotating Coolant Channels.* Research Studies Press, Baldock, 1981.

[80] M. Liu, J. Zhang, Y. Liu, W. M. Lau, and J. Yang. Modeling of flow burst, flow timing in lab-on-a-cd systems and its application in digital chemical analysis. *Chemical Engineering & Technology*, 31(9):1328–1335, 2008.

[81] D. Chakraborty, R. Gorkin, M. Madou, L. Kulinsky, and S. Chakraborty. Capillary filling in centrifugally actuated microfluidic devices with dynamically evolving contact line motion. *Journal of Applied Physics*, 105(8):084904, 2009.

[82] S. V. Patankar, C. H. Liu, and E. M. Sparrow. Fully developed flow and heat transfer in ducts having streamwise-periodic variations of cross-sectional area. *Journal of Heat Transfer*, 99:180, 1977.

[83] R. K. Shah and A. L. London. Thermal boundary conditions and some solutions for laminar duct flow forced convection. *Journal of Heat Transfer*, 96(2):159–165, 1974.

[84] K. Kawano, M. Sekimura, M. Ko, H. Iwasaki, and M. Ishizuka. Development of micro channel heat exchanging. *JSME International Journal. Series B, Fluids and Thermal Engineering*, 44(4):592–598, 2001.

[85] S. S. Hsieh, Y. J. Hong, and S. R. Jeng. Three-dimensional laminar forced convection in a rotating square duct with a rib on the leading wall. *International Journal of Heat and Mass Transfer*, 37(15):2273–2285, 1994.

[86] P. Roy, N. K. Anand, and D. Banerjee. Numerical simulation of flow and heat transfer in radially rotating microchannels. *Microfluidics and Nanofluidics*, 15(3):397–413, 2013.

[87] G. J. Hwang and T. C. Jen. Convective heat transfer in rotating isothermal ducts. *International Journal of Heat and Mass Transfer*, 33(9):1817–1828, 1990.

[88] J. Tien-Chien, A. S. Lavine, and H. Guang-Jyh. Simultaneously developing laminar convection in rotating isothermal square channels. *International Journal of Heat and Mass Transfer*, 35(1):239–254, 1992.

[89] J. Zhang, Y. Liu, J. Zhang, and J. Yang. Study of force-dependent and time-dependent transition of secondary flow in a rotating straight channel by the lattice boltzmann method. *Physica A: Statistical Mechanics and its Applications*, 388(4):288–294, 2009.

[90] W. W. F. Leung and Y. Ren. Scale-up on mixing in rotating microchannel under subcritical and supercritical operating modes. *International Journal of Heat and Mass Transfer*, 77:157–172, 2014.

[91] P. Roy, N. K. Anand, and D. Banerjee. Liquid slip and heat transfer in rotating rectangular microchannels. *International Journal of Heat and Mass Transfer*, 62:184–199, 2013.

[92] C. Navier. Mémoire sur les lois du mouvement des fluides. *Mémoires de l'Académie Royale des Sciences de l'Institut de France*, 6:389–440, 1823.

[93] W. G. Vincenti and C. H. Kruger. *Introduction to Physical Gas Dynamics*. Wiley, New York, 1965.

[94] J. L. Barrat and F. Chiaruttini. Kapitza resistance at the liquid–solid interface. *Molecular Physics*, 101(11):1605–1610, 2003.

[95] P. L. Kapitza. Heat transfer and superfluidity of helium II. *Physical Review*, 60(4):354, 1941.

[96] W. A. Ebert and E. M. Sparrow. Slip flow in rectangular and annular ducts. *Journal of Basic Engineering*, 87:1018, 1965.

[97] H. D. Hettiarachchi, M. Golubovic, W. M. Worek, and W. J. Minkowycz. Three-dimensional laminar slip-flow and heat transfer in a rectangular microchannel with constant wall temperature. *International Journal of Heat and Mass Transfer*, 51(21):5088–5096, 2008.

[98] R. K. Shah and A. L. London. *Laminar Flow Forced Convection in Ducts: A Source Book for Compact Heat Exchanger Analytical Data*. Academic Press, New York, 1978.

[99] L. Zhu, D. Tretheway, L. Petzold, and C. Meinhart. Simulation of fluid slip at 3D hydrophobic microchannel walls by the lattice Boltzmann method. *Journal of Computational Physics*, 202(1):181–195, 2005.

[100] M. Renksizbulut, H. Niazmand, and G. Tercan. Slip-flow and heat transfer in rectangular microchannels with constant wall temperature. *International Journal of Thermal Sciences*, 45(9):870–881, 2006.

[101] H. Itō and K. Nanbu. Flow in rotating straight pipes of circular cross section. *Journal of Basic Engineering*, 93:383, 1971.

[102] D. Gerlach, G. Tomar, G. Biswas, and F. Durst. Comparison of volume-of-fluid methods for surface tension-dominant two-phase flows. *International Journal of Heat and Mass Transfer*, 49(3):740–754, 2006.

[103] W. Shyy, H. S. Udaykumar, M. M. Rao, and R. W. Smith. *Computational Fluid Dynamics with Moving Boundaries*. Courier Dover Publications, New York, 2012.

[104] A. Salih and S. G. Moulic. Some numerical studies of interface advection properties of level set method. *Sadhana*, 34(2):271–298, 2009.

[105] K. Yu. *Level-set RANS method for sloshing and green water simulations.* PhD thesis, Texas A&M University, 2007.

[106] M. Sussman, P. Smereka, and S. Osher. A level set approach for computing solutions to incompressible two-phase flow. *Journal of Computational Physics*, 114(1):146–159, 1994.

[107] J. U. Brackbill, D. B. Kothe, and C. Zemach. A continuum method for modeling surface tension. *Journal of Computational Physics*, 100(2):335–354, 1992.

[108] A. Harten, B. Engquist, S. Osher, and S. R. Chakravarthy. Uniformly high order accurate essentially non-oscillatory schemes, iii. *Journal of Computational Physics*, 71(2):231–303, 1987.

[109] R. Fedkiw and S. Osher. *Level Set Methods and Dynamic Implicit Surfaces.* Springer-Verlag, New York, 2003.

[110] X. D. Liu, S. Osher, and T. Chan. Weighted essentially non-oscillatory schemes. *Journal of Computational Physics*, 115(1):200–212, 1994.

[111] R. J. LeVeque. *Numerical Methods for Conservation Laws*, volume 132. Springer, Berlin, 1992.

[112] M. Sussman and E. Fatemi. An efficient, interface-preserving level set redistancing algorithm and its application to interfacial incompressible fluid flow. *SIAM Journal on Scientific Computing*, 20(4):1165–1191, 1999.

[113] J. B. Bell, P. Colella, and H. M. Glaz. A second-order projection method for the incompressible Navier-Stokes equations. *Journal of Computational Physics*, 85(2):257–283, 1989.

[114] R. J. Leveque. High-resolution conservative algorithms for advection in incompressible flow. *SIAM Journal on Numerical Analysis*, 33(2):627–665, 1996.

[115] W. Ren and E. Weinan. Boundary conditions for the moving contact line problem. *Physics of Fluids*, 19(2):022101, 2007.

[116] L. Bu and J. Zhao. Numerical simulation of the water bubble rising in a liquid column using the combination of level set and moving mesh methods in the collocated grids. *International Journal of Thermal Sciences*, 59:1–8, 2012.

[117] J. C. Martin and W. J. Moyce. Part iv. an experimental study of the collapse of liquid columns on a rigid horizontal plane. *Philosophical Transactions of the Royal Society of London. Series A, Mathematical and Physical Sciences*, 244(882):312–324, 1952.

[118] M. Raessi and H. Pitsch. Modeling interfacial flows characterized by large density ratios with the level set method. *Annual Research Brief*, 2009.

[119] X. Y. Li, Y. Wang, G. Z. Yu, C. Yang, and Z. S. Mao. A volume-amending method to improve mass conservation of level set approach for incompressible two-phase flows. *Science in China Series B: Chemistry*, 51(11):1132–1140, 2008.

[120] M. M. Francois, S. J. Cummins, E. D. Dendy, D. B. Kothe, J. M. Sicilian, and M. W. Williams. A balanced-force algorithm for continuous and sharp interfacial surface tension models within a volume tracking framework. *Journal of Computational Physics*, 213(1):141–173, 2006.

[121] M. Herrmann. A balanced force refined level set grid method for two-phase flows on unstructured flow solver grids. *Journal of Computational Physics*, 227(4):2674–2706, 2008.

[122] S. H. Garrioch and B. R. Baliga. A PLIC volume tracking method for the simulation of two-fluid flows. *International Journal for Numerical Methods in Fluids*, 52(10):1093–1134, 2006.

[123] G. Taylor. The instability of liquid surfaces when accelerated in a direction perpendicular to their planes. I. *Proceedings of the Royal Society of London. Series A. Mathematical and Physical Sciences*, 201(1065):192–196, 1950.

[124] J. B. Bell and D. L. Marcus. A second-order projection method for variable-density flows. *Journal of Computational Physics*, 101(2):334–348, 1992.

[125] E. G. Puckett, A. S. Almgren, J. B. Bell, D. L. Marcus, and W. J. Rider. A high-order projection method for tracking fluid interfaces in variable density incompressible flows. *Journal of Computational Physics*, 130(2):269–282, 1997.

[126] S. Popinet and S. Zaleski. A front-tracking algorithm for accurate representation of surface tension. *International Journal for Numerical Methods in Fluids*, 30(6):775–793, 1999.

[127] P. Gómez, J. Hernandez, and J. López. On the reinitialization procedure in a narrow-band locally refined level set method for interfacial flows. *International Journal for Numerical Methods in Engineering*, 63(10):1478–1512, 2005.

APPENDIX A

SMOOTHING PROPERTY OF ITERATIVE METHODS

Recalling Equation 4.1 for a system of linear equations:

$$A\phi = b \tag{A.1}$$

Here, ϕ is the *exact solution* of the problem, and A is the *coefficient matrix*. Let us assume that, A is a stationary matrix that means A is not changing with iterations. Thus, at any point of iteration, the *approximate solution* ϕ^* satisfies the following equation:

$$A\phi^* = b + R \tag{A.2}$$

where R is the *residual* term. Subtracting A.2 from A.1, we get the following *residual equation*:

$$Ae = -R \tag{A.3}$$

where e is the *algebraic error* defined by $e = \phi - \phi^*$.

Now, for the standard iterative techniques such as Gauss-Seidel or Jacobi methods, the iteration equation can be written in the following form (refer to Eq. 2.15):

$$\phi^{*(l+1)} = \phi^{*(l)} + BR^{(l)} \tag{A.4}$$

Here, B is an approximation to A^{-1}. Subtracting Equation A.4 from the exact solution ϕ, we get the following iteration equation for the error:

$$e^{(l+1)} = e^{(l)} - BR^{(l)} \tag{A.5}$$

We can observe from Equation A.5 that, at each iteration the error is corrected by the spatially local corrections through the residual. When the residual is small, the error correction is also small and vice versa. At the beginning of the iterations, the high frequency error components tend to produce large residuals which in turn correct the errors significantly with each iteration. After a few iterations the high frequency error components are eliminated and the remaining low frequency error components tend to produce small residuals resulting in a slow decrease of the error. This is commonly known as the *smoothing property* of iterative methods. For an in depth discussion on this *smoothing property* of the standard iterative techniques, the readers are referred to [70].